# Fakultät für Physik und Astronomie

**Ruprecht-Karls-Universität Heidelberg**


**Diplomarbeit**
**im Studiengang Physik**


**vorgelegt von**
**Florian Huhn**
**geboren in Neumünster**


**2008**

# A Simple Instrument for the Measurement of the Slope and Height Distributions of Small Scale Wind-Driven Water Waves

Diese Diplomarbeit wurde durchgeführt
von Florian Huhn
am Institut für Umweltphysik
unter der Betreuung von
**Herrn Prof. Dr. Bernd Jähne**

## Abstract

A new optical wave gauge was built to measure simultaneously two statistical parameters of wind induced water surface waves, namely the surface slope and surface amplitude probability distribution functions. The new instrument was tested in a linear wind wave flume with a water depth of 10 cm. The surface slope is determined using the refraction of light at the water surface. The wave amplitude is measured using the absorption of infrared light in the water column. The wave gauge consists of a point-like dichromatic light source which is positioned under the flume (Ulbricht sphere with high-power LEDs, $\lambda_{RED} = 632\,\mathrm{nm}$ and $\lambda_{IR} = 850\,\mathrm{nm}$) and a camera above the flume that looks vertically through the water into the light source. No other optical components are needed. The light source is pulsed and the camera is triggered. The images show light speckles whose positions are a measure for the wave slope. The relative intensities are a measure for the wave amplitude. These quantities are derived from the digital images by means of image processing and simple geometrical considerations. The influence of different analysis methods on the wave slope and amplitude distribution was studied.

For the characterization of the new linear wind wave flume in the Institut für Umweltphysik (IUP), Heidelberg, mean square slope and root mean square wave height were measured for a wind speed up to 6.7 m/s and a fetch between 0.80 m and 2.40 m. The findings agree with comparable measurements in other linear wind wave flumes.



## Zusammenfassung

Ein neues Wellenmessgerät zur gleichzeitigen Messung von zwei statistischen Parametern von winderzeugten Wasseroberflächenwellen wurde gebaut. Dies sind die Wahrscheinlichkeitsdichtefunktionen der Wellenneigung und der Wellenamplitude. Das Messgerät wurde an einem linearen Wind-Wellenkanal mit 10 cm Wassertiefe getestet. Die Messung der Oberflächenneigung basiert auf der Brechung von Licht an der Wasseroberfläche. Die Wellenamplitude wird über die Absorption von Infrarotlicht in der Wassersäule gemessen. Das Wellenmessgerät besteht aus einer punktförmigen dichromatischen Lichtquelle unter dem Kanal (Ulbrichtkugel mit Hochleistungs-LEDs, $\lambda_{RED} = 632\,\mathrm{nm}$ und $\lambda_{IR} = 850\,\mathrm{nm}$) und einer Kamera darüber, die senkrecht zur Wasseroberfläche durch das Wasser in die Lichtquelle blickt. Die Lichtquelle wird gepulst und die Kamera extern getriggert. Auf den Bildern befinden sich Lichtflecken, deren Position ein Maß für die Wellenneigung und deren relative Intensität ein Maß für die Wellenamplitude ist. Beide Größen werden aus den Bildern mit Mitteln der Bildverarbeitung und einfachen geometrischen Beziehungen bestimmt. Der Einfluss verschiedener Auswertemethoden auf die Neigungs- und Amplitudenverteilung wurde untersucht.

Als ein Teil der Charakterisierung des neuen linearen Wind-Wellenkanals im Institut für Umweltphysik (IUP), Heidelberg, wurde die mittlere quadratische Neigung und die mittlere Wellenhöhe bei Windgeschwindigkeiten bis zu 6.7 m/s und einer Windwirklänge zwischen 0.80 m und 2.40 m gemessen. Die Ergebnisse stimmen mit vergleichbaren Messungen in linearen Windkanälen überein.

# Contents

# 1. Introduction

The earth as a system can be divided into different subsystems, which are the cryosphere, the biosphere, the lithosphere, the atmosphere and the ocean. The interface between the two last subsystems is the water surface of the ocean, that covers more than two third of the globe. Through this interface energy, momentum, heat and matter are exchanged between the ocean and the atmosphere. Kinetic energy and momentum is transferred to the ocean by the wind, the heat flux includes sensible heat, latent heat and radiation. Matter is exchanged in solid or liquid form as dust, sea spray aerosol or precipitation or as a gas. Gas exchange is especially important in context of climate modeling, since the ocean is the main sink for anthropogenic $CO_2$ from burning fossil fuels. All exchange at the air-sea interface depends on the transport processes that are possible at the interface.

## 1.1. Air-Water Gas Exchange

In the free atmosphere and the free ocean turbulent transport governs the flow of matter. Toward the air-sea interface turbulence in the flow decreases, as it cannot penetrate the water surface. In the boundary layers directly at the interface only diffusive transport is possible. For the air-water gas exchange of low and moderately soluble gases the diffusion coefficient in water is four orders of magnitude lower than in the air, so the mass transport is limited by the diffusive boundary layer at the water side. It has a typical thickness of 100 $\mu$m [20]. Small scale waves at the water surface that vary the thickness of the diffusive layer and induce surface-near turbulence are found to increase the gas transfer significantly [21].

Gas transfer is described with the transfer velocity $k$, $[k] = \mathrm{m/s}$. Based on Fick's 1. law of diffusion, the gas transfer flux density $j$ through the water surface can be written

$$\mathbf{j} = -D\,\vec{\nabla}C \tag{1.1}$$

with the gas concentration $C$ and the diffusion constant $D$. For a constant gas concentration gradient the global flux through the diffusive boundary layer can be written

with finite increments $\Delta C$ and $\Delta l$

$$\begin{aligned} j &= -D\,\frac{\Delta C}{\Delta l} = -k\,\Delta C \\ k &= \frac{D}{\Delta l} \end{aligned} \tag{1.2}$$

$D$ is not the pure molecular diffusion constant, but an effective constant describing the whole transport process including molecular diffusion and turbulent transport. It therefore also depends on near-surface turbulence. Hence, the transfer velocity $k$ depends also on the kind of transferred gas but mainly on the transport conditions, i.e. on the thickness of the diffusive boundary layer $\Delta l$ and near-surface turbulence.

### 1.1.1. Parameterization of Air-Water Gas Exchange

To get information about the gas transfer through the air-water interface for larger areas of the ocean, the gas transfer rate has to be parameterized with a quantity that can more easily be measured. A parameterization is a empirical relation between two quantities, which is measured and also modeled, because the many processes and variables involved in the relation make a simple theoretical determination of the relation impossible.

**Parameterization with Wind Speed** The wind speed 10 m over the water surface $u_{10}$ was used as a parameter for gas transfer and many parameterizations are published, Liss and Merlivat [30], Wanninkhof [48], McGillis et al. [33], Nightingale et al. [35], see also Fig. 1.1(a). The problem is that the wind speed is not directly linked to the processes enhancing gas transfer, but the wind induced waves influence the diffusive boundary layer that limits the transport. Especially surface slicks on the water are reported to decrease the gas transfer velocity, because the decreased surface tension avoids the development of small scale waves (see e.g. [5]). Banerjee [2] shows that the global oceanic $CO_2$ uptake varies by a factor of 2 for different gas transfer parameterizations with $u_{10}$.

**Parameterization with Wave Slope** In contrast to the wind, the slope of the water surface waves as a parameter for the gas transfer is more directly linked to the interaction of the waves with the transport processes at the air-water interface. In section 2.1 it is shown that the influence of the non-linear convective term in the Navier-Stokes equation can only be neglected for small wave slopes. Hence, steep waves tend to induce turbulence that enhances gas transfer.

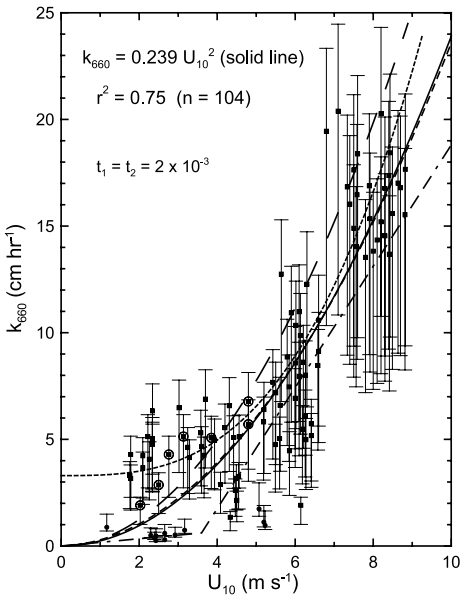


(a) Field measurements of gas transfer velocity k and parameterizations with wind speed $u_{10}$ at 10 m height

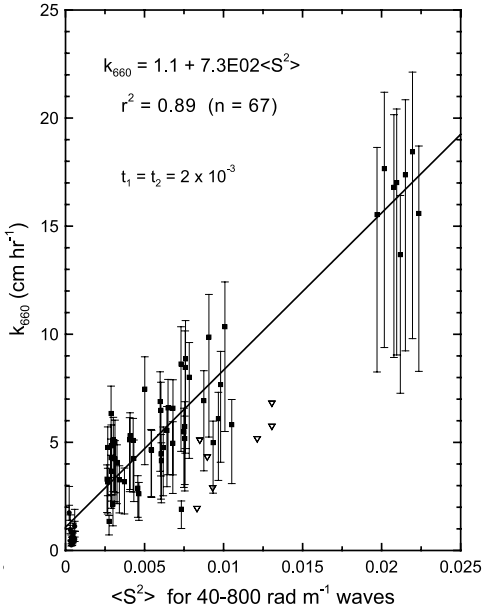


(b) Field measurements of gas transfer velocity k and parameterization with mean square slope $\langle S^2 \rangle$

Figure 1.1.: Gas transfer velocities from field measurements by Frew et al. [13]. Gas transfer velocities are determined by Schmidt number scaling of heat transfer velocities measured with infrared imagery. $k_{660}$ is the gas transfer velocity for $CO_2$, which has a Schmidt number $Sc_{CO_2} = \nu / D_{CO_2} = 660$ in seawater at 20°C. In (a) several idealized gas transfer-wind speed relations are drawn: *Nightingale et al.* (medium dash), *Wanninkhof* (long dash), *Liss and Merlivat* (short long dash), and *McGillis et al.* (short dash).

Wave breaking causes surface-near turbulence and is related to a high wave slope. Banerjee [2] reports simulations and measurements with Particle Image Velocimetry (PIV) that show a convergent surface velocity field at the face and a divergent velocity field at the back of micro-breaking waves. The breaking only occurs at high wave slopes.

Models for the transport processes at the water surface, e.g. the WOWC model (2.3), rely on the wave number spectrum of the wave field. In 2.4 it is shown that the slope integrated over all wave numbers is the mean square slope.

The ocean is observed with remote sensing methods from satellites on global scales to gain information about the sea state. The scattering properties of the ocean surface for microwave radiation ($\lambda \sim 5\,\mathrm{cm}$) from the satellites depends on the slope spectrum of the wave field. Altimeters measure perpendicular to the water surface. The highest reflected intensity is reached for a flat water surface and the intensity decreases for higher mean square slope of the water surface, so the roughness of the surface can be measured. Scatterometers use the Bragg reflection at the water surface at slant angles to determine typical wavelengths of the waves. This method is especially sensitive to small wavelengths in the range of the microwave radiation. With a reliable parameterization of the gas transfer with wave slope the estimation of the local transfer rates is improved compared to the use of $u_{10}$ parameterizations [14].

Jähne et al. [20] reports that the mean square slope is a good parameter to characterize the wave field concerning gas transfer. Fig. 1.1 shows a comparison of the parameterization of gas transfer velocities from field measurements with wind speed $u_{10}$ and mean square slope $\langle s^2 \rangle$. The parameterization with $\langle s^2 \rangle$ is more adequate. For all these reasons wave slope is a key parameter to characterize the wave field for gas exchange studies.

### 1.1.2. Gas Exchange Studies in Wind Wave Flumes

The air-sea gas exchange can be studied successfully in wind wave flumes in the laboratory. The measurement conditions such as the wave field, the wind speed and surface slicks can be controlled with the aim to understand the different processes influencing the gas transfer. More complex measurement setups are possible in the laboratory than in the field. Optical non-intrusive measurement techniques are able to show the structure of the water and air flow close to the interface. Gas concentrations can be measured in closed volumes more accurately than in the field. Since the gas transfer is dominated by small scale processes that are similar in the laboratory and in the field, the findings of laboratory measurements can be applied to understand the gas transfer between the ocean and the atmosphere. This requires comparable conditions. The wave fields in the

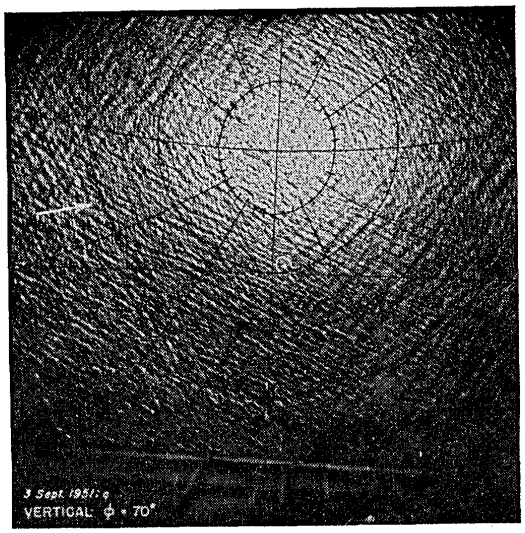


Figure 1.2.: Sun glitter image taken from a plane by Cox & Munk [8] to determine the wave slope probability distribution of ocean waves.

flumes differ from those on the ocean due to the influence of the boundary walls of the flume on the wind and water flow. The fetch, the length of the water surface in wind direction, is much smaller in linear wind wave flumes than on the ocean. In circular flumes that provide an infinite fetch secondary rotational flows due to centrifugal forces occur. Therefore, appropriate parameters as the mean square slope are necessary to describe the conditions at the air-water interface for the gas transfer.

## 1.2. Wave Measurement

A common challenge of measuring fluid flows is to find measurement techniques that do not disturb the subject of research, the flow. Therefore most of the presented methods of wave measurements work on optical principles. The different measurement techniques are presented shortly in this part. A detailed presentation of the historical development and a theoretical discussion about wave measurement techniques can be found in [19]. Citations of studies using the different wave measurement methods are given at the end of each paragraph.

**Sun Glitter - Cox & Munk** The pioneers of water wave slope measurement are Cox and Munk [8]. They took photos of the sun's reflections on the ocean surface from a plane (Fig. 1.2). The photo shows the ocean surface from a vertical view and a solar elevation of 70° from the horizon. The grid lines indicate constant slope direction

(radial) and constant total slope (closed lines) and are corrected for roll, pitch and yaw of the plane. The slope probability distribution was obtained from the intensity on the photos and mean square slope was calculated. Their measurement principle can easily be comprehended in a windy night wherever one can find a bright lantern at the border of a lake. The image of the lantern reflected into the eye of the observer by the water surface is the wider the higher the slopes on the water surface are.

**Wave Wires** Wave wires are a simple method to detect the water height at a fixed point. The resistance and the capacitance of a thin metal wire that penetrates the water surface perpendicularly depends on the water height, so the water height signal can be easily transformed to a voltage signal. Thin wires are necessary not to disturb the wave motion. For long gravity waves wave wires are an appropriate measurement method. But especially for small scale waves the wires represent obstacles in the wave field that reflect waves and damp the fluid motion. The time resolution is limited by the fact that the water in contact with the wire does not follow fast motions of the water surface due to adhesion. The scanning frequency can be up to 100 Hz [46]. For a linear dispersion relation $k = \frac{\omega}{c}$ and a minimal phase velocity $c = 0.2\,\mathrm{m/s}$ the minimal wavelength detected with this frequency is $\lambda = 1.2\,\mathrm{cm}$. Hence, small capillary waves are not detected. The spatial resolution is limited by the distance between the installed wires. Arrays of wave wires yield information of the wave direction. [7].

**Stereo Imaging** Stereo imaging can be applied to obtain depth information from photographs. The water surface is imaged with two cameras from two different angles and depth information is obtained from the different position of corresponding objects in the two images. Corresponding objects in the two images have to be found which is referred to as the correspondence problem. On the water surface it happens that an object in one image is not mapped in the second image, because the water surface is specular reflecting surface, so light from a light source is reflected only to a small range of angles. Hence, light might be reflected just in one of two cameras. The height resolution of stereo imaging is not sufficient to measure small scale waves. [46], [15].

**Reflective Slope Gauge (RSG)** The reflective slope gauge is based on the reflection of light on the water surface. In contrast to the sun glitter method of Cox, an artificial light source is used. It is arranged in a fixed geometry with a camera, so the slope can be determined from the position of the reflected light speckles in the images. No parts of the RSG have to be submerged, so a RSG is suitable for the field, e.g. measurements from ships. Problems occur because only about 2 % of the incident light on the surface

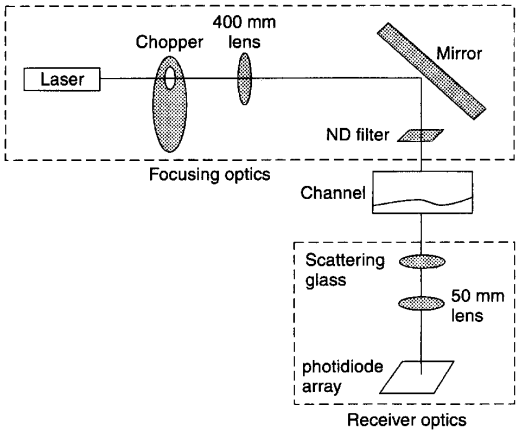


Figure 1.3.: Laser Slope Gauge (LSG) used by Duke et al. [11]. The laser beam is chopped with a frequency of 285 Hz, so frequency spectra can be obtained.

is reflected, so the signal has to be separated from the background intensity.[28].

**Laser Slope Gauge (LSG)** Laser Slope Gauges are used for the majority of wave slope measurements. The method is based on the refraction of a Laser beam at the water surface from which the slope can be determined. The deviation of the beam is detected with a photo diode array or a camera. Fig. 1.3 shows an Laser slope gauge used by Duke et al. [11]. The Laser beam is focused on the water surface where it has a width of less than 0.1 mm. Under the channel the beam hits a scattering glass which acts as an image plane. It is focused to a photodiode array where the position of the beam is detected.

For a scanning Laser Slope Gauge the beam is scanned over the water surface with a moving mirror to obtain spacial information about the slope. A slope image can be obtained from which frequency wave number spectra are calculated. For this method the Laser or the receiver must be submerged. An example of a LSG field measurement with a small catamaran can be found in [4].

**Imaging Slope Gauge (ISG)** The imaging slope gauge provides complete slope images from the water surface. It is based on refraction. A camera above the water surface looks into a extended light source under the water surface that has a color (CISG) or intensity distribution, so each the position on the light source is uniquely coded by a color or an intensity. Hence, each pixel in an image can be mapped to slope coordinates according to its color. These slope measurements have the best spacial and temporal resolutions of all wave measurement techniques. High resolution wave spectra can be

obtained from the data. Since the light source must be submerged, it is difficult to employ the ISG in the field. [1], [15], [39], [40].

**Polarimetric Imaging** The reflection coefficient on the water surface depends on the polarisation of the light. Therefore polarimetric imaging can be used to determine the slope of the water surface. Zappa et al. [49] image the water surface illuminated with unpolarized skylight to determine the slope from the polarization of the reflected light.

### 1.2.1. Discussion of Wave Measurement Techniques

The wavelength of water waves covers a range from millimeters to several meters. As the principal shape of the waves is similar for all wavelengths, the wave amplitude also has a wide dynamic range of several orders of magnitude. Therefore, it is difficult to develop a wave gauge that can measure the wave height in this wide dynamic range. In contrast to this, by measuring the wave slope the contribution of waves of all wavelengths can be captured. The majority of the wave gauges measure the wave slope optically, since it is accessible by the effects of refraction and reflection.

Slope gauges based on reflection are suitable for field measurements as no submerged parts are necessary. But disadvantages are the small amount of reflected light and the limited range of slope. Refractive slope gauges are suitable for slope measurements in flumes. They can detect a higher range of slope than the reflective slope gauge in the same field of view, which is an advantage in narrow flumes.

The dependence of the slope measurement on the water height is a problem especially for optical refractive methods, when the water height changes the geometry of the slope gauge. This can be avoided with telecentric optics [39]. The Imaging Slope Gauge has telecentric optics at the light source, so the color code of an emitted light ray does only depend on its angle to the optical axis. Hence, the distance to the water surface where the light ray is refracted into the camera does not matter. Telecentric optics on the detector side are also used for Laser Slope Gauges.

The state of the art method with the best spacial and temporal resolution to obtain wavenumber frequency spectra of the water surface is the Color Imaging Slope Gauge (CISG). However, a complex calibration procedure is necessary to determine the functional relation between the color code and the slope. Therefore, a simple method is developed in this study that allows for the determination of the statistical parameters of the wave field.

## 1.3. Goal of This Study

The goal of this study is to develop an optical device for a combined measurement of statistical parameters of a rough water surface populated with wind induced waves, namely the probability distributions for the wave height and wave slope. The main focus is set on building a wave gauge that is based on simple physical principles, so it can be put up and calibrated in a relatively short time. Moreover, it is aimed for a characterization of the mean square slope relation vs the friction velocity in the new linear wind wave flume. It is intended that the instrument measures the wave parameters along with gas exchange measurements.

# 2. Theory of Water Waves

## 2.1. Navier-Stokes Equation

The Navier-Stokes equation is Newton's law of motion $F = m\,a$ for an infinitesimal small volume of fluid. The differential equation in the Eulerian representation describes the evolution of a velocity field $\mathbf{u}$ in time. It is a formulation of the conservation of momentum and the terms have units of a force density. A fluid is called Newtonian fluid, if it has a normal viscous behavior, i.e. if the fluid flows over a plate as a shear flow with a constant velocity gradient $du/dz$ (see Fig. 2.2), it exerts a shear stress $\sigma$ to the ground plate, which can be expressed by

$$\sigma = \mu \frac{du}{dz} \tag{2.1}$$

with the constant absolute viscosity $\mu$. The fluid is incompressible, if its density $\rho$ is constant in time. For an incompressible Newtonian fluid the Navier-Stokes equation in the Langrangian representation is

$$\rho \frac{D\mathbf{u}(\mathbf{x_0}(t), t)}{Dt} = -\nabla p + \rho \mathbf{g} + \mu \nabla^2 \mathbf{u} \tag{2.2}$$

$\mathbf{u}(\mathbf{x_0}(t), t)$ is the velocity of a fluid particle at the point $\mathbf{x_0}(t)$, so the system is described in the Langrangian representation where the observer follows the particles. $\frac{D}{Dt}$ is the material derivative or particle derivative and describes the total rate of change of the velocity of the particle. In the Eulerian representation the velocity of a fluid is described as a velocity field, with a fixed coordinate system. In this representation the Navier-Stokes equation is

$$\rho \left[ \frac{\partial \mathbf{u}}{\partial t} + (\mathbf{u}\nabla)\mathbf{u} \right] = -\nabla p + \rho \mathbf{g} + \mu \nabla^2 \mathbf{u} \tag{2.3}$$

with the velocity field $\mathbf{u}(\mathbf{x}, \mathbf{t})$.

The right hand side of Eq. (2.3) can be parted in two surface forces and one volume or body force. The surface forces are the pressure force $\nabla p$ as a normal surface force and the viscous friction force $\mu \nabla^2 \mathbf{u}$ as a tangential surface force. The gravitational force $\rho \mathbf{g}$ is a body force that acts on the whole volume of the fluid particle. $(\mathbf{u}\nabla)\mathbf{u}$ is the convective term and leads to an acceleration of the fluid particle, due to a spacial

change of the velocity in the velocity field $\mathbf{u}$. The term is non-linear and the reason for turbulence in hydrodynamic flows. A detailed derivation of the Navier-Stokes equation can be found in [27].

The following comparison of the two left hand terms in Eq. (2.3) for the fluid motion in a water surface wave shows that the non-linear term can only be neglected for wave slopes $s \ll 1$ [28]. This indicates that for higher slopes turbulence may occur due to the non-linearity.

We assume a plane wave in one dimension with the amplitude $A$.

$$h(x,t) = A\,cos(kx - \omega t) \tag{2.4}$$

The slope of the wave and the velocity of the fluid particles are

$$s = \frac{\partial h(x,t)}{\partial x} \propto A\,k \tag{2.5}$$

$$u = \frac{\partial h(x,t)}{\partial t} \propto A\,\omega \tag{2.6}$$

The acceleration of the fluid particles and the velocity gradient are

$$\frac{\partial u}{\partial t} \propto A\,\omega^2 \tag{2.7}$$

$$\frac{\partial u}{\partial x} \propto A\,k\,\omega \tag{2.8}$$

The terms $(\mathbf{u}\nabla)\mathbf{u}$ and $\frac{\partial \mathbf{u}}{\partial t}$ are composed from the derivatives

$$\frac{\partial \mathbf{u}}{\partial t} \approx \frac{\partial u}{\partial t} \propto A\,\omega^2 \tag{2.9}$$

$$(\mathbf{u}\nabla)\mathbf{u} \approx u\,\frac{\partial u}{\partial x} \propto A^2\,\omega^2\,k \tag{2.10}$$

For a neglect of the non-linear convective term $(\mathbf{u}\nabla)\mathbf{u}$ it has to be much smaller than the local acceleration $\frac{\partial \mathbf{u}}{\partial t}$

$$(\mathbf{u}\nabla)\mathbf{u} \ll \frac{\partial \mathbf{u}}{\partial t} \tag{2.11}$$

This condition expressed in constants of the plane wave with Eq. (2.9) and 2.10 leads to

$$A\,k \ll 1 \tag{2.12}$$

$A\,k$ can be identified with the slope of the wave due to Eq. (2.5). Hence, the fluid motion in a wave with a slope much smaller than 1 is described by a linear differential equation. For higher wave slopes of the magnitude 1 the non-linear term can not be neglected and can lead to instabilities that might enhance the near-surface turbulence.

The Navier-Stokes equation can be analyzed numerically. Fluid dynamic simulations of wind induced water waves are reported by Tsai and Hung [44], [43]. Difficulties arise from the fact that the boundary conditions for the water flow are not stationary, because the water surface is a free surface that changes in time.

## 2.2. Water Surface Waves

Under the assumption of a small amplitude, water waves can be treated as linear waves. The dispersion relations for different regimes of linear waves are shown. Some effects of non-linear waves are described.

### 2.2.1. Linear Waves

Water waves with a small amplitude $h(\mathbf{x}, t)$, i.e. $h \ll \lambda$ (wavelength $\lambda$) and $h \gg H$ (water height $H$), obey the linear wave equation [27]

$$\frac{\partial^2 h(\mathbf{x}, t)}{\partial t^2} = c^2 \nabla^2 h(\mathbf{x}, t) \tag{2.13}$$

The wave is assumed to be a plane wave $h = A\,cos(kx - \omega t)$, which is constant in y-direction and propagates in x-direction. The continuity equation for velocities in the water $u = \frac{\partial x}{\partial t}$ and $w = \frac{\partial z}{\partial t}$ in a incompressible fluid

$$\frac{\partial u}{\partial x} + \frac{\partial v}{\partial z} = 0 \tag{2.14}$$

leads to a Laplace equation for the velocity potential (velocity $\vec{v} = \nabla\Theta$)

$$\frac{\partial^2 \Theta}{\partial x^2} + \frac{\partial^2 \Theta}{\partial z^2} = 0 \tag{2.15}$$

With the assumption of a plane wave as the boundary condition for the water surface, the velocity potential $\Theta$ can be solved with respect to the dynamic boundary conditions at the water surface and at the ground [27].

The dispersion relation for these plane water surface waves is

$$\omega(k) = \sqrt{gk\,\tan kH} \tag{2.16}$$

with the gravitational constant $g$ and wave number $k = \frac{2\pi}{\lambda}$. The surface tension $\sigma$ ($[\sigma] = \frac{\mathrm{N}}{\mathrm{m}}$) of the water surface is a line force, which has to be applied to the surface to increase its area. It is an additional term for the restoring force, so the dispersion relation becomes

$$\omega(k) = \sqrt{\left(gk + \frac{\sigma k^3}{\rho}\right) \tanh kH} \tag{2.17}$$

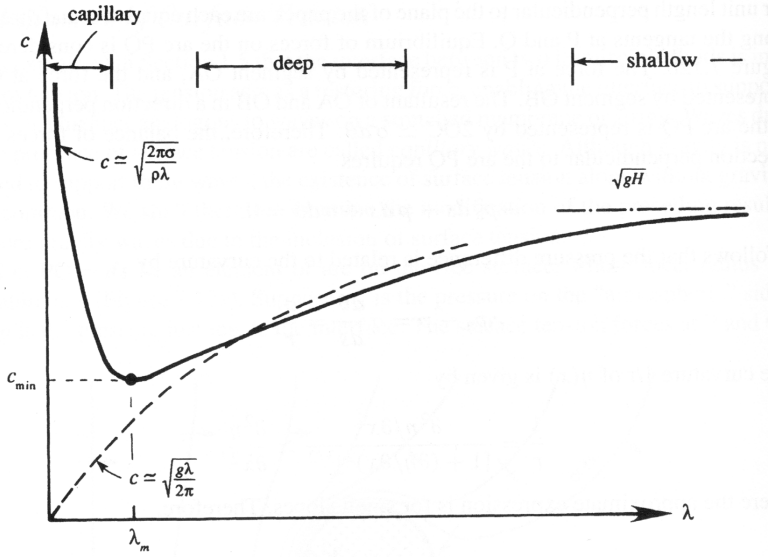


Figure 2.1.: Phase velocity c of water surface waves as a function of their wavelength $\lambda$. Water waves can be parted in three wave regimes depending on their dispersion relation: capillary waves (surface tension $\sigma$ dominant) and gravity waves (gravitation g dominant) in the deep water approximation and in the shallow water approximation. $\lambda_m = 1.73\,\text{cm}$ and $c_{min} = 23.2\,\frac{\text{cm}}{\text{s}}$ for standard conditions (from [27]).

with the density $\rho$. The phase velocity $c$ of the waves is

$$c = \frac{\omega(k)}{k} = \sqrt{\left(\frac{g}{k} + \frac{\sigma k}{\rho}\right) \tanh kH} = \sqrt{\left(\frac{g\lambda}{2\pi} + \frac{2\pi\sigma}{\lambda\rho}\right) \tanh \frac{2\pi H}{\lambda}} \tag{2.18}$$

Hence, three different regimes of waves can be defined regarding the dependence of the phase velocity $c$ on wavelength $\lambda$ and water height $H$ which is shown in Fig. 2.1.

- Capillary waves. For the capillary waves at wavelengths $\lambda \leq \lambda_m$ the surface tension becomes dominant as the restoring force. $\lambda_m = 1.73\,\text{cm}$ for ambient conditions and clean water. For these waves in the mm range $\tanh \frac{2\pi H}{\lambda} \approx 1$, so the phase speed is $c = \sqrt{\frac{2\pi\sigma}{\lambda\rho}}$. The dispersion is negative, i.e. smaller waves propagate faster.

- Gravity waves, deep water. For gravity waves in deep water $\tanh \frac{2\pi H}{\lambda} \approx 1$, and the dominant restoring force is gravity, so the phase velocity is $c = \sqrt{\frac{g\lambda}{2\pi}}$. This is the case for waves with $\lambda_m \ll \lambda \ll H$.

- Gravity waves, shallow water. For a wavelength $\lambda$ in the same order of magnitude as the water height $H$ the hyperbolic tangent can be approximated as $\tanh \frac{2\pi H}{\lambda} \approx$

$\frac{2\pi H}{\lambda}$, so the phase velocity becomes independent of the wavelength $c = \sqrt{gH}$, but depends on the water height $H$. This is the reason for refraction of large waves in shallow water close to the beach.

The general solution to the wave equation (Eq. (2.13)) is a superposition of all special solutions, i.e. the sum of all plane waves $h(\mathbf{x}, t) = A\,cos(\mathbf{kx} - \omega t)$. But water waves are only linear as long as the restoring forces are linear in the amplitude. In this case the single wave components cannot interact or disturb each other and their shape remains constant in time. A wave field consisting of a superposition of two sinusoidal waves with two different wavelengths will be composed of these wavelengths for all times. Its spectrum is stationary.

### 2.2.2. Non-linear Waves

The propagation of non-linear waves is described by non-linear differential equations. Single solutions of the differential equations cannot be superposed to new solutions, so the propagation of the wave field in time and space depends on all wavelengths. Some effects of non-linearity on the wave field are listed below.

- Stokes waves and solitary waves. All waves with a non-sinusoidal shape are composed from a spectrum of sine waves. They spread due to dispersion, because sine waves with different wavelengths have different phase speed. The effect of non-linear steepening can balance this effect, so non-sinusoidal waves with a stationary shape are possible. For Stokes waves that occur in deep water the wave speed depends on the wave amplitude, so the dispersion can be balanced. Solitary waves occur in shallow water and the non-linearity is linked to the water height [27].

- Wave-wave interactions. A concept of the coupling of waves with different wavelengths is similar to that for phonons in solid state physics. Coupling happens between four waves in a certain interaction time. The wave number vectors of the four waves $k_1 + k_2 + k_3 + k_4 = 0$ (conservation of momentum) and the frequencies $\omega_1 + \omega_2 + \omega_3 + \omega_4 = 0$ (conservation of energy) are added. Coupling constants between the different wave modes are used. With these models, the energy transfer from one to another wave mode is described, so equations can be obtained, that describe the evolution of the wave spectra in time [26]. A big contribution to the development of these models was done by Phillips [36]. An example for a wave-wave interaction is the presence of parasitic capillary waves on the downwind face of larger gravity waves [12], [10], [50].

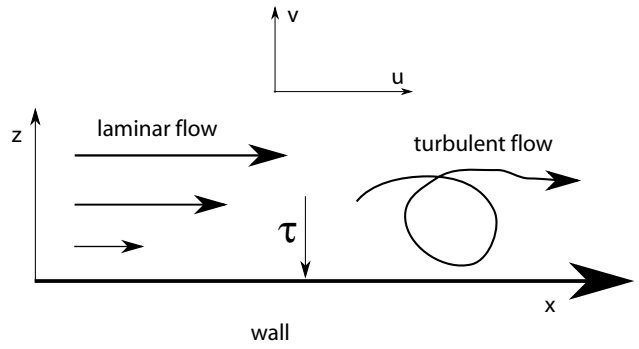


Figure 2.2.: Coordinate system for the momentum flux $\tau$

- Wave breaking is a vivid example for a non-linear process. Wave energy is transferred from a larger wave partly to smaller waves and partly the energy dissipates.

## 2.3. Wave Generation

When wind blows over a flat water surface, at first small scale waves are formed. They increase the roughness of the surface, so the wind can more effectively create small waves and later higher waves. The processes that change the wave field are governed by the fluxes of momentum and energy from the air flow into the water.

The fetch is an important parameter for the development of a wave field. It is the length on which the wind conditions are constant, so energy and momentum can be transferred into the wave field that propagates mainly in wind direction. For large depressions on the ocean the fetch can reach a length of $\sim 1000\,\mathrm{km}$. However, small scale waves in the mm wavelength range can already be observed after a fetch of $\sim 10\,\mathrm{cm}$.

**Momentum Transport into the Water and Friction Velocity** The following calculations can be found in [41]. For the definition of the coordinate systems see Fig. 2.2. Let us first consider the case of a laminar flow over a plane plate. The shear flow exerts a force to the plate parallel to the shear flow, the shear stress $\sigma$. This is a force per area $A$ of the plate and can be written

$$\sigma = \frac{F_{shear}}{A} = \rho\,\nu\frac{du}{dz} \tag{2.19}$$

with the kinematic viscosity $\nu$ of the fluid. The shear stress is equal to the momentum flux density $\tau$. $\tau$ can be written in the representation of Fick's 1. law for the diffusive

flow $j$ of a quantity Q.

$$j = -D\frac{dQ}{dz} \tag{2.20}$$
$$Q = \rho u \tag{2.21}$$
$$\tau = -\nu\frac{\rho\, du}{dz} = -\sigma \tag{2.22}$$

The quantity $Q$ transported here is the momentum density for momentum in x-direction $\rho u$, which is transported in the negative z-direction.

For a turbulent flow, momentum density is transported by turbulent mixing instead of viscous forces. $\tau$ can be written in a similar way but with a different viscosity, the eddy viscosity $\nu_e$, which is the turbulent diffusion constant for the momentum transport depending on the turbulent flow field.

$$\tau = \nu_e\frac{\rho\, du}{dz} \tag{2.23}$$

The instantaneous momentum flux at a point in the flow is

$$\tau = (\rho u(\mathbf{x},t))\, v(\mathbf{x},t). \tag{2.24}$$

The instantaneous momentum density $\rho u(\mathbf{x},t)$ is transported in z-direction with the velocity v($\mathbf{x}$,t). But in the turbulent flow $u$ and $v$ are highly variable in time, so the momentum flux density $\tau$ has to be averaged.

$$\tau = \langle\tau\rangle = \langle(\rho u)v\rangle = \rho\,\langle uv\rangle \tag{2.25}$$

The density $\rho$ is constant and the velocities are split into a mean part $\langle u\rangle$ and a fluctuating part $u'$.

$$u = \langle u\rangle + u' \tag{2.26}$$
$$v = \langle v\rangle + v' \tag{2.27}$$
$$\langle v\rangle = 0$$
$$\langle u'\rangle = \langle v'\rangle = 0$$

Thus, the momentum flux density is

$$\tau = \rho\,\langle uv\rangle = \rho\,\langle(\langle u\rangle + u')(\langle v\rangle + v')\rangle \tag{2.28}$$
$$= \rho\,\langle u'v'\rangle$$

Momentum density is only transferred by correlated fluctuations of both velocities $u$ and $v$. In the pure turbulent case, the friction velocity $u_*$ is defined by the correlation

of these velocity fluctuations and indicates the velocity of the momentum transfer by the turbulent flow.

$$u_*^2 = \langle u'v' \rangle \tag{2.29}$$

The friction velocity is generally defined as

$$u_*^2 = \frac{\tau}{\rho} \tag{2.30}$$

and is used for studies of all different effects of the wind on the water surface, because in contrast to the wind speed it does not depend on the height and characterizes the amount of momentum transferred to the water. In the water the momentum is divided into two parts. The main fraction is transferred to waves on the water surface, a smaller fraction goes into a mean water current in wind direction [34].

**Logarithmic Wind Profile** The wind profile is the horizontal wind velocity $u$ as a function of the height above the water surface $z$. With the assumption that the change of the wind velocity over the water surface $\frac{\partial u}{\partial z}$ only depends on the height $z$ and the friction velocity $u_*$, the only possible combination of these quantities with regard to the dimensions leads to a differential equation for the wind velocity.

$$\frac{\partial u}{\partial z} = \frac{1}{\kappa} \frac{u_*}{z} \tag{2.31}$$

The solution of this equation is the logarithmic wind profile with the surface roughness $z_0$ and the dimensionless empirical von Karman constant $\kappa \approx 0.4$.

$$u(z) = \frac{u_*}{\kappa} ln \left( \frac{z}{z_0} \right) \tag{2.32}$$

Measurements of the wind profile enable the determination of the friction velocity $u_*$.

**Wind-Wave Coupling** The description of the process leading to the formation and growth of wind induced water waves is very difficult. The main problem of models for the interaction of the wind with the water surface is, that the air flow is changed by the waves that occur at the surface. Therefore, no constant boundary conditions can be set for either of the two fluids. With a more abstract formulation, the problem could be described as a turbulent flow of a fluid (air) over another denser fluid with a free surface (water), which both become unstable and turbulent at the interface. Turbulence is a chaotic process, where the velocities of nearby particles can be totally different, so only statistical considerations about the flow can be made.

Wind-wave models all deal with the wave field as the subject of research. It is represented by its spectrum (see 2.4). The wave field is changed by energy and momentum

fluxes, that are themselves dependent on the wave field. Energy and momentum is provided by the wind.

The wind-wave model WAM (Wave Analysis Model) was published in 1988 by the WAMBDI group [47]. It is well established for wave predictions on the ocean. It is based on energy $E$ and momentum $\mathbf{P}$ transport equations for the wave field.

$$\frac{\partial E}{\partial t} + (\mathbf{u} + \mathbf{c_g}) \cdot \nabla E = S_{in} - S_{ds} \tag{2.33}$$

$$\frac{\partial \mathbf{P}}{\partial t} + (\mathbf{u} + \mathbf{c_g}) \cdot \frac{\partial \mathbf{P}}{\partial x} = \tau^w - \tau^o \tag{2.34}$$

The equations include an advective transport with a water current velocity $\mathbf{u}$ and wave field group velocity $\mathbf{c_g}$. The right hand terms are source terms due to the wind and sink terms due to dissipation [24].

Another model is the WOWC (Wind-Over-Waves Coupling) model published by Makin [32] (see also [7]). It models the different effects of wind drag on the water that are sinks for the momentum flux $\tau$.

$$\tau_{total} = \tau^{\nu} + \tau_w + \tau_{s_d} + \tau_{s_{eq}} \tag{2.35}$$

with $\tau^{\nu}$ the viscous drag, $\tau_w$ the wave induced drag for a smooth air flow, and $\tau_{s_d}$ and $\tau_{s_{eq}}$ the drag due to air flow separation behind steep waves in different parts of the spectrum.

## 2.4. Wave Number Spectrum

The water surface amplitude $h(\mathbf{x}, t)$ can be represented as a wave number frequency spectrum. The wave number frequency spectrum $\hat{H}$ is the energy spectrum of the water surface amplitude, i.e. the square of the Fourier transformed surface amplitude. The energy of a signal, here the amplitude of the water surface, is proportional to the square of its amplitude.

$$\hat{h}(\mathbf{k}, \omega) = \int_{\mathbf{x}} \int_{t} h(\mathbf{x}, t) e^{-i(\mathbf{kx} - \omega t)} \, d\mathbf{x} \, dt \tag{2.36}$$

$$\hat{H}(\mathbf{k}, \omega) = |\hat{h}(\mathbf{k}, \omega)|^2 \tag{2.37}$$

$$F(\mathbf{k}) = \int_{\omega} \hat{H}(\mathbf{k}, \omega) d\omega \tag{2.38}$$

$F(\mathbf{k})$ is the wave number spectrum, which is obtained as the integration over all frequencies $\omega$ of the wave number frequency spectrum. The variance $\sigma_h^2$ of the water surface amplitude $h(\mathbf{x}, t)$, later referred to as *mean square wave height*, can be obtained from

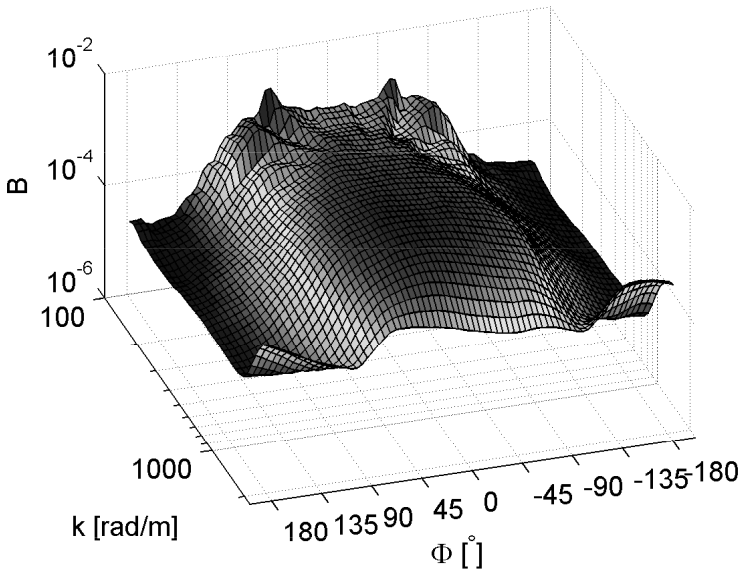


Figure 2.3.: 2-dim directional wave spectrum from Rocholz [40]. The 2-dim wave number vector $\mathbf{k}$ is represented with its norm and angle $\theta$ to the wind direction: $\mathbf{k} = (|\mathbf{k}|, \theta)$. In this representation the direction of the waves is visible. According to this spectrum, most of the wave energy can be found in waves that propagate in wind direction with an angle of $|\phi| < 90°$.

the wave number spectrum $F(\mathbf{k})$.

$$\sigma_h^2 = \langle h^2 \rangle - \langle h \rangle^2 = \langle h^2 \rangle = \frac{1}{A} \int_A |h(x,y)|^2 d\mathbf{x} = \int |\hat{h}(\mathbf{k})|^2 d\mathbf{k} = \int F(\mathbf{k}) d\mathbf{k} \tag{2.39}$$

with $A$ the area of the whole wave field. In the fourth transformation is Parseval's theorem is applied.

In the same way the mean square slope of the water surface $\sigma_s^2$ is connected with the slope energy spectrum. For the slope component in x-direction this is

$$\begin{aligned} s_x(\mathbf{x}) &= \frac{\partial h(\mathbf{x})}{\partial x} && (2.40) \\ \hat{s_x}(\mathbf{k}) &= ik_x \hat{h}(\mathbf{k}) && (2.41) \\ \sigma_{s_x}^2 &= \langle s_x^2 \rangle - \langle s_x \rangle^2 = \langle s_x^2 \rangle = \frac{1}{A} \int_A |s_x(\mathbf{x})|^2 d\mathbf{x} = \int |\hat{s_x}(\mathbf{k})|^2 d\mathbf{k} && (2.42) \\ &= \int |ik_x \hat{h}(\mathbf{k})|^2 d\mathbf{k} = \int k_x^2 |\hat{h}(\mathbf{k})|^2 d\mathbf{k} = \int k_x^2 F(\mathbf{k}) d\mathbf{k} \end{aligned}$$

The total mean square slope is

$$\sigma_s^2 = \sigma_{s_x}^2 + \sigma_{s_y}^2 = \int k_x^2 |\hat{h}(\mathbf{k})|^2 d\mathbf{k} + \int k_y^2 |\hat{h}(\mathbf{k})|^2 d\mathbf{k} = \int \mathbf{k}^2 F(\mathbf{k}) d\mathbf{k} \tag{2.43}$$

with the slope energy spectrum $S(\mathbf{k}) = \mathbf{k}^2 F(\mathbf{k})$. Hence, the two integral quantities mean square slope $\sigma_s^2$ and mean square wave height $\sigma_h^2$ are obtained from the energy

spectra for water surface amplitude and slope by an integration over all wave numbers (see [1], [22], [37]).

In literature saturation wave number spectra $B(\mathbf{k})$ are common with the dimensionless spectral density $B$. It is defined as $B(\mathbf{k}) = S(\mathbf{k})\mathbf{k}^2 = F(\mathbf{k})\mathbf{k}^4$ and was first introduced by Phillips [36]. Fig. 2.3 shows a directional wave spectrum from Rocholz [40] measured with a Color Imaging Slope Gauge (CISG).

## 2.5. Statistical Water Surface - Probability Density Function for Wave Amplitude and Slope

The individual hydrodynamical processes in water surface waves are still a current subject of research and partly not yet understood. But the water surface can be seen as a statistical system and probability distribution functions for the wave amplitude and the slope can be obtained.

**Linear Superposition Wave Model** Longuet-Higgins [31] assumes the surface amplitude $h(\mathbf{x}, t)$ to be a linear superposition of an infinite number of plane waves with amplitude $c_n$ and an arbitrary phase $\epsilon \in [0, 2\pi]$. This is a valid description for the water surface for small slopes (2.1).

$$h(\mathbf{x}, t) = \sum_n^\infty c_n \cos\left(\mathbf{kx} - \omega(\mathbf{k})t + \epsilon\right) \tag{2.44}$$

These linear waves propagate without interaction, so the surface elevation at a fixed point in space and time $h(\mathbf{x_0}, t_0)$ is the sum of an infinite number of independent random variables with vanishing average. Therefore, according to the the central limit theorem the probability density function (pdf) for the surface elevation is a normal distribution

$$p_h(h) = \frac{1}{\sqrt{2\pi}\,\sigma_h} e^{-\frac{h^2}{2\,\sigma_h^2}} \tag{2.45}$$

With the linear superposition wave model the wave slopes in x and y direction are

$$s_x(\mathbf{x}, t) = \frac{\partial h(\mathbf{x}, t)}{\partial x} = -\sum_n^\infty k_x\, c_n \sin\left(\mathbf{kx} - \omega(\mathbf{k})t + \epsilon\right) \tag{2.46}$$

$$s_y(\mathbf{x}, t) = \frac{\partial h(\mathbf{x}, t)}{\partial y} = -\sum_n^\infty k_y\, c_n \sin\left(\mathbf{kx} - \omega(\mathbf{k})t + \epsilon\right), \tag{2.47}$$

so the two slope components at a fixed point in space and time are also the sum of an infinite number of random variables with a vanishing average and the central limit

theorem also applies. The 2-dim pdf for both slope components is a normal distribution

$$\begin{aligned} p_{s_x,s_y}(s_x,s_y) &= \frac{1}{2\pi\sqrt{\Delta}} e^{-\frac{1}{2\Delta}\left(s_x^2\langle s_y^2\rangle - 2\langle s_x s_y\rangle s_x s_y + \langle s_x^2\rangle s_y^2\right)} \\ \Delta &= \langle s_x^2\rangle\langle s_y^2\rangle - \langle s_x\, s_y\rangle^2 \end{aligned} \tag{2.48}$$

For the case of the x-axis parallel and y-axis perpendicular to the wind direction, the two slope components are independent and mixed terms in (2.48) cancel: $\langle s_x\, s_y\rangle = \langle s_x\rangle\langle s_y\rangle = 0$. The slope distribution becomes

$$\begin{aligned} p_{s_x,s_y}(s_x,s_y) &= \frac{1}{2\pi\,\sigma_{s_x}\,\sigma_{s_y}} e^{-\frac{1}{2}\left(\frac{s_x^2}{\sigma_{s_x}^2}+\frac{s_y^2}{\sigma_{s_y}^2}\right)} \\ \sigma_{s_x}^2 &= \langle s_x^2\rangle \\ \sigma_{s_y}^2 &= \langle s_y^2\rangle \end{aligned} \tag{2.49}$$

Hence, the slope pdf can be separated

$$p_{s_x,s_y}(s_x,s_y) = p_{s_x}(s_x)\,p_{s_y}(s_y), \tag{2.50}$$

so the variances $\sigma_{s_x}^2$ and $\sigma_{s_y}^2$ can be determined separately.

**Non-linear Interactions - Gram-Charlier Distribution** For real wave fields the pdf's for surface amplitude $p_h(h)$ and slope $p_{s_x,s_y}(s_x,s_y)$ deviate from a normal distribution. Due to non-linear wave-wave interaction some of the assumptions for the central limit theorem are violated. For example, the phase of parasitic capillary waves is coupled with the phase of the dominant wave, the capillaries appear on. Furthermore, the ideal representation of the wave field as a linear superposition of plane waves (2.44) becomes invalid when the non-linear term in the wave equation is important for higher slopes. These effects on the slope pdf can be modeled with a Gram-Charlier (GC) distribution. It is a correction of the Gaussian normal distribution with Hermite polynomials $H_i$

$$p_{GC}(s_x,s_y) = p_{normal}(s_x,s_y) \times \left[1 + \sum_{i,j=1}^{\infty} c_{ij}\, H_i\left(\frac{s_x}{\sigma_{s_x}}\right) H_j\left(\frac{s_x}{\sigma_{s_x}}\right)\right] \tag{2.51}$$

The coefficients can be determined by a fit to the slope data. A further description can be found in [8], [29].

Plant [38] shows that the shape of the slope pdf can also be calculated from a model that assumes independent bound and free waves. The slope distribution of both follows a Gaussian distribution, but with a non-zero mean slope. The sum of both distributions yields the total slope pdf, which agrees with the Gram-Charlier distribution.

# 3. Experimental Setup and Measurement Principles

## 3.1. Setup

The setup of the slope gauge is shown in Fig. 3.1 and Fig. 3.2. It can be classified as a Refractive Slope Gauge, but is referred to in this study as Ulbricht Sphere Slope Gauge (USSG) to name this special measurement device. The main parts are the Ulbricht sphere with a LED light source that is positioned under the wind wave flume and the camera above. The camera is adjusted so that its optical axis is perpendicular to the water surface. It looks directly into the light source in a way, that the light source is centered in the image. Only light rays passing the water surface at a certain slope are refracted into the camera, which gives the possibility to determine the local slope of the water surface. The LED light source emits light with two different wave lengths ($\lambda_{RED} = 632\,\mathrm{nm}$, $\lambda_{IR} = 850\,\mathrm{nm}$) with a difference in the absorption coefficients for water of one order of magnitude. Hence, the water height can be measured based on the effect of absorption in the water. Therefore, two images have to be taken of the water surface with an IR and a RED illumination in a short time. Since the frame rate of the camera is limited to 200 Hz, the LEDs are pulsed in a way that the effective exposure times for the images are short and two images can be taken from the same state of the water surface. The LED pulses and the camera trigger signal are provided by a electronic control unit.

## 3.2. Lightsource and LED control unit

An Ulbricht sphere with four high power LEDs is used as the light source for the USSG. A special control unit sets the time pattern for the flashed LEDs and triggers the camera. Below both parts are described.

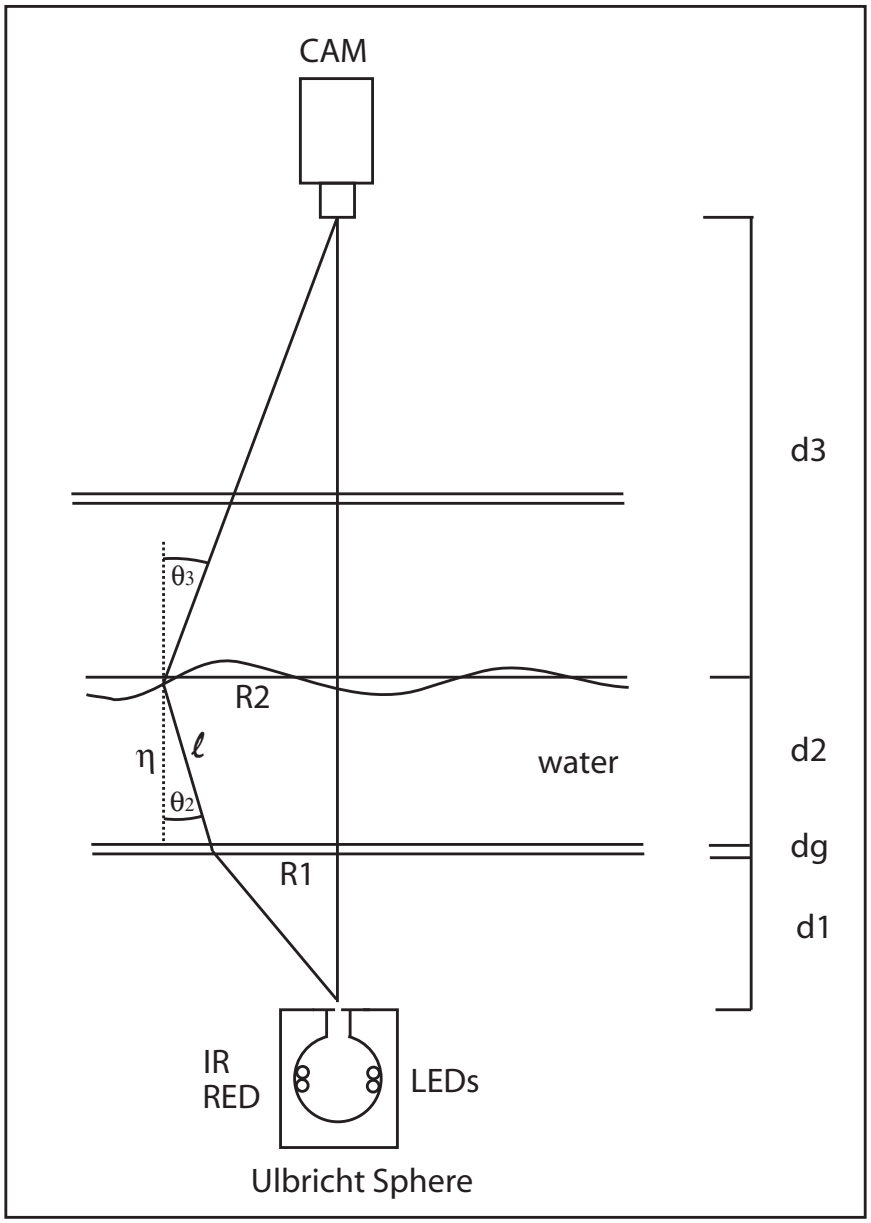


Figure 3.1.: Schematic sketch of the experimental setup of the wave gauge

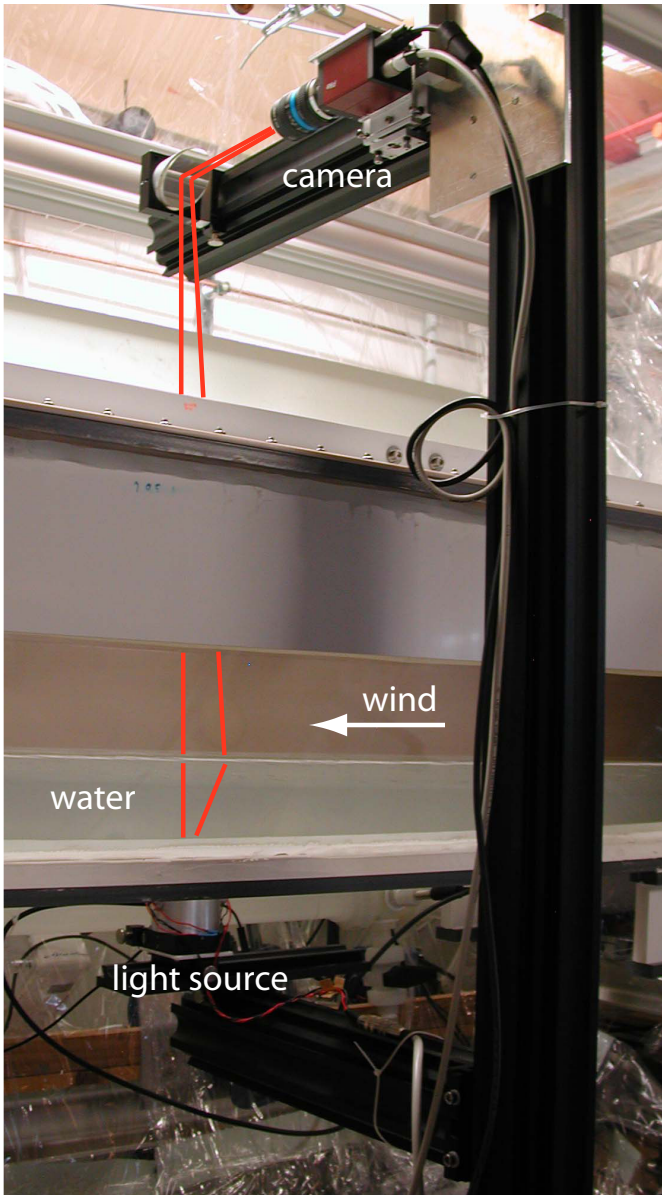


Figure 3.2.: The whole experimental setup at the wind wave flume. Two light rays are drawn, one of which passes the water surface at slope $s = 0$ and the other at a slope $s > 0$. The whole wave gauge is fixed on a cantilever that can be moved along the flume.

| LED type | OSRAM SFH 4230 | OSRAM LR W5SN-JYKY-1 |
|---|---|---|
| peak wavelength $\lambda$ [nm] | 850 | 632 |
| spectral bandwidth $\Delta\lambda$ [nm] | 40 | 18 |
| forward current [mA] | 1000 | 1000 |

Table 3.1.: Main LED parameters from the data sheet

### 3.2.1. Ulbricht Sphere

The Ulbricht sphere is a hollow sphere made of the diffuse reflecting material OP.DI.MA. OP.DI.MA has a reflectance higher than 93 % in the wavelength range between 250 nm and 2.5 $\mu$m. Diffuse reflection on a surface means that an incoming light ray is reflected at many different bounding surfaces to different directions. In contrast to a specular reflecting surface with a typical roughness length much smaller than the wave length of the radiation, a diffuse reflecting surface has a roughness length in the order of magnitude of the wavelength. The soft material OP.DI.MA is protected by an aluminium frame.

Inside the Ulbricht sphere the light emitted by the LEDs is reflected diffusly many times, before it leaves the sphere through a small circular hole of diameter $d = 2\,\mathrm{mm}$ (Fig C.1). By this means, the hole in the Ulbricht sphere is very close to be a Lambertian light source. A light source is Lambertian, if the luminance $L$ is constant

$$L = \frac{d^2\Phi(\theta)}{dA_S\; d\Omega_D(\theta,\phi)} = const \tag{3.1}$$

where $\Phi[W]$ is the radiant energy flux, $dA_S$ is an increment of the source's area perpendicular to the detector direction and $\Omega_D$ is the solid angle of the detector. $\theta$ is the angle between the surface normal and the detector direction and $\phi$ is the azimuthal angle. The intensity $I$ of a Lambertian source depends on $\theta$,

$$I(\theta) = \frac{d\Phi(\theta)}{d\Omega} = \frac{d\Phi_0}{d\Omega}\cos\theta \tag{3.2}$$

but as the area increment of the source $dA_S(\theta) = dA_S^0\,\cos\theta$, the luminance L is constant.

Four high power LEDs are included in the Ulbricht sphere, two of each type (Tab.3.1). They will be referred to intuitively as "RED" and "IR" LED corresponding to their wavelengths $\lambda_{RED} = 632\,nm$ and $\lambda_{IR} = 850\,nm$. They are fixed pairwise (one RED, one IR) in $-90°$ and $+90°$ positions from the hole of the Ulbricht sphere to get maximal isotropy (Fig. 3.1). All LEDs are glued to the aluminium frame of the Ulbricht sphere with heat-conductive glue to enable a sufficient heat transfer and thermal stability.

The Ulbricht sphere makes it possible to couple two light sources with different wavelengths, so the light is emitted from exactly the same area and has a Lambertian emission

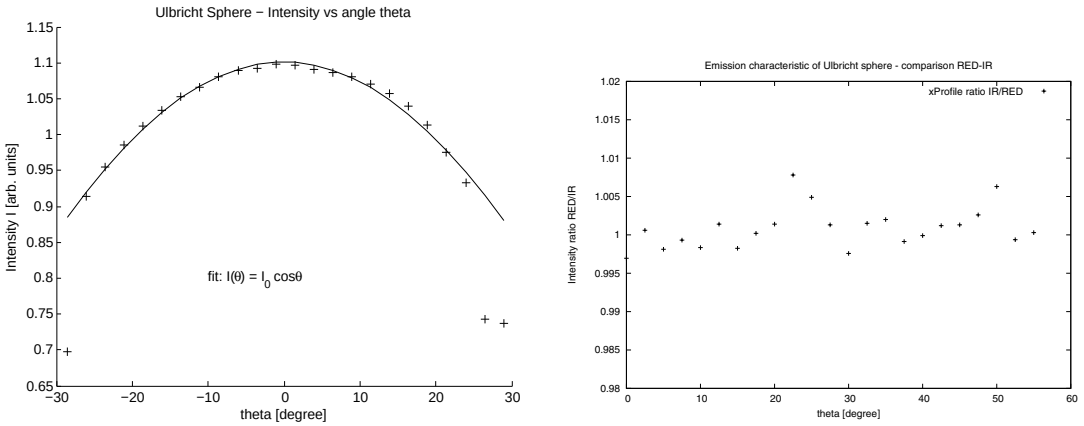


(a) The intensity of the Ulbricht sphere has a $\cos\theta$ angle dependence.

(b) The ratio of the intensities of IR and RED light $I^0_{IR}/I^0_{RED}$ of the Ulbricht sphere is constant.

Figure 3.3.: Directional emission characteristics of the Ulbricht sphere light source

characteristic for both wavelengths.

Fig. 3.3(a) shows the emission characteristic of the Ulbricht sphere with the RED LEDs switched on. The angle dependency was measured for the RED and IR LEDs separately in two directions ($\theta \in [-30°, 30°]$, $\phi = 0°, 90°$), but all with similar results. The luminance $L$ of the Ulbricht sphere light source is integrated over the whole area of the aperture $A_\perp$ perpendicular to the camera direction giving the intensity $I$

$$I(\theta) = \int_{A_\perp} L\, dA = L \int_{A_\perp} dA = L\, A_\perp = L\, A_0\, \cos\theta \tag{3.3}$$

The area of the aperture $A_\perp$ seen by the camera depends on the angle $\theta$. This is due to the fact that for a slant view on the circular aperture it deforms to an ellipse with major semi-axis $a = r$ and minor semi-axis $b = r\, \cos\theta$, so the area is $A_\perp = \pi r^2\, \cos\theta$. The fit in Fig. 3.3(a) shows exactly this dependence of the intensity $I(\theta)$ indicating a constant luminance $L(\theta) = L = const$ for the Ulbricht sphere.

The most important property of the Ulbricht sphere is that the emission characteristics for both the RED and IR light are the same. Later the ratio of both intensities is used to calculate the water height, so no angle dependent corrections have to be done. Fig. 3.3(b) shows the ratio of IR and RED intensities at a wide range of angles $\theta$. The angle $\theta$ has an offset of about 30°, so the intensity ratio is given for a range $\theta \in [-30, 30]$. Both intensities are normalized to their mean value, so the constant factor between both data sets is 1. The variations are smaller than 1 %.

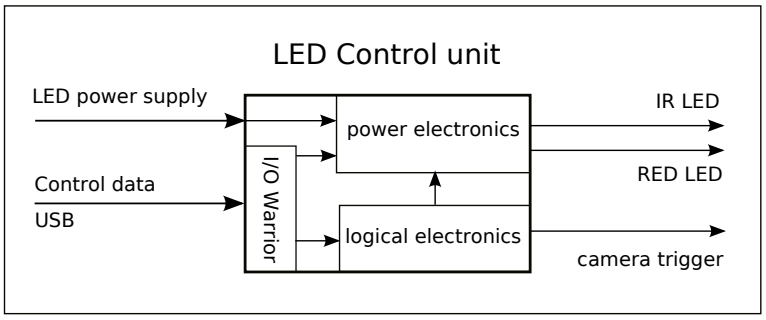


Figure 3.4.: The LED control unit with its basic parts and the input/output signals

### 3.2.2. LED Controller

On order to take two images from the water surface with a IR and RED illumination within a short time, so that the water surface does not change, the IR and RED LEDs in the Ulbricht sphere are pulsed and the camera is triggered. The time pattern and the current for the LEDs in the Ulbricht sphere and the camera trigger signal are controlled by a special control unit (Fig. 3.4). It is connected to the computer via USB and can be programmed with the image processing software heurisko. A special IC chip, the *I/O warrior 24* produced by *Code Mercenaries* in the control unit receives control data from the computer via USB and transfers the data via the serial or parallel ports to the different parts on the board.

In the logical part of the electronics the camera trigger frequency is adjusted and the length and position of the LED flash pulses within the trigger interval are set (Fig. 3.5). For the height measurements two images with RED and IR illumination have to be taken with one camera without a significant change of the water surface's slope. The time $\Delta t_{img}$ between these two images should be much less than the time $\Delta t_{wave}$ a fast wave ($v_{ph} \approx 500\,\mathrm{mm/s}$) needs to run the distance of two pixels projected on the water surface ($\Delta x \approx 0.1\,\mathrm{mm}$), so $\Delta t_{img} \ll \frac{\Delta x}{v_{ph}} \approx 0.2\,\mathrm{ms}$. Due to the fact that the maximal frequency of the camera is around 200 Hz, corresponding to a minimal time of 5 ms between two images, the LEDs have to be flashed. Fig. 3.5 shows that the IR LED flash is set at the end of the exposure time of the first image and the RED LED flash at the beginning of the exposure time of the second image. Hence, the mean temporal distance between both LED pulses is $\Delta t_{img} = 0.08\,\mathrm{ms}$. This is short enough to obtain two images with very small differences. Differences of the magnitude of some pixels can still be seen, because interference of waves of different wavelengths sometimes leads to even faster change of the water surface's slope. To simplify the systematical analysis, the logical part of the LED controller starts the camera trigger always synchronous with the IR LED, so all image sequences start with the IR image.

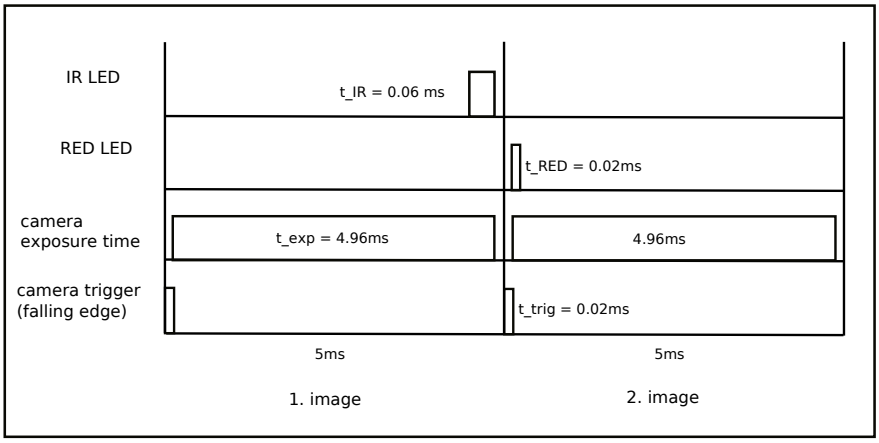


Figure 3.5.: Time pattern of the triggered camera exposure time and the LED pulses

In the power electronics part the current of the LEDs is set. By adjusting the current, the intensity at both wavelengths is set approximately equal. Thus, by varying the aperture of the camera the intensities of light speckles in both images can be set to a high value in the dynamical range of 8 bit $[0, 255]$ of the camera, so the relative noise $\Delta N_{count}/N_{count}$ is about 1 % (Fig. 3.8). Another possibility to balance the IR and RED light speckle intensity in the images is to vary the flash time of the LEDs. Since the spectral sensitivity of the camera is about three times higher for light at $\lambda = 632\,\text{nm}$ than for $\lambda = 850\,\text{nm}$ (Fig. 3.7), the IR flash time is three times longer than the RED flash time (Fig. 3.5).

### 3.2.3. Thermal Stability of LEDs

After the LEDs are switched on they heat up from ambient temperature to a much higher temperature, until the total heat flux produced by the LEDs is equal to the flux flowing away to cooler parts of the aluminium frame of the Ulbricht sphere. The higher temperature leads to a loss of light intensity emitted by the LEDs. Fig. 3.6(a) shows the stabilization of the LEDs' intensity about 15 min after being switched on. After 60 min the intensity of both IR and RED is totally constant in the range of the measurement errors (Fig.3.6(b)). The intensity was measured integrating the light source's intensity over a series of 200 images. Further measurements were always started after the warming up time for the LEDs of about 30 min.

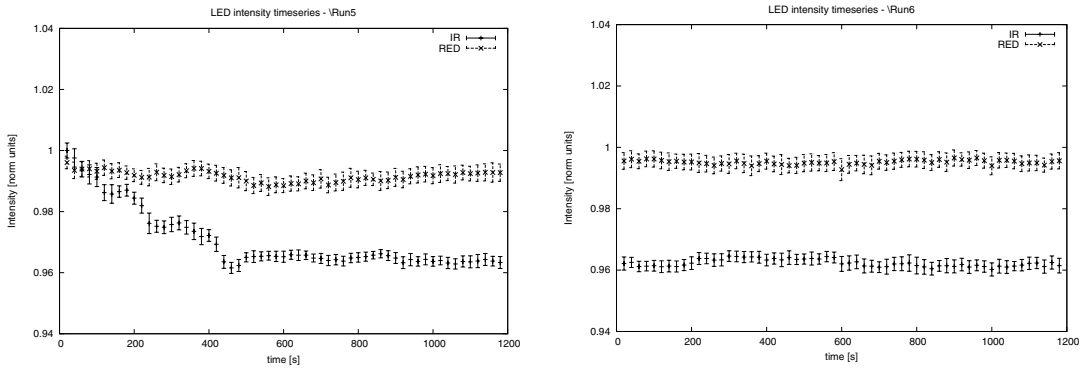


(a) LED intensity immediately after switch-on

(b) LED intensity 1h after switch-on

Figure 3.6.: LED intensity time dependence due to warming up

## 3.3. Camera

The camera *Pike F-032B* produced by *Allied Vision Technologies (AVT)* is a black/white camera with a maximal resolution of $640 \times 480$ pixels. The CCD chip has a pixel size of $7.4\,\mu\text{m} \times 7.4\,\mu\text{m}$. Image data is transfered via FireWire 800 (or IEEE 1394b), a serial bus interface standard developed by Apple Computer. In one cycle of $125\,\mu\text{s}$ a data load of 8192 bytes can be transfered, which is a bandwidth of 800 Mbit/s. Byte depth of the b/w images is 8 bit/pixel corresponding to gray values $[0, 255]$, so the frame rate with a resolution of $640 \times 480$ pixels is limited to 213 fps (frames per second). The camera is triggered with 200 fps by the LED control unit (Fig. 3.4), so images are taken synchronously with the LED flashs (Fig. 3.5).

The object lens is a *RODENSTOCK MEVIS 5018* measurement objective with a focal length of $f = 50\,\text{mm}$. The optics is corrected for wavelengths between 400 nm and 900 nm, so the light speckles on the water surface can be focused for both used wavelengths 632 nm and 850 nm.

Fig. 3.7 shows the spectral sensitivity of the camera. The quantum efficiency is the fraction of photons that generate a electron-hole pair on the chip and are therefore counted. Especially in the near infrared region at 850 nm the sensitivity of the camera is quite low, but for this setup the camera looks directly into the light source, so the signal is very strong and no problems concerning background noise occur.

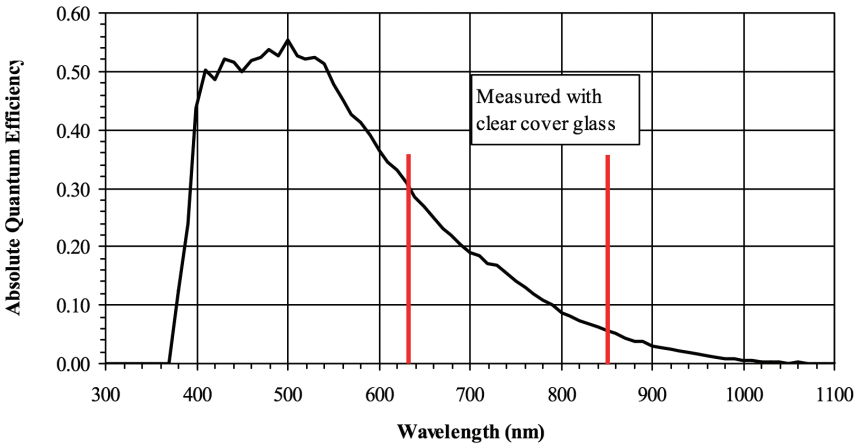


Figure 3.7.: Spectral sensitivity of the camera Pike F-032B from the data sheet. The LED peak wavelengths of $\lambda_{RED} = 632\,\text{nm}$ and $\lambda_{IR} = 850\,\text{nm}$ are marked.

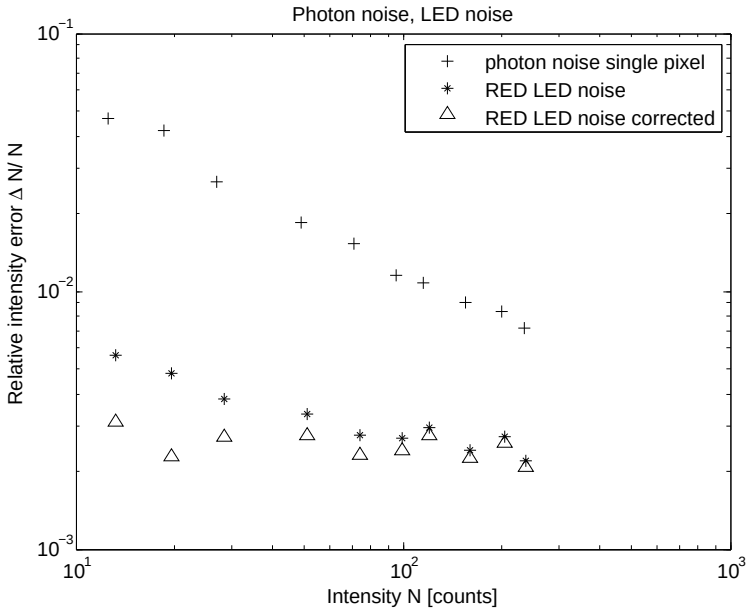


Figure 3.8.: Statistical photon noise and LED intensity noise over the dynamical range [0,255] of the camera.

### 3.3.1. Noise

The photon noise and the variations of the LED flash intensity in time are measured for error calculations of the height measurement. Photon noise $\Delta N_{ph}$ is due to the statistical process of counting the photons that hit one pixel at a certain constant LED intensity during a certain time. The intensity of the LED flashs is expected to vary in time. Both errors affect the measurement of the light speckle's intensity in the image. 1000 images are taken and the mean and variance of the intensities are calculated. The errors are independent, so their squares can be added to the total error (Eq. (3.4)). The intensity is indicated as counts $N$ in the 8 bit image. $n$ is the number of pixels whose counts are added up.

$$\left(\frac{\Delta N_{tot}}{N}\right)^2 = \left(\frac{\Delta N_{LED}}{N}\right)^2 + \left(\frac{1}{\sqrt{n}}\frac{\Delta N_{ph}}{N}\right)^2 \tag{3.4}$$

In oder to determine the two errors, we consider two cases, where the number of analyzed pixels is $n = 1$ and $n = 100$.

For $n = 1$ the error of the counts of only one pixel is determined. In this case the first term in Eq. (3.4) is much smaller than the second, so the total noise $\Delta N_{tot}$ is approximately the photon noise $\Delta N_{ph}$ (Eq. (3.5)). The relative photon noise of a single pixel is shown in Fig. 3.8 (+) and is less than 1 % for count values $N > 100$. Since the photon noise depends on $N$ as $\Delta N_{ph} \propto \sqrt{N}$, the relative photon noise is proportional to the reciprocal of the square root of N, $\frac{\Delta N_{ph}}{N} \propto \frac{1}{\sqrt{N}}$. It appears in the logarithmic plot as a straight with gradient $-\frac{1}{2}$ (Fig. 3.8).

$$\left(\frac{\Delta N_{tot}}{N}\right)^2 \approx \left(\frac{\Delta N_{ph}}{N}\right)^2 \tag{3.5}$$

For $n = 100$ the error of the counts of 100 pixels is determined which show the light source. In Eq. (3.4) the photon noise (second term) is suppressed by the factor 1/100, so the total measured noise $\Delta N_{tot}$ is approximately the LED noise $\Delta N_{LED}$ (Eq. (3.6)).

$$\left(\frac{\Delta N_{tot}}{N}\right)^2 \approx \left(\frac{\Delta N_{LED}}{N}\right)^2 \tag{3.6}$$

Fig. 3.8 shows, that the LED noise ($*$) depends still slightly on $N$, which indicates that the photon noise term is still relevant in this case. It is subtracted to get a constant LED noise of about 0.3 % ($\triangle$). This LED noise is smaller than the photon noise of one single pixel and justifies the neglect of the LED noise in Eq. (3.5).

The smallest light speckles occur for high wind speed, when the water surface has a high local curvature. Even in this case the mean light speckle size is 200 pixels. Additionally,

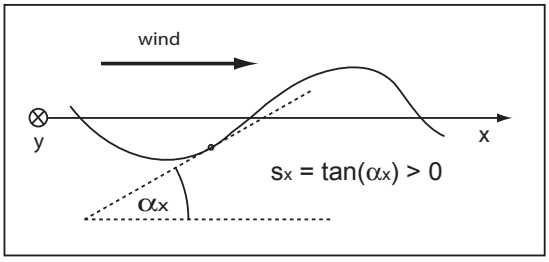


Figure 3.9.: Definition of the coordinate system on the water surface and the x-component of slope $s_x$.

light speckles with a size smaller than 50 pixels are excluded from the wave height analysis. Therefore, for the average light speckle the photon noise is suppressed with a factor $1/\sqrt{200}$, so the intensity error is dominated by the LED noise.

## 3.4. Measurement Principles

The purpose of the measurement is the determination of the probability distribution of the wave slope and height. In the following part the quantities are defined and the measurement principles to determine these quantities are described.

### 3.4.1. Wave Slope

The moving water surface can be represented as a 2-dim function $\eta(x, y, t)$ with the coordinate system $(x, y)$ in the plane of the calm water surface. The x-axis is parallel and the y-axis perpendicular to the wind direction (Fig. 3.9). The slope $\mathbf{s}(x, y, t)$ of the surface is then defined as the gradient of $\eta(x, y, t)$ and the total slope $s$ as the norm of $\mathbf{s}(x, y, t)$. The slope is positive for increasing and negative for a decreasing water surface in wind direction (Fig. 3.9).

$$\mathbf{s}(x, y, t) = \nabla\eta(x, y, t) = \begin{pmatrix} \tan\alpha_x(x, y, t) \\ \tan\alpha_y(x, y, t) \end{pmatrix} \tag{3.7}$$

$$s = |\mathbf{s}| = \sqrt{s_x^2 + s_y^2} \tag{3.8}$$

#### Refraction - Snell's Law

The optical effect of refraction of light at an interface between two materials with different refractive indices is used to measure the slope of the water surface. The refraction is described by Snell's law. The vectorial notation of Snell's law gives the

unit vector for the direction of the outgoing ray $\mathbf{r}'$ given the unit vector in direction of the incoming ray $\mathbf{r}$, the normal unit vector on the interface area $\mathbf{N}$ and the two refractive indices $n$ and $n'$ [3].

$$\mathbf{r}' = \frac{n}{n'}\mathbf{r} + \mathbf{N}\left[\frac{n}{n'}\mathbf{r}\mathbf{N} - \sqrt{1 - \left(\frac{n}{n'}\right)^2 + \left(\frac{n}{n'}\mathbf{r}\mathbf{N}\right)^2}\right] \tag{3.9}$$

In this case of the USSG, the setup has a rotational symmetry around the optical axis, which is perpendicular to the water surface, so the geometry is 2-dim (Fig. 3.1). Most graphs for quantities depending on slope or the position on the water surface in this work are drawn in 2-dim for reasons of clearness, but have to be seen as 3-dim graphs in the context of rotational symmetry (e.g. Fig. 3.11(b)). Due to this symmetry all light ray vectors lie in the plane defined by the optical axis and the point of intersection of the light ray with the water surface. Snell's law becomes the simple relation

$$\frac{sin(\alpha_1)}{sin(\alpha_2)} = \frac{n_2}{n_1} \tag{3.10}$$

with refractive indices $n_1, n_2$ and angles to the interface normal $\alpha_1, \alpha_2$ in material 1 and 2. With the notation of Fig. 3.10(a) Snell's law becomes

$$\frac{sin(atan(s) - \theta_2)}{sin(atan(s) + \theta_3)} = \frac{n_2}{n_1} \tag{3.11}$$

So the necessary condition for the slope on the water surface at a distance of $R_2$ from the optical axis can be calculated that a light ray from the Ulbricht sphere is refracted into the camera.

$$s = \frac{-n_w sin\theta_2 - sin\theta_3}{cos\theta_3 - n_w cos\theta_2} \tag{3.12}$$

The refractive index of water is $n_1 = n_w$ and refractive index of air $n_2 = 1$ in Eq. (3.12). The total slope $s$ can be split in a $s_x$ and $s_y$ component. $(x, y)$ are the world coordinates of the point of intersection of the light ray and the water surface and $R_2$ is the distance of that point from the optical axis, $R_2 = \sqrt{x^2 + y^2}$.

$$s_x = \frac{x}{R_2}s \tag{3.13}$$

$$s_y = \frac{y}{R_2}s \tag{3.14}$$

Angles $\theta_2$ and $\theta_3$ can be determined with knowledge of the whole geometry of the light path from the Ulbricht sphere's hole to the camera aperture. $\theta_2$ cannot be written as an explicit function $\theta_2 = \theta_2(d_1, d_2, d_g, R_2)$, but can be solved by an iteration, that

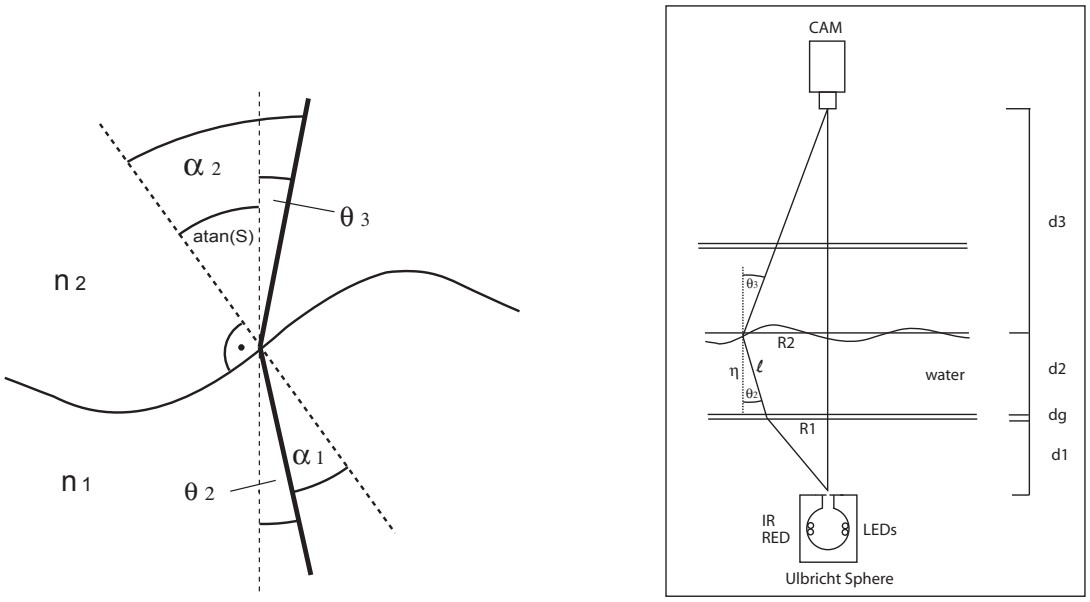


(a) Refraction at the water surface with slope S: Definition of the angles

(b) Setup geometry: Definition of the distances

Figure 3.10.: Definition of geometrical quantities

converges fast.

$$\theta_2 = atan\left(\frac{R_2}{d_2} - \frac{d_g}{d_2}\, tan\left[asin\left(\frac{n_w}{n_g}\sin\theta_2\right)\right] - \frac{d_1}{d_2}\, tan\left[asin(n_w \sin\theta_2)\right]\right) \tag{3.15}$$

$$\theta_3 = atan\left(\frac{R_2}{d_3}\right) \tag{3.16}$$

Fig. 3.10(b) shows the geometry of the light path with the distances $d_1$, $d_2$, $d_3$, $d_g$ and $R_2$. The distance $d_1$ between the light source and the bottom of the flume and the thickness of the bottom window $d_g$ are constant, as well as the distance from the light source to the camera. For the light path the displacement of the light ray due to the glass plate at the bottom of the channel is taken into account, whereas the displacement due to the top glass plate is neglected. This is justified by the fact that the angle $\theta_3$ is small, $\theta_3 < 3°$, so the displacement at the top window is very small. Initially the lengths $d_2$ and $d_3$ are taken as constants, but the effects of variations $d_2$ and $d_3$ due to changing water height for a wavy surface is discussed later (4.1.4). The distance of the light point from the optical axis $R_2$ is measured in the image.

In Fig. 3.11 the slope dependence on the position on the water surface $R_2$ is shown for a realistic geometry of the slope gauge (Eq. (3.12)). The function $s(R_2)$ is nearly linear,

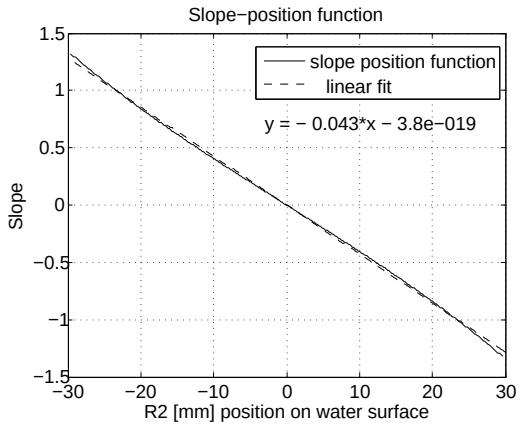


(a) Slope condition at the position $R_2$ to refract a light ray from the light source into the camera

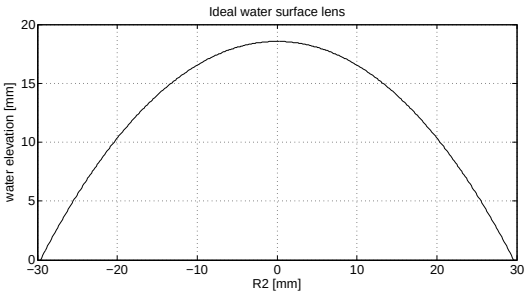


(b) Ideal water lens. Shape of the water surface that would be necessary to form a lens, that refracts all light rays from the light source into the camera (integration of Fig. 3.11(a))

Figure 3.11.: a) Slope condition b) Water lens

so basic considerations for an error estimation can be done with a linear dependence, i.e. 0.042 slope/mm. A light ray from the light source is only refracted into the camera at a position $R_2'$ on the water surface, if and only if the slope at this position $s' = s(R_2')$ according to Fig. 3.11. This is referred to as the refraction condition. A view on Fig. 3.10(b) shows that a convex lens would be needed at the water surface to refract all divergent light rays from the Ulbricht sphere into the camera. This lens with the right slope at all positions is shown in Fig. 3.11, it is the integration of the function $s(R_2)$.

**Dependence of Refractive Index on Wavelength** The refractive index of water differs slightly for both wavelengths: $n(\lambda = 632\,\text{nm}) = 1.332$ and $n(\lambda = 850\,\text{nm}) = 1.329$ [16]. There is no effect on the slope measurements, because only RED images are used for the slope calculation. For the height measurement pairs of RED and IR images are used. The difference in refractive index leads to a small shift of the light speckles in the image of about $0.16mm$ at a slope of $S = 1$, which corresponds to $1\frac{1}{2}$ pixel. This is of the same size as shifts due to the change of the water surface's slope during the time between the IR and RED LED flashs (cp. 3.2.2).

| peak wavelength $\lambda$ [nm] | $\alpha(\lambda)$ [1/mm] | $\frac{1}{\alpha(\lambda)}$ [mm] | $e^{-\alpha(\lambda)l}, \quad l = 100\,\text{mm}$ |
|---|---|---|---|
| 632 | 0.000316 | 3165 | 0.97 |
| 850 | 0.00425 | 235 | 0.65 |

Table 3.2.: Absorption coefficients and absorption factors for the used LEDs. A typical water height in the linear wind wave flume is $l = 100\,\text{mm}$.

### 3.4.2. Wave Height

The amplitude of the water surface $h(x, y, t)$ is defined as the water height from the bottom of the channel $\eta(x, y, t)$ with an evanescent time and space average.

$$h(x, y, t) = \eta(x, y, t) - \langle \eta(x, y, t) \rangle \tag{3.17}$$

$$\langle h \rangle = 0 \tag{3.18}$$

#### Absorption - Lambert-Beer's Law

The water height can be measured comparing the intensities $I_{RED}$ and $I_{IR}$ of light speckles in two images, taken with a RED ($\lambda = 632\,\text{nm}$) and IR ($\lambda = 850\,\text{nm}$) light source [23]. Passing an absorption length $l$ in the water, radiation is absorbed corresponding to the Lambert-Beer law of absorption with $I^0_{IR} = I_{IR}(0)$ and the IR absorption coefficient $\alpha_{IR}$, for RED respectively.

$$I_{IR}(l) = I^0_{IR}\, e^{-\alpha_{IR} l} \tag{3.19}$$

$$I_{RED}(l) = I^0_{RED}\, e^{-\alpha_{RED} l} \tag{3.20}$$

$$l = -\frac{1}{(\alpha_{IR} - \alpha_{RED})} \left[ ln \frac{I^0_{RED}}{I^0_{IR}} + ln \frac{I_{IR}}{I_{RED}} \right] \tag{3.21}$$

Fig. 3.3(b) shows the constant ratio $I^0_{RED}/I^0_{IR}$ of the Ulbricht sphere, so

$$l = -\frac{1}{(\alpha_{IR} - \alpha_{RED})}\, ln \left( \frac{I_{IR}}{I_{RED}} \right) + C \tag{3.22}$$

with a constant length $C$.

$l$ is the slant absorption length in water(Fig. 3.10(b)). The water height $\eta$ is obtained by

$$\eta = l\, \cos\theta_2 \tag{3.23}$$

This is a very small correction. For typical measurements at high wind speed when high slopes occur, the angle $\theta_2$ is small and the cosine is approximately 1, $\langle \theta_2 \rangle = 2.2°$ and $\langle cos\, \theta_2 \rangle = 0.9989$.

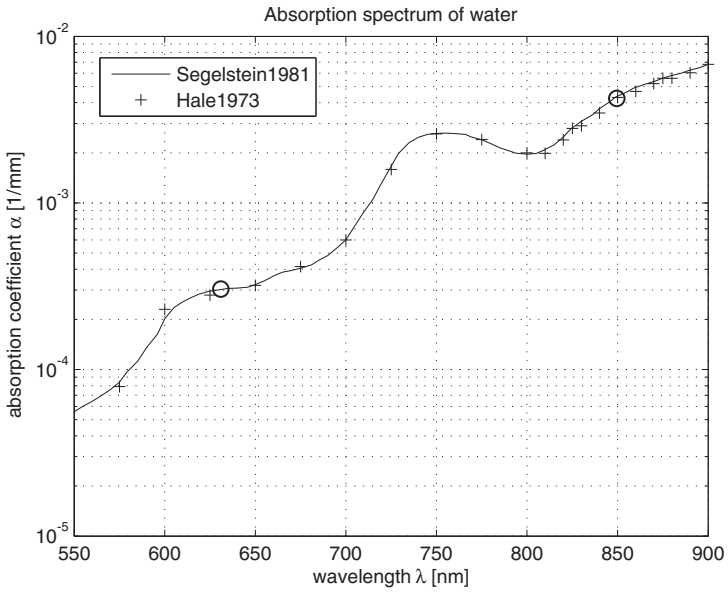


Figure 3.12.: Absorption spectrum of water between 550 nm and 900 nm. The peak wavelength of the LEDs are marked (○). Data from Hale and Querry [16] and Segelstein [42].

**Absorption Coefficients** The LEDs are chosen, so that for the RED wavelength the light passes the water with few absorption (Tab. 3.2). For the IR LED absorption should be as high as possible to gain a good sensitivity for height variations, but without loosing to much intensity in the water column, so images with good contrast can be taken at short flash times.

Fig. 3.12 shows the absorption spectrum of water from literature with marked peak wavelengths of the LEDs. However, the emission spectrum of the LEDs is far away from being monochromatic (Fig. 3.13). This implies that the effective absorption coefficients for the LED radiation differ from the values for the peak wavelengths. The measured intensities to determine the absorption coefficient (Fig. 3.14) are integrated over the LED spectrum.

$$\alpha_{eff} = \frac{1}{l_2 - l_1} ln \left( \frac{I^1_{eff}}{I^2_{eff}} \right) \tag{3.24}$$

$$I^{1/2}_{eff} = \int I_{LED}(\lambda)\, e^{-\alpha(\lambda) l_{1,2}}\, q(\lambda) d\lambda \tag{3.25}$$

So depending on the quantum efficiency of the camera $q(\lambda)$ and the absorption factor $e^{-\alpha(\lambda)l}$ the effective absorption coefficient can be shifted as if the LED had another peak wavelength. It is measured for the IR LED in a water column with absorption length $l \in [0\,\text{nm}, 500\,\text{mm}]$ (Fig. 3.14). The value of $\alpha^{eff}_{IR} = 0.00367\,\text{mm}^{-1}$ is about 86 %

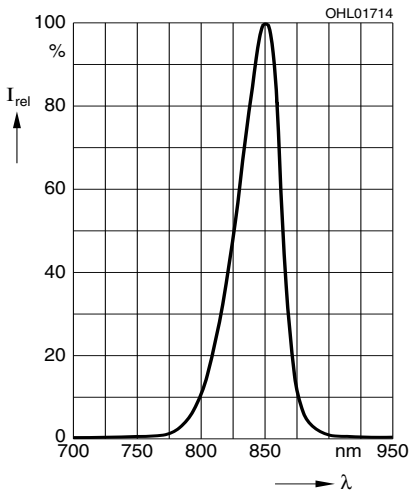


Figure 3.13.: Emission spectrum of the IR LED from the data sheet

of the literature value of the peak wavelength $\lambda_{peak} = 850\,\text{nm}$ and would correspond to an effective peak wavelength $\lambda_{peak}^{eff} \approx 840\,\text{nm}$. This is consistent with the properties of the weighting functions $q(\lambda)$ and $e^{-\alpha(\lambda)l}$, that weight smaller wavelengths stronger in Eq. (3.25).

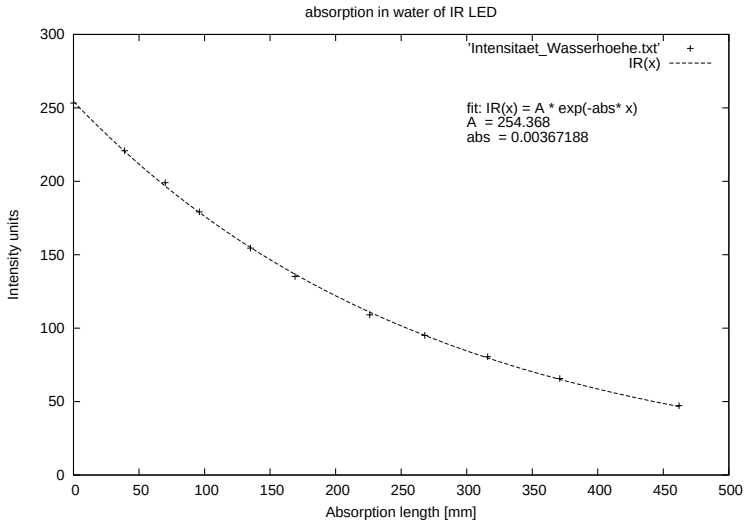


Figure 3.14.: Absorption of IR LED intensity in water. An exponential fit was applied to determine the effective absorption coefficient $\alpha_{IR}$.

(a) IR speckle image (b) RED speckle image (c) Difference image

Figure 3.15.: Typical IR and RED speckle image pair with difference image

### 3.4.3. Light Speckles

For a better demonstration this paragraph shortly describes and shows a pair of images from which slope and height data is extracted. Chap. 5 describes the image processing in detail. Fig. 3.15 shows a typical pair of IR and RED images at a wind velocity $v_{wind} = 5\,\frac{\mathrm{m}}{\mathrm{s}}$. They are taken with a delay of $\Delta t_{img} = 0.08\,\mathrm{ms}$ and show light speckles on the water surface. Light speckles are defined as areas on the water surface that fulfill the slope condition and appear therefore illuminated by the light source, because light rays from the source are refracted into the camera. Shifts of few pixels between the two images can be seen in the difference image. They are caused by slight changes of the slope between both images. Another effect is the different blurring of the speckles due to different refractive indices for the two wavelengths.

### 3.4.4. Statistical Measurements - Homogeneous and Stationary Wave Field

An ISG (Imaging Slope Gauge) takes spacial slope data of the water surface $\mathbf{s}(x, y, t)$, so the water elevation $\eta(x, y, t)$ can be reconstructed in each image. In contrast to this, the much simpler USSG takes images with binary information, i.e. an image shows, if a certain slope $\mathbf{s}$ occurred at a certain point (x,y) on the water surface or not. The height can only be measured, where light speckles occur, i.e. at points where the slopes fulfills the refraction condition. No image of the water surface can be taken, though the statistics of slope and height can be determined. It is described by a probability density function of slope $p_s(s_x, s_y)$ and height $p_h(h)$ (pdf). To be able to measure these pdf's some assumptions have to be made.

1.

$$\frac{\partial p_s(\mathbf{s})}{\partial t} = \frac{\partial p_h(h)}{\partial t} = 0 \tag{3.26}$$

The distributions $p_s(\mathbf{s})$ and $p_h(h)$ are assumed to be constant in time. To determine the distributions, images are taken over a time of several minutes. The distributions are assumed to be constant during that time, when the flow conditions are constant. Hence, reaction times of the air and water flow have to be respected after a change of conditions. Air flow is constant after $t_{wind}^{react} \approx 40\,\mathrm{s}$ [45]. The water flow (in wind direction on the water surface and contrarily at the bottom of the channel) was not measured, but measurements were not started until some minutes after a change of the wind velocity. The wind velocity was always decreased, as deceleration reaction times for the water flow should be shorter than reaction times for acceleration.

2.

$$\left.\frac{\partial p_s(\mathbf{s})}{\partial x}\right|_{field\ of\ view} = \left.\frac{\partial p_s(\mathbf{s})}{\partial y}\right|_{field\ of\ view} = 0 \tag{3.27}$$

$$\left.\frac{\partial p_h(h)}{\partial x}\right|_{field\ of\ view} = \left.\frac{\partial p_h(h)}{\partial y}\right|_{field\ of\ view} = 0 \tag{3.28}$$

The distributions $p_s(\mathbf{s})$ and $p_h(h)$ are assumed to be constant in space at a length scale of the field of view of the camera, because the frequency of occurrence of each slope is measured at a certain point at the water surface and must be representative for all points on the surface. On larger scales the distributions change for a measurement at a different point on the water surface. The distributions are modified for a translation on the water surface in x-direction (upwind) due to the change of wind fetch and in y-direction (crosswind) due to the wave damping and reflecting effects of the channel walls.

### Mean Square Wave Slope

The 2-dim slope probability distribution function $p_s(s_x, s_y)$ is obtained by counting the frequency of occurrence of slope $\mathbf{s}$ in a whole series of about 10000 images. The direct way is to add all images in slope coordinates which leads to a histogram with pixels as bins. Another way is to determine the positions of the light speckles in terms of slope, so the list of measured slopes can be analysed statistically. Both methods are explained and compared in detail in Chap. 5. The variances of the slope in x and y direction $\langle \Delta s_x \rangle^2$ and $\langle \Delta s_y \rangle^2$ are determined from the data.

$$\langle \Delta s_x \rangle^2 = \langle s_x^2 \rangle - \langle s_x \rangle^2 \tag{3.29}$$

Since the spacial and temporal mean of the slope $\langle s_x \rangle$ is zero per definition for a constant water height, the slope variance is equal to the mean square slope

$$\langle s_x \rangle = 0 \tag{3.30}$$

$$\langle \Delta s_x \rangle^2 = \langle s_x^2 \rangle = \sigma_{s_x}^2 \tag{3.31}$$

Therefore, the slope variance $\langle \Delta s_x \rangle^2$ is always referred to in literature as *mean square slope* $\langle s_x^2 \rangle$ with the symbol $\sigma_{s_x}^2$. All equations analogous for $s_y$.

### Root Mean Square Wave Height

The *root mean square wave height* (rms wave height) $\sigma_h$ is determined by a fit of a Gaussian to the distribution of the elevation of the water surface $p_h(h)$, which is calculated from intensity values in corresponding RED and IR images. The rms wave height is defined as

$$\sigma_h^2 = \langle \Delta h \rangle^2 = \langle h^2 \rangle - \langle h \rangle^2 \tag{3.32}$$

$$\langle h \rangle = 0 \tag{3.33}$$

$$\sigma_h = \sqrt{\langle h^2 \rangle} \tag{3.34}$$

# 4. Calibration and Sources of Error

The calibration procedure for both measured quantities, the wave slope and wave height, is described in detail. The validity of the simple geometrical considerations for the determination of the wave slope are verified with calibration devices called slope tubes. The height measurement is calibrated to an ultrasonic distance sensor that measures the water height. After the calibration the dominant errors for single slope and water height values can be estimated.

## 4.1. Slope Calibration

### 4.1.1. Geometrical Calibration

The wave slope is calculated from geometrical relations including Snell's law of refraction. The position on the water surface, where a light ray is refracted, is measured in the images taken by the camera. To be able to measure distances in the images a geometrical calibration is necessary. For this geometrical calibration an *affine* transformation is used. Its parameters are determined by fitting the positions of the edges of a checkerboard calibration target in the calibration image to their real positions (ground truth). A transformation $T$ from pixel coordinates in the image to the world coordinates in the object plane is needed.

$$T : \mathbf{x}_{pix} \longmapsto \mathbf{x}_{world} \tag{4.1}$$

In the simplest case of an ideal pinhole camera this transformation is a scalar multiplication with the magnification factor $V$.

$$\begin{aligned} T(\mathbf{x}_{pix}) &= V\,\mathbf{x}_{world} \\ V &\in \mathbf{R} \end{aligned} \tag{4.2}$$

Both planes have to be parallel and their origins are both at the point of intersection with the optical axis, so a translation is not included.

For the slope gauge an *affine* transformation is used to transform from pixel to world coordinates (Eq. (4.3)). It includes the following transformations: translation, rotation,

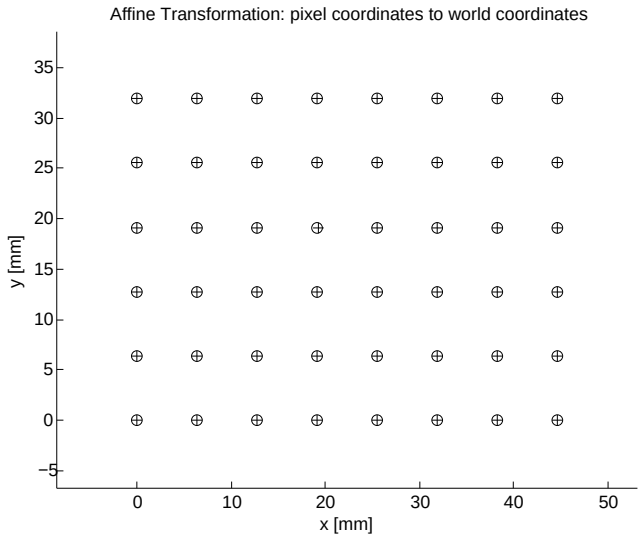


Figure 4.1.: Fit result of the affine transformation from pixel coordinates to world coordinates. Base points (ground truth, ∘) and transformed control points (+)

dilation, compression and shear. It is a linear transformation and in homogenous coordinates, where the z-component is always 1, it can be written as a simple matrix multiplication [18], with the translation coefficients $t_x$ and $t_y$.

$$\begin{bmatrix} x_{world} \\ y_{world} \\ 1 \end{bmatrix} = \begin{bmatrix} a_{11} & a_{12} & t_x \\ a_{21} & a_{22} & t_y \\ 0 & 0 & 1 \end{bmatrix} \begin{bmatrix} x_{pix} \\ y_{pix} \\ 1 \end{bmatrix} \tag{4.3}$$

$$\mathbf{x}_{world} = \mathbf{T}\,\mathbf{x}_{pix} \tag{4.4}$$

Especially for optics with short focal lengths the image-world transformation cannot be represented by a linear transformation. Additionally, distortions of the image in higher orders have to be corrected. But for the used setup with a focal length of $f = 50\,\text{mm}$ an affine transformation is sufficient.

The entries of the transformation matrix are found by a MATLAB fitting routine. It fits the affine transformation, so control points $CP$ ($CP \in \mathbf{x}_{pix}$) extracted from a calibration image are optimal transformed to the base points (ground truth, $\mathbf{x}_{world}$) defined by the calibration target. Fig. 4.1 shows the matching between the base points (∘) and the transformed control points (+). The maximal difference is 0.06 mm, which is half the size of a pixel projected on the water surface. Thus, the transformation can be determined very accurately and length measurements are limited by the pixel size.

In a second step a translation $(t_x, t_y)$ is added to the affine transformation $T$, so that the center of the image is transformed to the origin of the world coordinates (Zero

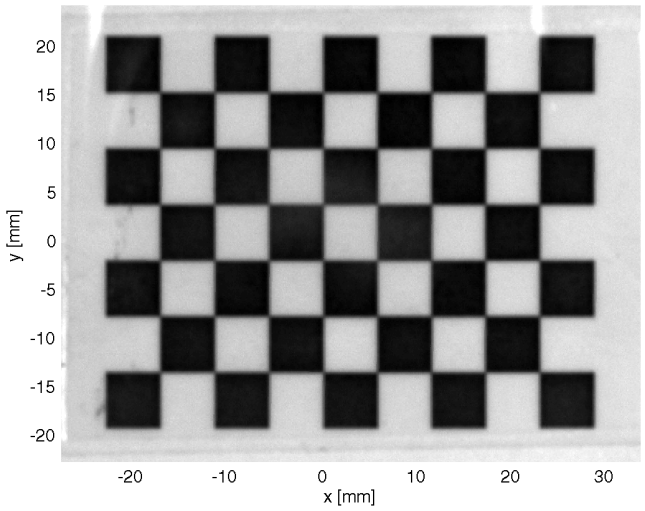


Figure 4.2.: An image of the checkerboard calibration target mapped to world coordinates on the water surface.

Point Correction). That is, the light source centered in the image has the position $\mathbf{x}_{world} = (0, 0)$. Given the affine transformation $T$, all pixel coordinates in the image can be transformed to the position on the water surface (Fig. 4.2).

### 4.1.2. Transformation World Coordinates - Slope Coordinates

With Eq. (3.12) all positions in an image in world coordinates can be transformed to slope coordinates. A light signal on a pixel with slope coordinates $\mathbf{s} = (s_x, s_y)$ is interpreted as the occurrence of that slope on the water surface.

#### Slope Band

The slope mapped to a pixel is only unique for the ideal case of a point-shaped light source. Although the hole in the Ulbricht sphere has a small radius of $r = 1\,\text{mm}$ it has to be considered as extended. Therefore a light signal on a pixel corresponds to different slopes if the light ray was emitted from the center or fringe of the light source. The condition for an illumination of a pixel with world coordinates (x,y) is

$$s_x^{water}(x, y) = s_x^0(x, y) \pm \Delta s_x \tag{4.5}$$

$$s_y^{water}(x, y) = s_y^0(x, y) \pm \Delta s_y \tag{4.6}$$

where $s_x^0(x, y)$ is the strict slope condition (cp. Fig. 3.11). Hence, there can be a slope variation in the range of $2\Delta s$ in one pixel. The value for $\Delta s$ depends on the diameter of the light source. Thus, the function $s_x(x)$ appears as a narrow band in Fig. 4.3. This

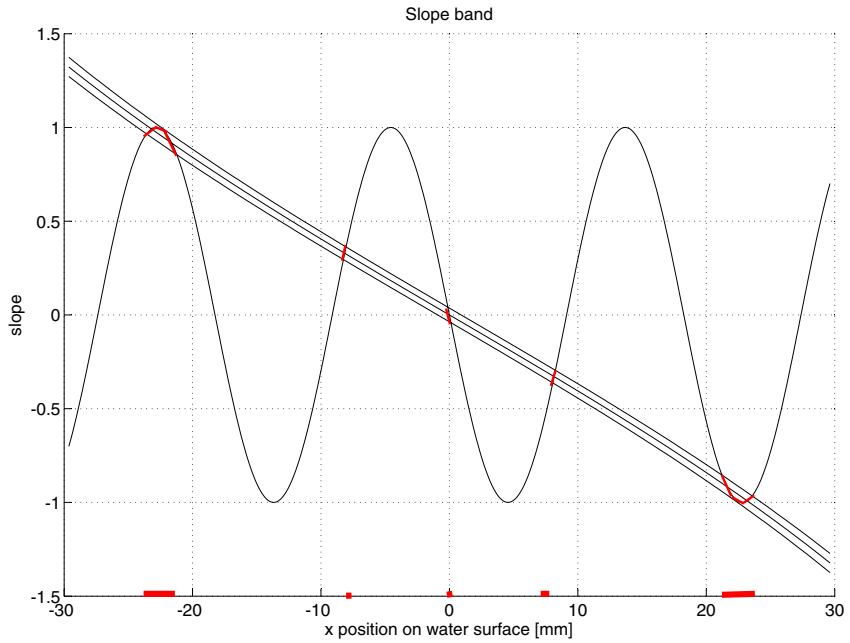


Figure 4.3.: Slope band: slopes at a point x on the water surface that are inside the range of the slope band result in an illumination of the corresponding pixel (red markers). As an example the slope function of a sinusoidal wave is drawn.

band is referred to as *slope band* as a direct translation of the German *Neigungsband* [29]. If the slope at a position $x$ is inside the band, the corresponding pixel is illuminated and shows the occurrence of that slope. The drawn slope of an even sinusoidal wave would result in three small light speckles at lower slopes and two wider light speckles at higher slopes. Both the regions where the slope condition is fulfilled and their projection on the water surface are marked in Fig. 4.3. The diagram also demonstrates how the curvature of a wave (derivative of slope) influences the size of the speckles. The steeper the slope curve is, the smaller is the horizontal projection of its intersection with the slope band, i.e. the smaller is the light speckle.

The slope band in Fig. 4.3 comes from a simple ray tracing simulation in MATLAB. It has a width of $\Delta s \approx 0.05$. This is consistent with the extension of the light source in an image taken at a flat water surface and mapped to slope coordinates (Fig. 4.4).

### Slope Tubes

Due to the fact that the slope measurement principles of the wave gauge are based on a length measurement with the camera and Snell's simple law of refraction, no classical calibration procedure is necessary. This would be the systematic variation of the water

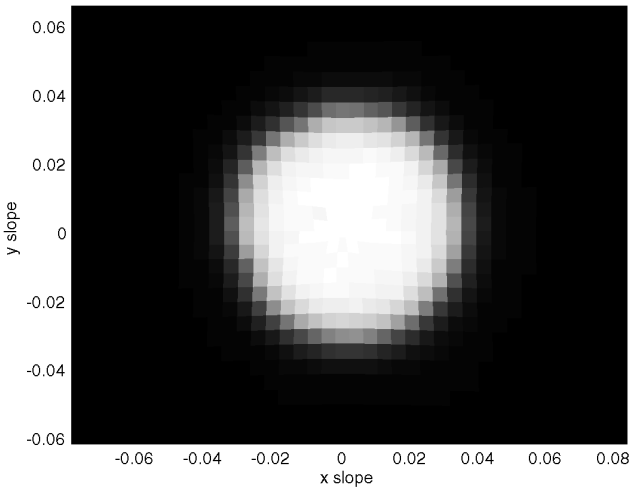


Figure 4.4.: Width of the slope band: due to the extension of the light source pixels with $s \leq 0.05$ are illuminated at a flat water surface, although $s = 0$.

surface's slope and a direct mapping of the slope to pixel positions in the image at a setup with fixed geometry. Instead, the world to slope transformation $s(R_2)$ can be modeled based on Snell's law and trigonometry. To be sure that all effects are respected by this simple model, the results of the model have to be compared to ground truth values. For this reason the measured slope was verified with the help of so-called *slope tubes* (Fig. 4.5(a)). Two plastic tubes were covered with thin Plexiglas windows at a defined slope of $s_1 = 0.993 \pm 0.003$ and $s_2 = 0.591 \pm 0.002$, which correspond to angles $\alpha_1 = 44.8°$ and $\alpha_2 = 30.6°$, and filled with water. The slope tubes were set at various points in the field of view of the camera (Fig. 4.5(b)). The measured slope from light speckle positions in the image match very well the ground truth slope of the slope tubes. Measured slope values are $s_1^{meas} = 0.980 \pm 0.012$ and $s_2^{meas} = 0.594 \pm 0.003$. Within the error margins this is consistent with the ground truth slope of the slope tubes. Hence, the slope measurement based on length measurement with the camera is reliable.

The model's predictions of the variation in measured slope due to changes in water height are verified with the slope tubes and confirm the validity of the simple calculations.

### 4.1.3. Calibration Procedure in the Linear Flume

#### Camera - Light Source Adjustment

All previous argumentations rely on the fact that the optical axis of the camera is perpendicular to the flat water surface and that the hole of the Ulbricht sphere is on

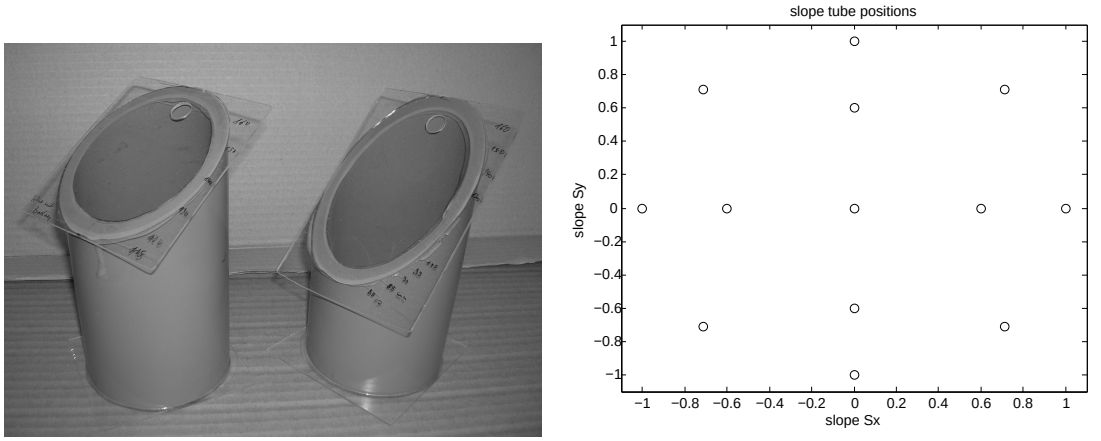


(a) Slope tubes with $s_1 \approx 1$ (right) and $s_2 \approx 0.6$ (left)

(b) Positions in slope space verified with ground truth slope tube data.

Figure 4.5.: Calibration with slope tubes

the optical axis (Fig. 3.10(b)). Therefore it has to be adjusted carefully.

First, the optical axis of the camera is set perpendicular to the water surface. In the mirror image of the camera reflected at the water surface the camera sees its own objective lens, whose center point is marked with a white point. A modified lens cap is used for that purpose. With the assumption that the center point of the CCD chip lies on the optical axis of the camera's objective, the camera can simply be adjusted such that the bright point at the center of the objective is located at the center point of the CCD chip, i.e. of the image. The incident light ray from the objective's center to the water surface and the reflected ray to the center pixel of the chip are parallel, so they are at right angle with the water surface. Several mirror images occur due to the glass windows of the flume, but the mirror image on the water surface can easily be identified, because it moves most for a slightly moving water surface.

Second, the light source under the flume is adjusted that it appears centered in the image of the camera, so it is located on the optical axis.

### Geometrical Calibration with a Checkerboard Target

For gas exchange measurements even with highly reactive gases, e.g. hydrochloric acid fumes $HCl$, the linear wind wave flume is airtight. For this reason the top cover is fixed with a hundred screws and a Teflon seal, so there is no simple acces to the water surface, where a calibration target should be positioned to calibrate the length measurement.

To simplify the calibration process a calibration target for the geometrical calibration

is fixed under the wind wave flume. With the assumption of a pinhole camera model (Fig. B.3) the geometrical calibration is rescaled with respect to the distance between the calibration target and the water surface. A checkerboard with square length $sl = 6.38\,\text{mm}$ is clamped against the bottom window of the flume, so the checkerboard plane is perpendicular to the optical axis of the camera. The rotational orientation around the optical axis is chosen that the edges of the checkerboard are parallel to the image edges. Hence, the orientation of the checkerboard is given by the camera's orientation in relation to the flume. The camera is adjusted in a way that the edges of the images are parallel to the wind direction given by the walls of the flume.

Calibration images are taken with the camera focused on the standard water surface height in the channel. This is necessary, because the focus changes the scale factor of the camera's optics. Since the water level is approximately 10 cm above the checkerboard plane, the calibration images (with the checkerboard under the bottom of the flume) are blurred. However, in the calibration procedure the corners of the checkerboard are detected by an algorithm (Camera Calibration Toolbox for MATLAB [6]), which is based on an edge filter in two directions that works on blurred images.

The fit of the affine transformation to the base points (ground truth) of the checkerboard gives the transformation matrix $T$. It is corrected to the right distance from the camera to the water surface and the origin is centered (Zero Point Correction (4.1.1)).

$$T = \begin{bmatrix} -0.1103 & 0.0000 & 0 \\ -0.0002 & -0.1109 & 0 \\ 35.4943 & 26.7097 & 1.0000 \end{bmatrix} \tag{4.7}$$

$$M = \begin{bmatrix} -0.1103 & 0.0000 \\ -0.0002 & -0.1109 \end{bmatrix} \tag{4.8}$$

$$V = \sqrt{det(M)} = 0.1106 \tag{4.9}$$

Entries $M(1,2) = M(2,1) \approx 0$ and $M(1,1) = M(2,2)$ show that the transformation is only a dilation. No rotation is included in $T$, because the calibration checkerboard is oriented to the edges of the calibration image. V is the magnification factor with unit [mm/pixel]. With this value, the field of view on the water surface is $640 \times 480\,pixel^2 \times V^2 = 71 \times 53\,\text{mm}^2$. Thus, the field of view is small compared to the dimensions of the water surface ($3000 \times 300\,\text{mm}^2$), so the condition of a locally stationary and homogeneous wave field is fulfilled.

The calibration procedure was repeated 10 times to estimate the variation of the geometrical calibration due to different positions of the checkerboard in the calibration image and due to the fitting process. The obtained variation of the magnification factor $V$ is less than 0.1 %.

#### Focusing the Light Speckles

For the slope measurement and especially for the height measurement the images of the light speckles should be pictured as sharp as possible. The camera cannot simply be focused on the light source at a calm water surface, because the wavy water surface has a curvature, so additional lenses at the water surface lead to blurred images of the light speckles. The water surface must be the focus plane, but no target can be put there, as the flume is closed. So the light speckles must be focused at a rough water surface, which means focusing while looking on fast moving images with objects that can also be blurred depending on the curvature of the water surface.

In fact, two limiting cases show the problems of focusing: First, for a very small curvature of the water surface there is no additional lens and the camera can be focused on the light source under the flume. Second, for a high curvature the water surface must be seen as a strong lens and the combined optics of camera and water lens cannot focus on the light source. Hence, the lens, the water surface must be focused.

The unavoidable blurring of the light speckles is the reason why the intensity of the light speckles must be seen as a continuous quantity that is a measure for the frequency of occurrence of a slope. This is especially important for the choice of the analysis method to obtain the slope distribution from the light speckle images (see Section 5.2.1).

### 4.1.4. Slope Error for Single Slope Values

For a slope measurement of $s = 1$ at maximum wind speed (maximum height variation of water surface) the total error of slope is $\Delta s \leq 0.065$. Most important are the errors due to the slope band and due to height variations of the water surface. The constant error of the slope band is $\Delta s_{slopeband} = 0.05$ (cp. 4.1.2). The height variation of the water surface changes the geometry of the slope gauge and leads to an error with a linear dependence on slope $\Delta s_{heightvar}(s) = 4\,\%\, s$. The error due to height variations fo the water surface becomes dominant for conditions where higher gravity waves occur. Additionally, uncertainties of length measurements in the setup play a role for the total error. Tab. 4.1 shows the main slope errors ordered in descending importance. Since they are uncorrelated their squares can be added to the total error.

| slope error due to | type | $\Delta s(s)$ |
|---|---|---|
| width of light source (slope band) | constant | 0.05 |
| water height variations $d_2$ | relative | 0.04 $s$ |
| length measurements $d_1, d_3$ | relative | 0.01 $s$ |
| maximal total error at $s = 1$ | | 0.065 |

Table 4.1.: Main errors of slope mapped to pixels

## 4.2. Height Calibration

### 4.2.1. Photometric Calibration

A photometric calibration is necessary to measure total light intensities with a camera. This is a difficult task, because the camera has to be calibrated with a total intensity standard. Black bodies or special lamps can be used, but the whole procedure is quite sensitive to stray light and depends on angles and wavelengths. By the way, Ulbricht spheres are also used as photometric standard lamps with a Lambertian emission characteristic.

In this case no absolute measurements of intensity is necessary for the height measurement, as only the ratio of RED and IR intensity appears in the equation for the water height (Eq. (3.22)).

However, depending on the method to obtain the slope distribution, corrections for the slope measurement have to be considered, as the RED intensity is a quantity for the frequency of occurrence of the slope. An angle (slope) dependent intensity would bias the slope distribution. The following effects cause the intensity to be slope dependent.

1. Lambertian light source. The intensity $I(\theta_1)$ emitted by the light source is

$$I(\theta_1) = L\ A_\perp = L\ A_0\ cos\ \theta_1 \tag{4.10}$$

   with the constant luminance $L$ and light source area $A_0$. See Fig. 3.3(a) for the measured angle dependency of the intensity of the Ulbricht sphere.

2. Fresnel reflection at interfaces (glass, water, air). The Fresnel equations describe the angle dependent transmission $T$ and reflection $R$ of light at an interface of two media with different refractive indices. Using Snell's law the refractive indices vanish and the reflection coefficient depends only on the angles of the incident $\theta_i$ and transmitted $\theta_t$ light ray. Reflection coefficients are different for linear polarized light perpendicular and parallel to the plane of incidence and can be averaged in

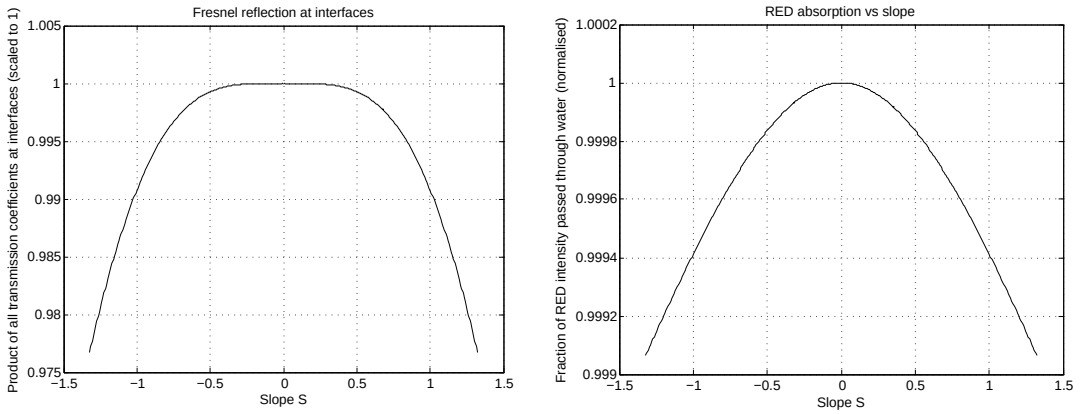


(a) Intensity loss to higher slopes (angles) due to Fresnel reflection at interfaces, simulation

(b) Absorption effect for longer absorption length due to slant rays at higher slopes (angles), simulation

Figure 4.6.: Effects that cause an angle dependent RED intensity: Fresnel reflection and absorption

the case of unpolarized light.

$$R = \frac{1}{2}\left[R_{\perp} + R_{\parallel}\right] \tag{4.11}$$

$$R = \frac{1}{2}\left[\left(\frac{sin(\theta_t - \theta_i)}{sin(\theta_t + \theta_i)}\right)^2 + \left(\frac{tan(\theta_t - \theta_i)}{tan(\theta_t + \theta_i)}\right)^2\right] \tag{4.12}$$

$$T = 1 - R \tag{4.13}$$

Fig. 4.6(a) shows the loss of intensity to higher slopes (angles) due to Fresnel reflection at the interfaces. The data comes from a simulation of the slope gauge's geometry in MATLAB.

3. Absorption effect due to slant ray path in water (RED). The stronger absorption of RED light at higher slopes due to a slant ray path in water and a slightly longer absorption length is less than 0.1 % (simulated data in Fig. 4.6(b)).

The influence of slope dependent effects on the intensity of the RED slope distribution are discussed in 5.2.1.

### 4.2.2. Ultrasonic Height Sensor

The water height in the wind wave flume is measured with an ultrasonic distance sensor for two reasons. First, the water height measured by the USSG can be calibrated

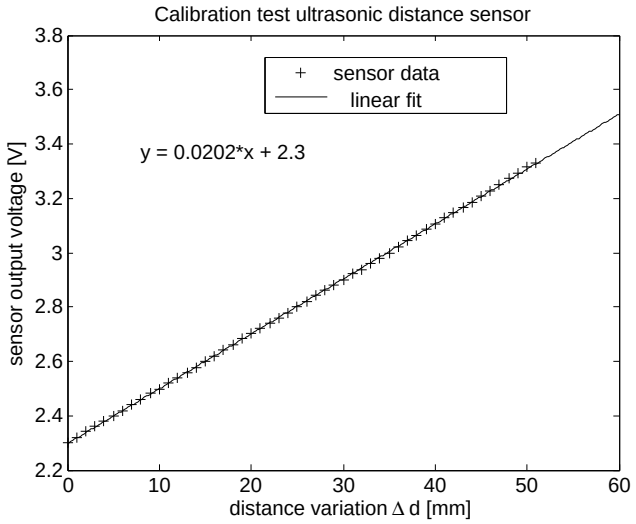


Figure 4.7.: Verification of the calibration of the ultrasonic distance sensor

with the data from a ultrasonic distance sensor. The absorption coefficient of water is determined for both the RED and IR LEDs. Second, the total water height $d_2$ (Fig. 3.10(b)) defines the geometry of the USSG and must be determined for slope measurements.

The ultrasonic distance sensor is a P47-F4V-2D-1C0-300E produced by the German company *PIL Ultraschall Sensorik*. A piezo-electric element emits an ultrasonic pulse and receives the pulse reflected by the water surface. Distance is calculated from the time of flight. The sensor can measure distances between $100\,\text{mm} - 600\,\text{mm}$ with a repeatability of measured distance of $\pm 2\,\text{mm}$ for a single measurement. The repeat rate for the measurement is $100\,\text{Hz}$, so the error of a measurement over $1\,\text{s}$ is much smaller as can be seen in Fig. 4.7. The water surface must be flat, because the sensor needs objects of the size $10 \times 10\,\text{cm}^2$ for an accurate reflection, so it averages over a wide area and would only measure the mean water height for a wavy water surface. Signal output is a voltage $0 - 10\,V$ with a fixed gain of $20\,\text{mV/mm}$. The linearity and the gain factor are checked by a calibration measurement with a water basin on a translation stage. The distance between the sensor and the water surface of the basin is increased in steps of $1\,\text{mm}$. Fig. 4.7 shows the linearity of the sensor with a slightly higher gain of $20.2\,\text{mV/mm}$ than indicated in the data sheet. This is respected for the height measurement. The voltage signal of the sensor is converted to a digital signal by an analog-digital converter and recorded with the image processing software *heurisko*.

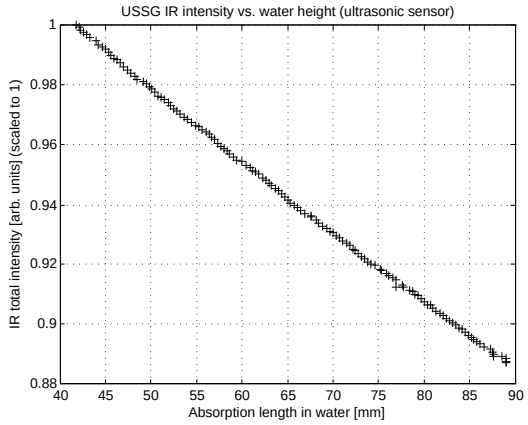


(a) Intensity of IR light speckles vs. water height measured with the ultrasonic sensor

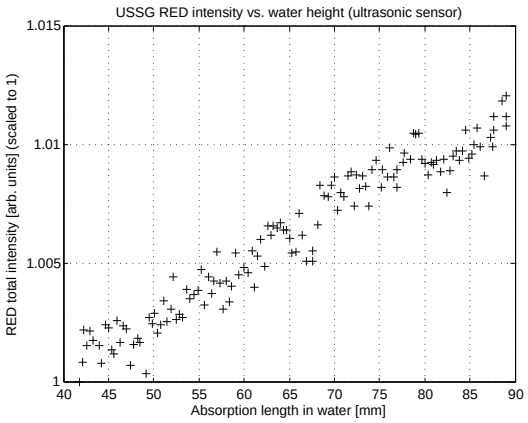


(b) Intensity of RED light speckles vs. water height measured with the ultrasonic sensor. Intensity increases(!) for a increasing absorption length due to an additional focus effect apart from absorption

Figure 4.8.: USSG IR and RED intensities vs. water height

### 4.2.3. Height Calibration in the Flume, Determination of Absorption Coefficients

The water height measured by the USSG is calibrated to the height data of the ultrasonic distance sensor by the determination of the absorption coefficients and a constant height shift. Although the IR absorption coefficient was already determined in a measurement outside of the flume (Fig. 3.14), the measurement was repeated inside the flume for the the determination of the RED and IR absorption coefficient.

The ultrasonic distance sensor is fixed at the top of the flume above the water looking perpendicular to the water surface, to achieve an optimal reflection of the ultrasonic waves at the flat water surface. Distances to the walls are at least 10 cm. During varying the water height, it is measured with the ultrasonic sensor and with the USSG. Intensities for both wavelengths of the Ulbricht sphere light source are taken every 5 s as an average of 50 images taken within 0.5 s. The intensity of a light speckle in one image is determined by summing up the intensities of all pixel of the light speckle.

Fig. 4.8(a) shows the measured intensities depending on the water height measured with the ultrasonic sensor. The IR intensity decreases apparently following Lambert-Beer's law. But surprisingly the RED intensity increases with an increasing absorption length. This indicates an additional optical effect of focusing by the water column $f_{foc}(l)$, so the higher the water is the more intensity of the light source is captured. Since the

geometry is the same for IR and RED images, this effect must also influence the IR intensity, where it is much smaller than the absorption and cannot directly be seen in the data. Only for the RED intensity, where absorption is small, the focus effect overcompensates the absorption, which leads to the surprising fact of higher intensities for a thicker absorption medium. The occurrence of the focus effect makes it impossible to determine both absorption coefficients $\alpha_{IR}$ and $\alpha_{RED}$ by fitting to the intensity data directly. But in the following part it is shown, that a focus effect depending linear on the water height has no effect on the height measurement based on the comparison of IR and RED intensity.

The intensity depends on the water height $l$ with the factor $f_{tot}(l)$ due to Lambert-Beer's law and the unknown focus effect $f_{foc}(l)$.

$$f_{tot}(l) = e^{-\alpha_{abs}\ l} \ \cdot \ f_{foc}(l) \tag{4.14}$$

Fig.4.8(b) indicates, that the additional focus factor $f_{foc}(l)$ depends linear on $l$, as it changes an expected weakly exponential (linear) decline to a linear increase. So the ansatz is

$$f_{foc}(l) = 1 + \alpha_{foc} l \ \approx \ e^{(\alpha_{foc}\ l)} \tag{4.15}$$

The focus effect can be estimated by comparing the expected decline of the RED intensity to the measured increase. A rough calculation over the full measured range $\Delta l \approx 50\,\mathrm{mm}$ with an expected absorption coefficient $\alpha_{RED}^{exp} \approx 0.0003\,\mathrm{mm}^{-1}$ (Fig. 3.12) gives

$$f_{foc}(\Delta l) \ = \ e^{(\alpha_{foc}\Delta l)} = f_{tot}^{meas}(\Delta l)\ e^{(\alpha_{abs}\Delta l)} \approx 1.03 \tag{4.16}$$

$$\alpha_{foc}\Delta l \ \approx \ ln(1.03) \approx 0.03 \tag{4.17}$$

The focus effect increases the RED intensity by about 3 % over the full water height variation of $\Delta l \approx 50\,\mathrm{mm}$. So $\alpha_{foc}\Delta l$ is small which justifies the backward first-order Taylor series approximation in Eq. (4.15). Hence, the total factor $f_{tot}(l)$ can be written

$$f_{tot}(l) \ = \ e^{-(\alpha_{abs}\ l)}\ e^{(\alpha_{foc}\ l)} = e^{-(\alpha_{abs}-\alpha_{foc}\ l)} = e^{-(\alpha_{eff}\ l)} \tag{4.18}$$

$$\alpha_{eff} \ = \ (\alpha_{abs} - \alpha_{foc}) \tag{4.19}$$

Thus, the IR and RED intensity depends on the length $l$ according to Lambert-Beer's law with the effective absorption coefficients $\alpha_{eff}^{IR}$ and $\alpha_{eff}^{IR}$. But Eq. (4.21) shows that the measured absorption length $l$ depends only on the difference of the absorption coefficients $(\alpha_{IR} - \alpha_{RED})$, so the focus effect vanishes for the height measurement.

$$\alpha_{eff}^{IR} - \alpha_{eff}^{RED} \ = \ (\alpha_{abs}^{IR} - \alpha_{foc}^{IR}) - (\alpha_{abs}^{RED} - \alpha_{foc}^{RED}) = \alpha_{abs}^{IR} - \alpha_{abs}^{RED} \tag{4.20}$$

$$l \ = \ -\frac{1}{(\alpha_{IR} - \alpha_{RED})}\ ln\left(\frac{I_{IR}}{I_{RED}}\right) + C \tag{4.21}$$

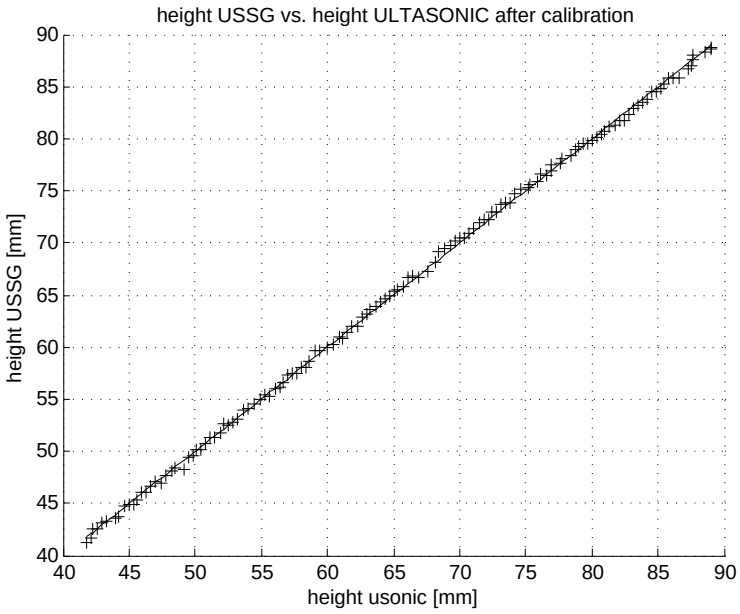


Figure 4.9.: Comparison of the calibrated USSG height data to the ultrasonic height sensor data. The line is a straight with slope 1.

The single absorption coefficients cannot be determined, but their difference ($\alpha_{abs}^{IR} - \alpha_{abs}^{RED}$). Therefore, the USSG data calculated with Eq. (4.21) is fitted to the height data of the ultrasonic sensor via parameters $p_1 = (\alpha_{IR} - \alpha_{RED})$ and $p_2 = C$. The fit result can be seen in Fig. 4.9. The height data of the USSG is consistent with that of the ultrasonic sensor for parameter $p_1 = (\alpha_{IR} - \alpha_{RED}) = 0.002743\,\mathrm{mm}^{-1}$. The standard deviation of the difference of both datasets is $\langle \Delta l \rangle = 0.33\,\mathrm{mm}$. This value must not be misinterpreted as the possible height resolution for a single measurement of the USSG, because the intensities for the calibration are mean values from 50 measurements. The single measurements have a standard deviation of about 1.8 mm, which is a realistic resolution for the height measurement of a flat water surface.

The value $(\alpha_{IR} - \alpha_{RED}) = 0.00274\,\mathrm{mm}^{-1}$ is used for following height measurements. It is consistent with values for $\alpha_{IR}$ and $\alpha_{RED}$ from literature. With $\alpha_{RED} \approx 0.0003\,\mathrm{mm}^{-1}$, $\alpha_{IR}$ would be $0.00304\,\mathrm{mm}^{-1}$. This is smaller than the absorption coefficient for $\lambda = 850\,\mathrm{nm}$, it corresponds to a wavelength $\lambda \approx 830\,\mathrm{nm}$, but this is due to the asymmetric spectrum of the LED and a higher quantum efficiency of the camera for lower wavelengths (cp. 3.4.2).

### 4.2.4. Height Error

A single height measurement on the water surface by comparing the IR and RED intensity of a light speckle in an image pair has errors due to uncertainties of the intensity measurement and due to the error of the difference of absorption coefficients (Eq. (4.21)). The intensity values vary due to the noise of the camera and the noise of the LED intensity. The intensity is also biased by fast changes of the water surface slope and lens effects of a rough surface that lead to a different form of the light speckles in a corresponding IR/RED image pair. Under the assumption, that the errors are independent, their squares can be added to the total error of the intensity

$$\left(\frac{\Delta I}{I}\right)^2 = \left(\frac{\Delta I_{LED}}{I}\right)^2 + \left(\frac{\Delta I_{CAM}}{I}\right)^2 + \left(\frac{\Delta I_{bias}}{I}\right)^2 \tag{4.22}$$

The errors in detail and their size are the following.

1. Light source: LED noise. The flashing of the LEDs causes variations of the emitted intensity of about $\frac{\Delta I_{LED}}{I} = 0.3\,\%$.

2. Camera noise. The photon noise in one pixel depends on the counts $N_{phot}$ in that pixel ($N_{phot} \in [0, 255]$). For a well balanced intensity with counts $N_{phot} > 100$ the relative error $\frac{\Delta N_{phot}}{N_{phot}} \leq 1\,\%$, but can reach $5\,\%$ for low intensities (cp. 3.3.1). This error decreases for an intensity calculated as the mean of $n$ pixels as $\frac{\Delta I_{CAM}}{I} = \frac{1}{\sqrt{n}}\frac{\Delta N_{phot}}{N_{phot}}$. Thus, the intensity error is less than $0.1\,\%$ for a photon noise of $1\,\%$ and a light speckle size of more than $n = 100$ pixels, which is the case for almost all light speckles.

3. Variations of the intensity ratio due to fast changes of the surface's slope and lens effects of the rough water surface (see section 3.4.3). For the majority of image pairs the IR and RED light speckles have the same size and position. But in cases when the slope at a light speckle changes significantly in the time between the two LED pulses $\Delta t_{pulse}$, one of the corresponding speckles can be much larger and brighter than the other. A second possible effect is the different focusing by water lenses with high curvature due to the different refractive index of the IR and RED light, which might cause a bias in the intensities. This leads to false height values which can even exceed the dimensions of the flume in extreme cases, so wave heights of 40 cm are measured for an almost flat water surface. These non-realistic values can be excluded from a further analysis, but there is an influence even on realistic height values, which can only be estimated.

4. Absorption coefficients. A constant value is taken for the difference of the absorption coefficients ($\alpha_{IR} - \alpha_{RED}$) for the calculation of the height data (Eq. (4.21)).

It is determined by the calibration of the USSG to the ultrasonic distance sensor. The uncertainty of this value leads to a systematic error of the height values which is constant for all data in contrast to the first three errors, that are statistical errors of all height values.

5. The correction of the slant absorption length $l$ to the water height $\eta$, $\eta = l \cos\theta_2$ depends on the water height itself, because the angle $\theta_2$ depends on the geometry of the ray path so it does on the water height $\eta$. However, the correction itself is very small so the even smaller error can be neglected.

The final error for the height measurement only due to the first two points can be calculated.

$$\Delta h = \frac{1}{(\alpha_{IR} - \alpha_{RED})} \sqrt{\left(\frac{\Delta I_{RED}}{I_{RED}}\right)^2 + \left(\frac{\Delta I_{IR}}{I_{IR}}\right)^2} \tag{4.23}$$

$$\Delta h \approx 1.6\,\text{mm} \tag{4.24}$$

This value is consistent with the found error for single height measurements at a flat water surface $\Delta h \approx 1.8\,\text{mm}$. Hence, for height measurements in absence of errors from point 3 and 5, the observed height error can be explained by intensity variations due to camera and LED noise.

# 5. Image and Data Processing

The camera is the part of the wave gauge that delivers the data. The image sequences are intensity data from the water surface which are 2-dim in space and 1-dim in time.

$$\text{Image sequence} : I(x, y, t) \tag{5.1}$$

Time plays a minor role for the analysis, since no time dependent quantities are measured. The height and slope distributions are assumed to be constant in time (cp. 3.4.4). The single images can be seen as micro states of the statistical system 'water surface' and the whole image sequence is the statistical ensemble.

Positions in the images are directly connected to the slope via the geometry of the wave gauge. Intensities are measured to determine the water height. To extract positions and intensities of light speckles in the images some operations have to be done on the image data. In the following these operations on the images are described in detail. Different methods are presented to obtain the slope and height distributions and their disadvantages and advantages are discussed. Image processing is done with the software *heurisko*, which offers a diversity of image processing operators and is optimized to operate very fast on large amounts of data. Fig. 5.1 shows the steps from the acquisition of the image sequences to the slope distribution and values for mean square slope and Fig. 5.8 shows the data processing to obtain the root mean square wave height (rms wave height).

## 5.1. Basic Operations

### 5.1.1. Removal of Intensity Background

Since the camera looks directly into the light source very short exposure times $t_{exp} = 4.96\,\text{ms}$ are possible. Hence, the background intensity (or dark image) is mostly zero or only few counts. It can be removed by a simple masking operation. The mask is a binary image which is obtained by a segmentation of the speckle image with a low threshold of 5 counts. Thus, the mask has the value 1 at pixels with an intensity $I > 5$ (the speckles) and the value 0 for the rest. The multiplication of the mask with the

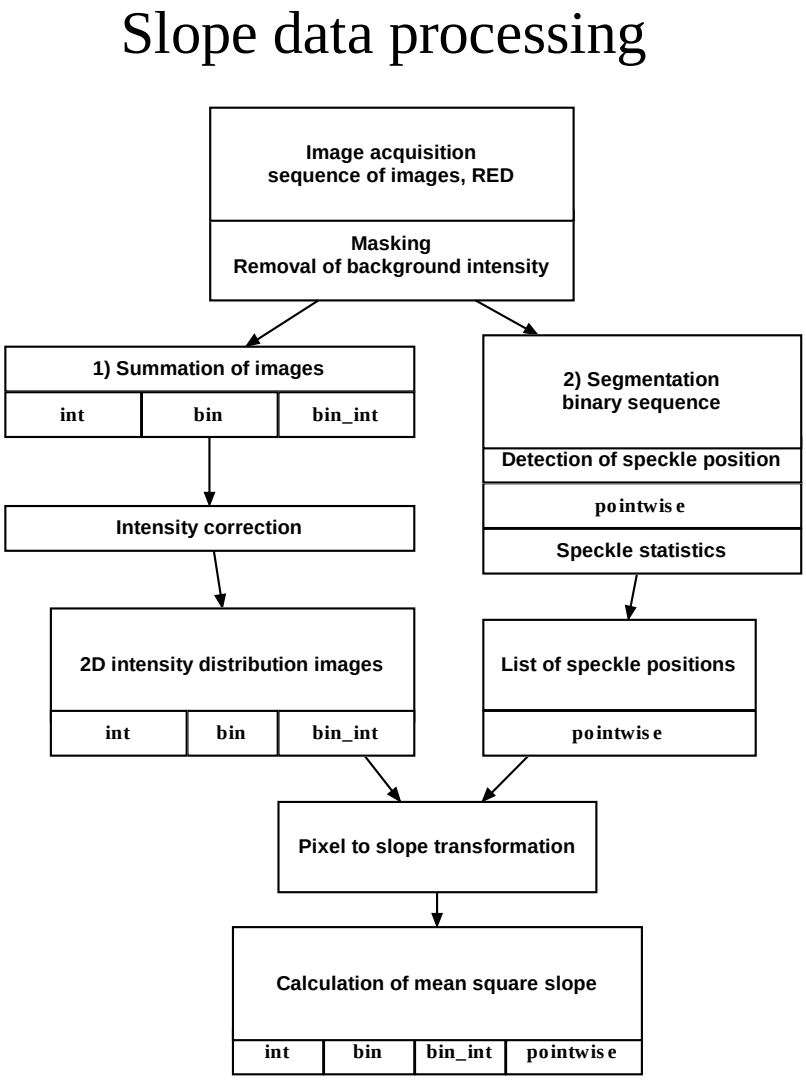


Figure 5.1.: Flow chart of slope image processing

(a) Light speckle image, *int*

(b) Segmented image, *bin*

Figure 5.2.: Original light speckle image with intensity information (a), and binary image after segmentation (b)

light speckle image sets values smaller than 5 to zero, whereas the intensity values of the speckles are kept.

### 5.1.2. Segmentation

A segmentation procedure is used to define different disjoint objects in an image, here the light speckles (Fig.5.2). An object is a set of pixels with certain properties. Objects are separated by the definition of a four-neighborhood, i.e. only pixels with a common edge are part of the same object, whereas pixels with only a common corner belong to different objects. In this case, the segmentation of the light speckle images can easily be done with a simple count threshold set to 1, because the background intensity is already set to zero by the masking procedure directly after the acquisition. The light speckles are defined as objects to determine their position in the image on the one hand, and to obtain the set of pixel from which the intensity for the height measurement is determined on the other hand.

## 5.2. From Images to Mean Square Slope

Fig. 5.1 shows the flow chart of the operations from the light speckle images to the mean square slope values. In the following part the different steps of data manipulation are described in detail and discussed to obtain the 2-dim slope distribution and the mean square slope.

### 5.2.1. Summation of Images vs. Single Position Detection of Light Speckles in Each Image

The frequency of occurrence of light intensity in a pixel in the light speckle image is directly linked to the frequency of occurrence of the corresponding slope. At first sight, the intensity in the images of the wave gauge is a binary information in the way that an image contains the data for every pixel if it is illuminated or not. But this is only true in the case of perfectly sharp images, when a pixel detects radiation only from a small area in the plane of the light source, so the pixel sees the light source or not. Instead, the water surface acts like a lens, so the image can be blurred (cp. 4.1.3) and a wide area in the plane of the light source is mapped to one pixel. This area can contain the light source but also dark background, so the intensity is an average of the intensities in the mapped area. Therefore, the intensity in a pixel is a continuous quantity proportional to the frequency of occurrence of slope.

For the determination of mean square slope only the RED images are used, because the RED intensity is hardly absorbed by the water, so the intensity corrections are smaller. Since the IR images are taken immediately before the RED ones, they do not contain new information.

To determine the 2-dim slope distribution $p_{\mathbf{s}}(s_x, s_y)$ two different methods are evaluated. The *Summation method* adds up the whole sequence of images, so the result image is an intensity distribution, which is transformed to a slope distribution. The image can be seen as a histogram with pixels as bins. The *Speckle position method* detects the positions of the light speckles in the single light speckle images. The result is a list of statistical distributed positions, which are transformed to slopes. Mean square slope is calculated from this data.

#### Summation Method

This simple method is used for many mean square slope measurements of the wave field in context with gas transfer velocity measurements, e.g. [21]. In times of slow cameras and low data stream the intensity distribution was simply obtained with a laser slope gauge and a long exposure time of the camera up to several seconds or images were added immediately after the acquisition. Here, all light speckle images $I_i(x, y)$ (Fig. 5.2) are added up and normalized by the factor $A$ to obtain the normed intensity distribution

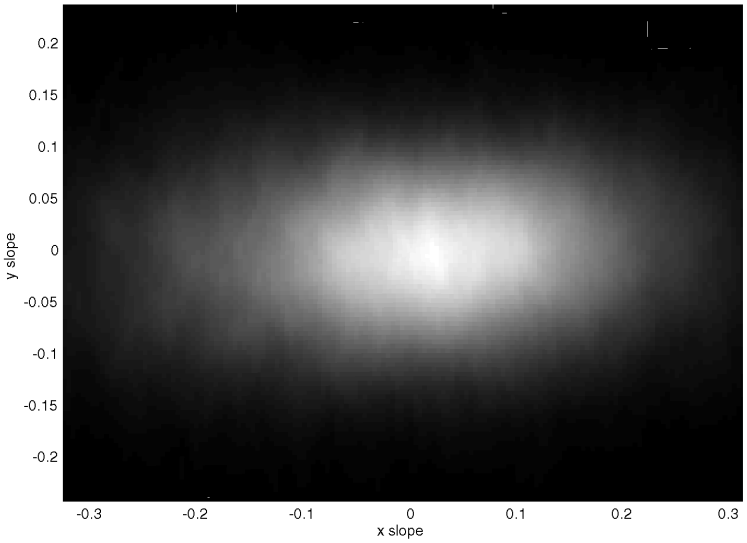


Figure 5.3.: Intensity distribution image transformed to slope coordinates, summation of 5000 light speckle images

image $p_{int}(x, y)$.

$$I_{sum}(x, y) = \sum_{i=1}^{N} I_i(x, y) \tag{5.2}$$

$$A = \sum_{x} \sum_{y} I_{sum}(x, y) \tag{5.3}$$

$$p_{int}(x, y) = \frac{I_{sum}(x, y)}{A} \tag{5.4}$$

Fig.5.3 shows a distribution image, which is already transformed to slope coordinates. The amount of 5000 images is sufficient to obtain a smooth distribution.

Regarding the distribution image as the sum of many light speckles it is useful to take a look at their properties. The light speckles can be characterized by two main parameters: the area, which is the area of the segmented object, and the mean intensity, which is the intensity average over this area. To understand the influence of these two parameters on the distribution and for a further use for the intensity correction three different summations are analyzed. They are indicated with abbreviations that are used in the following part.

- *int.* This abbreviation stands for the summation of light speckle images with the whole intensity information (Fig.5.2(a)).
- *bin.* The single light speckle images are segmented before they are added up. Only the binary information if a pixel is illuminated or not is transferred to the result

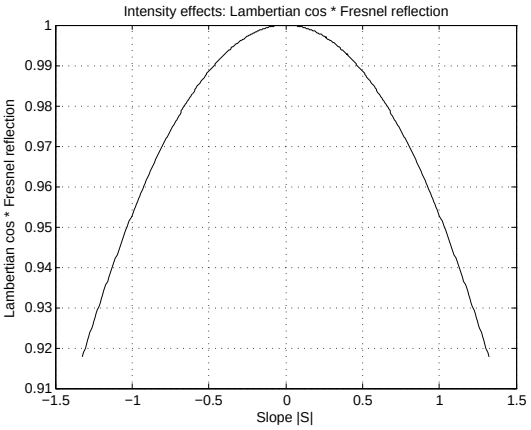


Figure 5.4.: Theoretical intensity dependence on slope: Lambertian cosine and Fresnel reflection

image. The intensity is neglected (Fig.5.2(b)).

- *bin_int.* The distribution image is composed artificially by adding up the binary speckle images from 2., but the corresponding mean intensity from 1. is allocated to each speckle object.

**Intensity Correction** The intensity correction of the slope distribution images is difficult to do. For the summation of images with the full intensity information (*int*) the result image $I_{int}$ is the multiplication of the slope probability distribution $p_{slope}(s_x, s_y)$ and the intensity distribution $p_{intensity}(s_x, s_y)$

$$I_{int} = I_0 \cdot p_{slope}(s_x, s_y) \cdot p_{intensity}(s_x, s_y) \tag{5.5}$$

with a constant scale factor $I_0$. The intensity distribution is the slope dependent intensity detected by the camera, if all slopes had the same probability. The desired slope distribution $p_{slope}(s_x, s_y)$ is obtained by dividing the result image $I_{int}$ with the intensity distribution $p_{intensity}(s_x, s_y)$. The problem is to determine this intensity distribution accurately. In 4.2.1 some effects are presented that cause a slope dependent intensity. The expected theoretical dependence of the intensity on slope, if only these effects played a role, is shown in Fig. 5.4. The intensity decrease is 5% between $|\mathbf{s}| = 0$ and $|\mathbf{s}| = 1$ and it is rotationally symmetric. But the intensity distribution $p_{intensity}(s_x, s_y)$ must be measured experimentally at the setup. For a systematic measurement the slope of the water surface had to be varied in a controlled way, which is not possible at the closed channel and another tricky calibration task. But even in this case only intensity effects at a flat inclined surface could be studied.

For a wavy surface, information about the slope dependent intensity distribution can

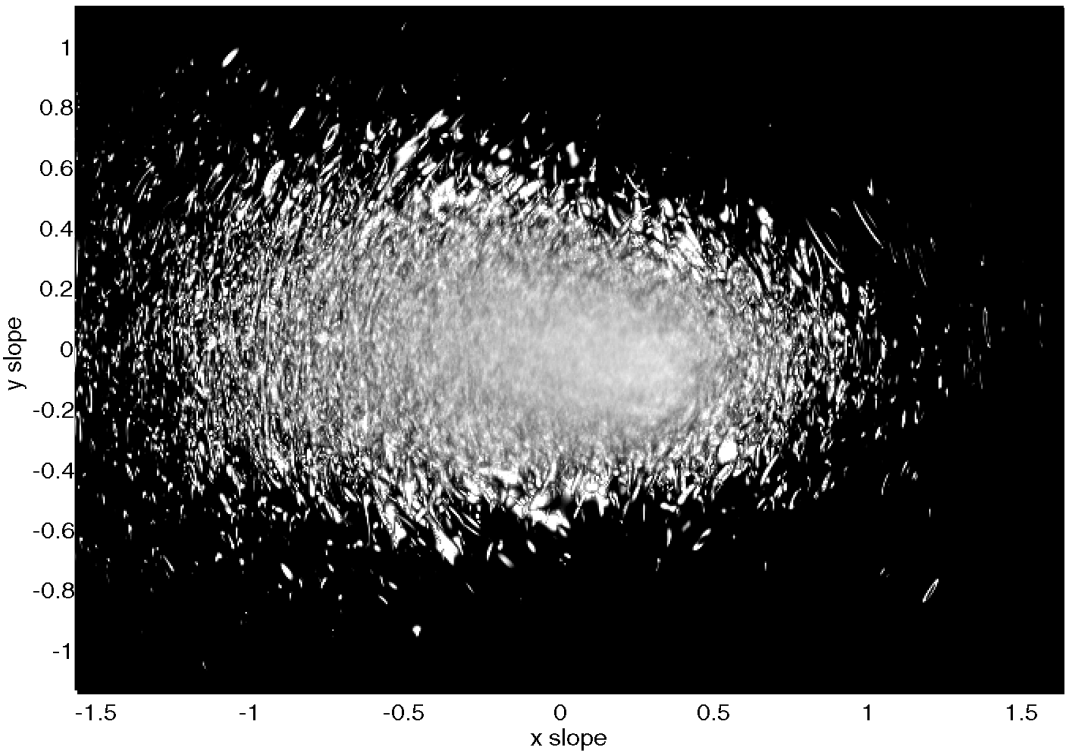


Figure 5.5.: Intensity distribution image at a wind speed of $v_{wind} = 6.5\,\mathrm{m/s}$. In the center the intensity is averaged over a sufficient number of speckles, which leads to a smooth image. To higher slopes single speckles can be seen. At the left edge of the image few speckles for maximum negative slope in x-direction are outside of the field of view for this maximum wind speed.

be obtained in two ways. First, the intensity data of each light speckle, originally extracted for the height measurement, can be plotted against slope coordinates of the light speckles. Fig. 5.6(a) and Fig. 5.6(b) show the decrease of averaged speckle intensity for higher slopes at a wind speed of $6\,\frac{\mathrm{m}}{\mathrm{s}}$ for both directions. The intensity decreases much more than predicted by the effects shown in Fig. 5.4. Second, an intensity distribution image can be obtained from the summation images. The *int* summation image with the full intensity information is divided by the *bin* summation image, which contains the number of illuminations for each pixel, i.e the frequency of occurrence. The result image (Fig. 5.5) shows the mean intensity for each pixel. In the center of the image a sufficient number of light speckles are averaged, whereas in the regions of higher slopes single light speckles can be seen, so intensity values are not averaged over a sufficient number of speckles in these regions. Profiles in x and y direction can be seen in Fig. 5.6(c) and Fig. 5.6(d).

The comparison of Fig. 5.6(a) and Fig. 5.6(b) with Fig. 5.6(c) and Fig. 5.6(d) shows a

stronger reduction of intensity to higher slopes for the data from single speckle intensities. It can be explained by the observation that light speckles at higher slopes are smaller and less intense (see Fig. B.1 and Fig. 5.6(a), Fig. 5.6(b)). Unlike for the single speckle intensities (5.6(a), 5.6(b)), in the summation method (from which the intensity distribution image is calculated) the less intense speckles at higher slope are weighted with their area, so the less intense speckles have less impact on intensity reduction due to their small area. For the intensity correction of a summation image of type *int* the correction image Fig. 5.5 can be used, but only its center region with sufficient statistical data. In the smooth center region $|\mathbf{s}| < 0.5$ the profiles (Fig. 5.6(c), Fig. 5.6(d)) show a maximum intensity decrease of about 10%. This is a much stronger decrease than the 1% predicted by the simulated effects of Lambert cosine and the Fresnel reflection (Fig. 5.4). The water surface forms lenses that depend on the surface curvature and are slope dependent. Probably, blurring effects due to these lenses are responsible for this additional decrease in intensity.

Some problems occur for an accurate intensity correction, that improves the data instead of adding new errors. First, to obtain a smooth intensity distribution image over a wide slope range a much larger number of light speckle images must be added than the 10000 images taken for this intensity image. Secondly, small slope values are more probable than higher slope values, which will be one result of this study, but can already be seen in Fig.5.5. Hence, the intensity correction, which varies only in the range of few % for the most probable slopes (see profiles), has little impact on the main parameters of the slope distribution $p_{slope}(s_x, s_y)$. Thirdly, without an experimental extensive systematic variation of the surface slope, an intensity correction image can only be obtained for a wavy water surface by dividing the *int* summation image with the *bin* summation image as described above. The *bin* summation image is already the slope distribution without intensity information of the speckles. A universal intensity correction image could be useful to correct slope distribution images, which are the result of a time-saving immediate summation when the segmentation operation on single light speckle images is not possible. But the image processing operations that are necessary for an analysis based on single light speckle images can be done in the short time of some minutes. For these reasons, an intensity correction is at first neglected and the results are interpreted with respect to this neglect.

**Calculation of Mean Square Slope from Distribution Images** Three slope distribution images (*int, bin, bin_ int*) are obtained from the *summation method*. As can be seen in the flow-chart (Fig. 5.1), the pixel coordinates of the images are transformed to slope coordinates and mean square slope values are calculated from the distribution

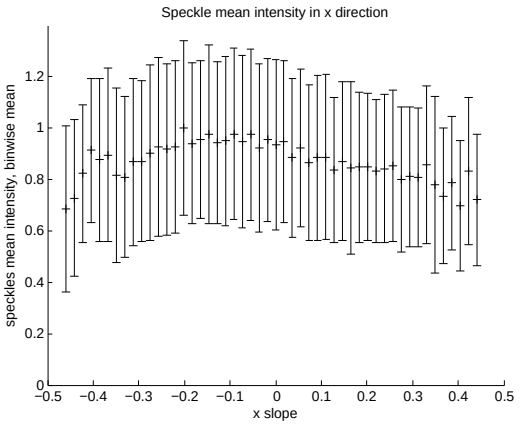


(a) Mean speckle intensity in x direction (long-wind)

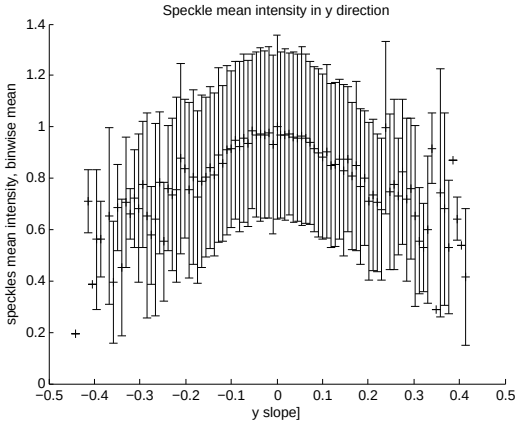


(b) Mean speckle intensity in y direction (cross-wind)

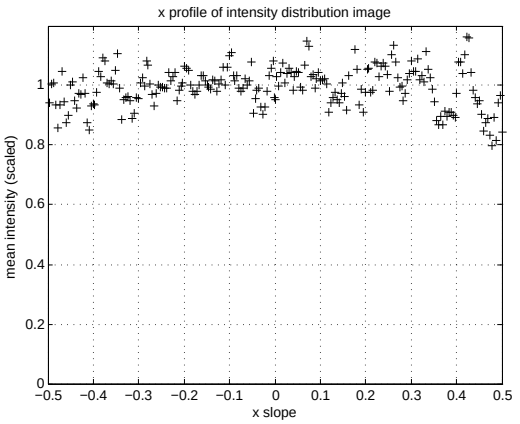


(c) x profile (upwind) of mean intensity in intensity distribution image

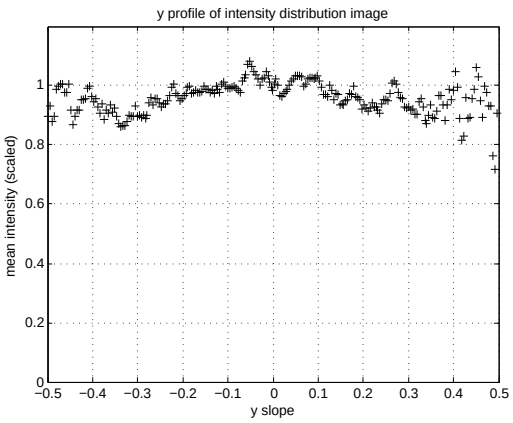


(d) y profile (crosswind) of mean intensity in intensity distribution image

Figure 5.6.: Intensity dependence on slope at a wind speed of 6.5 m/s

images.

$$p(i,j) = \frac{I(i,j)}{I_{sum}} \tag{5.6}$$

$$I_{sum} = \sum_{i=1}^{M}\sum_{j=1}^{N} I(i,j) \tag{5.7}$$

$$\langle s_x \rangle = \sum_{i=1}^{M}\sum_{j=1}^{N} p(i,j)s_x(i,j) \tag{5.8}$$

$$\langle s_x^2 \rangle = \sum_{i=1}^{M}\sum_{j=1}^{N} p(i,j)s_x(i,j)^2 \tag{5.9}$$

$$\sigma_{s_x}^2 = \langle \Delta s_x \rangle^2 = \langle s_x^2 \rangle - \langle s_x \rangle^2 \tag{5.10}$$

$I(i,j)$ is the intensity value for the pixel at slope coordinate $(s_x(i,j), s_y(i,j))$. $p(i,j)$ is the probability for the slope $(s_x(i,j), s_y(i,j))$. Image dimensions are $M = 640$ and $N = 480$. Calculations are done for $S_y$ respectively.

The finite width of the light source leads to a non-zero mean square slope for a flat water surface. The slope distribution is convolved with the mean intensity distribution of the light speckles, but compared to the slope distribution the width of the light speckles is very small.

### Speckle Position Method

The basic idea of this method is to use light rays from the light source to the camera as pointers, that point on the slope values that occurred. This enables a measurement technique without the necessity to measure intensities in the images, which is a tricky task as can be seen in the paragraphs above. Only positions are measured and the slope distribution can be determined only with geometrical calculations and statistics.

For this method, which is referred to as *pointwise*, the center positions of all speckles are determined. An operator (*ObjPos*) in the software *heurisko* calculates the center of mass of objects with respect to the gray values $g_i$ in the object.

$$(x,y)_{center} = \left( \frac{\sum_i g_i \; x_i}{\sum_i g_i}, \frac{\sum_i g_i \; y_i}{\sum_i g_i} \right) \tag{5.11}$$

Speckle objects are defined by the same binary image sequence used for the *bin* summation image. The center positions are written to a list. At the same time basic properties of the speckles are determined such as the area and the mean intensity. The center positions can easily be transformed to slope coordinates, so mean square slope is calculated as the variance of the slope values

$$\sigma_{s_x}^2 = \langle \Delta s_x \rangle^2 = var(s_x) \tag{5.12}$$

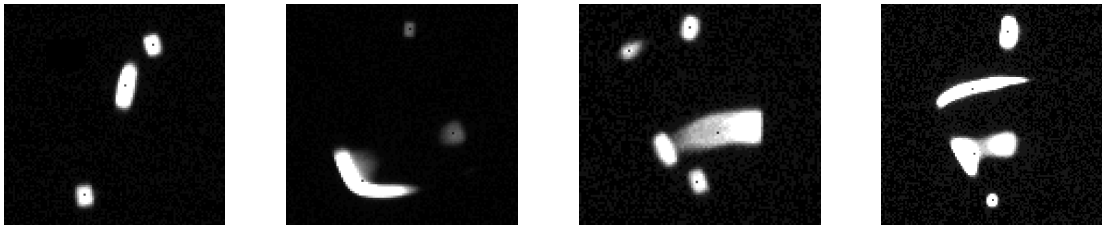

(a) Circular speckles (b) Bended speckle (c) Unseparated double speckle (d) Different speckle shapes

Figure 5.7.: Speckle position detection. The detected center of the speckles is marked with a small point. Good representation of the speckle position by the center of gray values for circular speckles (a). Non-circular speckle shapes with a bad representation of the shape by the center point (b),(c) and (d)

for $s_y$ respectively. In this way, all speckles are weighted equally, independent of their area or intensity. To be able to compare the results of the speckle position method (*pointwise*) to the results of the summation method (*int, bin, bin_ int*), the variance of the slopes is also calculated from the speckle positions with weighting with respect to the area and the intensity of the speckles. For example mean square slope $\langle s_x^2 \rangle$ weighted with area:

$$p^i_{area} = \frac{area_i}{\sum_i area_i} \tag{5.13}$$

$$\langle s_x \rangle = \sum_i p^i_{area} s^i_x \tag{5.14}$$

$$\langle s_x^2 \rangle = \sum_i p^i_{area} (s^i_x)^2 \tag{5.15}$$

$$\sigma^2_{s_x} = \langle \Delta s_x \rangle^2 = \langle s_x^2 \rangle - \langle s_x \rangle^2 \tag{5.16}$$

$area_i$ is the size of the $i^{th}$ light speckle in units of pixel.

An advantage of the speckle position method is the possibility to do an immediate height correction. The slope that corresponds to a position of a speckle in the image depends on the water height, because a variation of the water height changes the geometry of the wave gauge. With the knowledge of the water height for each speckle from the height measurement, the slope can be corrected for every single speckle. In the linear wind wave flume the fetch is so short, that only a small wave height occurs. Additionally, the single height values have a strong variation which is not realistic, so the correction would induce more errors than correct errors. Therefore, a height correction is not executed for the measurements in the small linear flume. For higher waves in larger flumes the correction should be considered.

The main disadvantage of the method is the fact, that speckles are reduced to their

center of gray value. The center point is a good representation for the position of a circular speckle, but for shapes that deviate a lot from a circular shape the center of gray values does not respect the properties of the shape and can even be outside of the speckle. Fig. 5.7 shows examples of typical speckle images with marked center points.

## 5.3. From Images to Root Mean Square Wave Height

The absorption length $l$ in water is calculated according to the following equation

$$l = -\frac{1}{(\alpha_{IR} - \alpha_{RED})} \, ln\left(\frac{I_{IR}}{I_{RED}}\right) + C. \tag{5.17}$$

To measure the IR and RED intensity ($I_{IR}$, $I_{RED}$) of a speckle a combined binary image is determined from the IR and RED image to define the speckle binary object. First of all, two different binary images are obtained from a segmentation of the IR and RED image with a threshold of 1. They are combined by a logical OR operation, so the speckle object in the result binary image contains the set union of both the IR and RED speckle object. Speckle intensities are measured in the speckle object defined by this common binary image. The binary image is used as a mask and the mean intensity over all pixels in one object is determined. Both intensities are averaged over the same numbers of pixels $N$, so the factor $\frac{1}{N}$ from the averaging vanishes in the ratio of both intensities in Eq. 5.17. The main reason to choose a combined binary image is the problem of allocation of corresponding speckle intensities. For two corresponding IR and RED binary images it is possible to obtain two different numbers of speckles, because two close speckle objects might be distinct in one binary image and conjunct in the other (cp. third speckle from top in Fig 5.7(d)). This is avoided with the combined binary image.

Intensities are measured as the average over all pixels of a light speckle, because the noise of the camera is a significant error of the intensity measurement. By averaging over $N$ pixels the error is reduced by a factor $\frac{1}{\sqrt{N}}$. For very small light speckles this factor is close to 1, so the error is high. These light speckles are excluded from the analysis by a threshold for the minimal $N$ called *area threshold*. It is set to $N_{thresh} = 50$, so the reduction of the error due to camera noise is at least $\frac{1}{\sqrt{N_{thresh}}} \approx \frac{1}{7}$.

However, the combined binary image as a set union of the IR and RED binary images covers up the cases, when one of the two speckle objects is much smaller than the other. Then, the IR and RED intensity values show big differences and the calculated height values are totally unrealistic. These values are excluded from the analysis of the rms wave height.

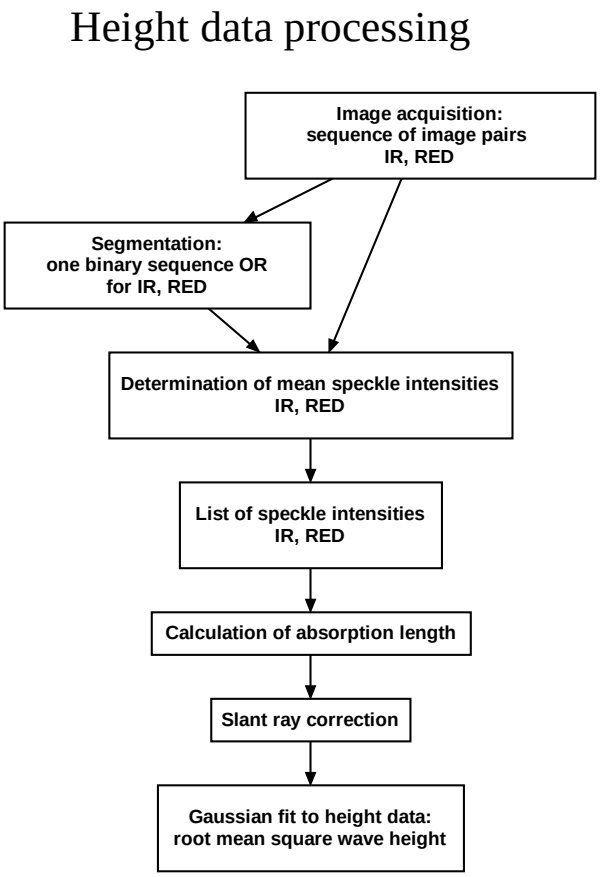


Figure 5.8.: Image and data processing steps from images to rms wave height

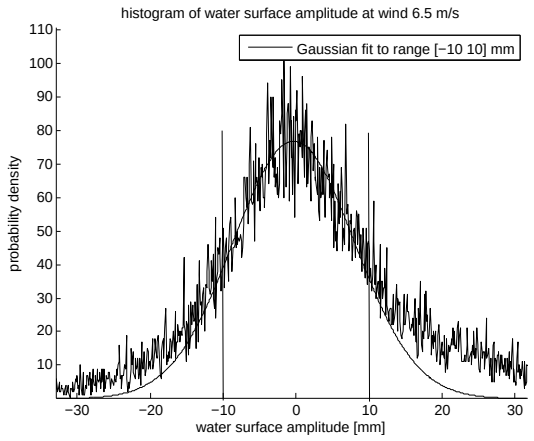


Figure 5.9.: Gaussian fit to the histogram of the water surface amplitude $h$ to determine the rms wave height $\sigma_h$

The values for the amplitude of the water surface $h$ are calculated, with the length $b$ calculated from the intensity values and $d_2$ and $\theta_2$ as defined in Fig. 3.1. This includes the slant ray correction, which is basically the factor $\cos\theta_2$ in Eq. 5.18. For a detailed calculation see A.1.

$$h = \left[(b - \langle b \rangle) + \frac{d_2}{\langle \cos\ \theta_2 \rangle}\right] \cos\theta_2 \tag{5.18}$$

$$\sigma_h = \langle \Delta h \rangle = \sqrt{var(h)} \tag{5.19}$$

A Gaussian is fitted to the histogram of the amplitude values $h$ to determine the root mean square wave height $\sigma_h$, the standard deviation $\sigma_h$ of the amplitude (Fig. 5.9). Unrealistic values for a wave height higher than 10mm are ignored for the fit.

Basically three effects lead to a variation of the measured water height (see also Sec. 4.2.4).

1. Intensity variations due to camera noise and LED noise. These effects can be determined from measurements at a flat water surface.

2. Fast movements of the water surface between the two IR and RED images and lens effects of the rough water surface can lead to very different speckle size which results in strong difference in intensities and therefore biases the height values.

3. The actual quantity of interest is the variation of the wave height that varies the absorption length. This quantity has to be measured.

For independent variables the three contributions to the measured variation of the water height can be added.

$$\sigma^2_{h\ meas} = \sigma^2_{noise} + \sigma^2_{bias} + \sigma^2_{h\ wave} \tag{5.20}$$

The contribution of the LED and Camera noise is constant. It can be determined from measurements at a flat water surface and can be subtracted (1). However, the contribution from different speckle size due to fast variations of the water surface depends on the wave field, so it cannot be determined separately (2). Its contribution to the final rms wave height value can be reduced by the limitation of the fit range to realistic values, but then the rms wave height from the Gaussian fit depends on the fit range. Therefore, the final rms wave height values still include a contribution from the variation due to different speckle size and the rms wave height is overestimated.

# 6. Measurements and Results

## 6.1. Description of the Linear Wind Wave Flume

Wave slope and height measurements have been performed in the linear wind wave flume in the Aelotron laboratory at the Institut für Umweltphysik (IUP), Heidelberg (Fig. 6.2). The linear flume was constructed for the research on gas transfer with a Laser Induced Fluorescence (LIF) technique to visualize gas concentrations in the water. A fluorescent dye will be used whose fluorescent intensity depends on the gas concentration.

In contrast to a circular wind wave flume, no secondary rotational air flows due to centrifugal forces occur in a linear flume. The fetch is limited to the length of the water basin. At the end of the water basin the waves are dissipated by a beach made of flexible plastic tubes to avoid waves that are reflected at the wall and run against the wind direction. The water basin has a length of 4 m and a width of 0.42 m. Water depth is about 95 mm. The air circulates in a closed loop, where it is accelerated by an air fan in the lower part and flows over the water basin in the upper part. An air flow homogenizer made of many parallel tubes serves to provide a laminar air flow at the entrance of the water basin. A smooth diminution of the air flow cross section in front of the water basin leads to higher achievable wind speeds.

The wind speed is measured with a Prandtl tube, which compares the static pressure to the total pressure of the air flow, so the wind speed can be calculated from Bernoulli's equation of conservation of energy in a fluid

$$\frac{1}{2}\rho u^2 + p_{stat} + \rho g h = const \tag{6.1}$$

with the fluid density $\rho$, its velocity $u$, the local static pressure $p_{stat}$, the gravitational constant $g$ and the height of the fluid particle $h$. For small height variations of the flow the term $\rho g h$ is constant, so Eq. (6.1) can be written

$$\frac{1}{2}\rho u^2 + p_{stat} = p_0 = const \tag{6.2}$$

where the term $\frac{1}{2}\rho u^2$ is referred to as the dynamic pressure and the constant $p_0$ as the

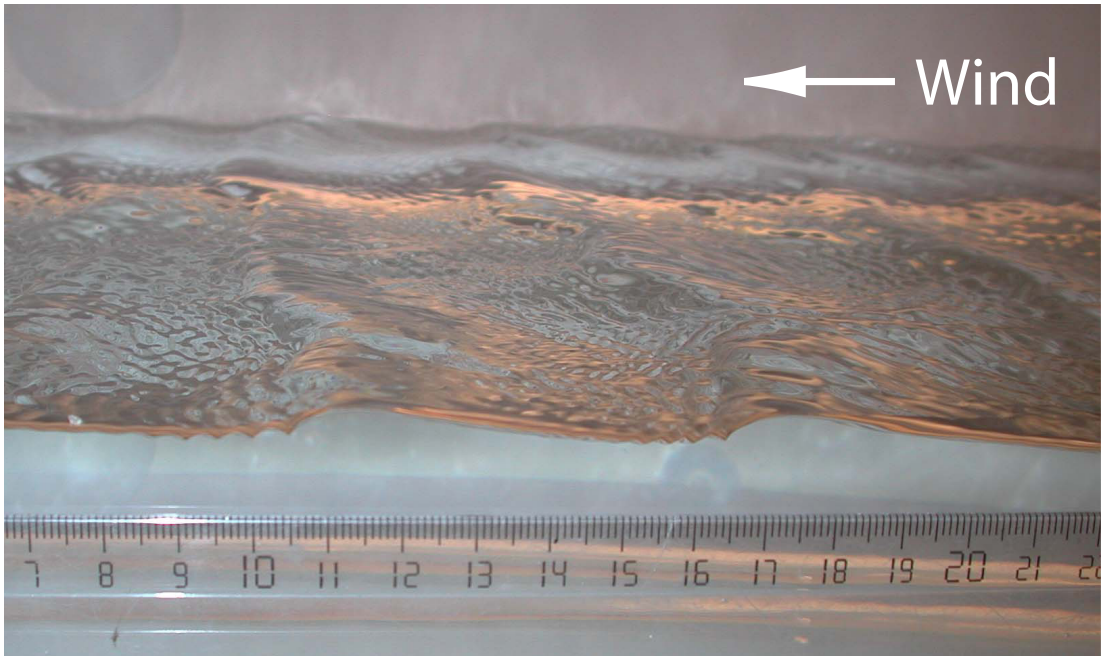


Figure 6.1.: Side view on the water surface at 6 m/s wind and 2.40 m fetch. Exposure time is 4 ms. Capillary waves with a wavelength of few mm sit in front of short gravity waves with $\lambda \approx 6$ cm.

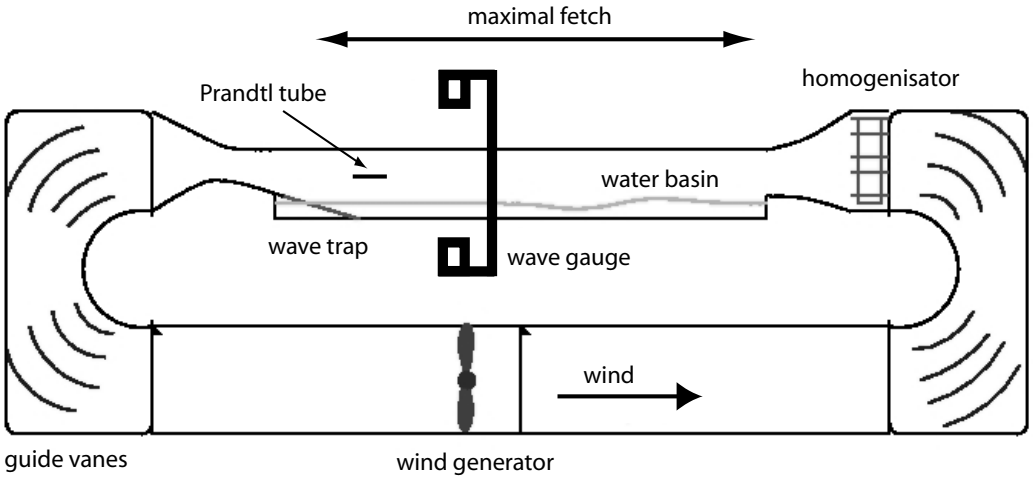


Figure 6.2.: Schematic sketch of the wind wave flume. Total length is 7 m, the length of the water basin 4 m and water depth about 95 mm. Wind speed reaches 7 m/s at 10 cm above the water surface.

total pressure. So the air flow velocity is

$$u = \sqrt{\frac{2}{\rho}(p_0 - p_{stat})} \tag{6.3}$$

The Prandtl tube is fixed $(12 \pm 1)$ cm above the mean water level at a fetch of about 2.70 m (Fig. 6.2). The statistical error of the wind speed is about 0.03 m/s. It is important to note that compared to other wave flumes or measurements in the field the wind speed in the linear flume is measured very close to the water surface. As the wind speed increases with the height - in the ideal case according to the logarithmic wind profile, the measured wind speed directly above the water surface corresponds to a significantly higher wind speed further above the water surface. Therefore, the given wind speed has to be seen as a reference value mostly useful for the comparison of measurements in the same flume. The friction velocity is a more adequate quantity to describe the stress on the water surface.

Friction velocities are taken from Ueltzhöffer [45]. In that study the air side friction velocity is determined from measurements of the vertical wind profile in the linear wind wave flume. A logarithmic wind profile (Eq. (2.32)) is fitted to the data to obtain the friction velocity $u_*$. The wind profiles were taken with a movable Prandtl tube at the end of the water basin at a fetch of about 2.70 m. This is close to the position of the wave gauge at a fetch of 2.40 m. However, the friction velocity values were taken at other wind speeds than the wave field parameters. Therefore, a linear interpolation yields the friction velocities for the slope measurements in this study.

The water side friction velocity is more common in literature than the friction velocity on the air side. For stationary conditions the momentum flux density $\tau = u_*^2 \rho$ is constant at the air and the water side of the air-water interface.

$$\tau_a = u_{*a}^2 \rho_a = u_{*w}^2 \rho_w = \tau_w \tag{6.4}$$

Hence, the friction velocities scale as

$$u_{*w} = \sqrt{\frac{\rho_a}{\rho_w}}\, u_{*a} \approx \frac{1}{28.8}\, u_{*a}. \tag{6.5}$$

The air side friction velocity $u_{*a}$ is transformed to the water side friction velocity $u_{*w}$. $u_{*w}$ typically has values of about 1 cm/s. The interpolated water side friction velocity as a function of the wind speed measured with the Prandtl tube is shown in Fig. 6.3.

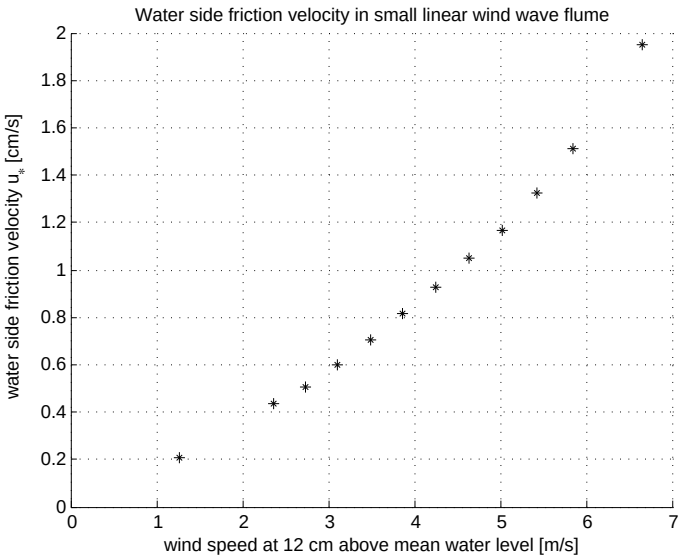


Figure 6.3.: Water side friction velocity $u_{*w}$ as a function of the wind speed measured with the fixed Prandtl tube. From Ueltzhöffer [45].

## 6.2. Wave Slope Distributions and Mean Square Slope

### 6.2.1. Comparison of Different Image Processing Methods for Mean Square Slope

As described in 5.2 different image processing methods to obtain the mean square slope values are tested. Fig. 6.4 shows the results of the different methods dependent on the wind speed.

The comparison of the data leads to the following conclusions (Fig. 6.4).

1. The light rays from the light source that are refracted at the water surface into the camera cannot be considered as simple pointers that point on a position on the CCD chip and the slope is calculated from that position. The point-like light source is imaged as extended light speckles. The shape and the intensity of these light speckles in the images have to be taken into account, since these speckle properties influence the slope probability distribution and therefore the mean square slope values.

2. The mean square slope data from the *pointwise* method (+) is above the data of all other methods. The slope values from the light speckles are all weighted equally for the *pointwise* method, whereas all other methods weight the slope data from the light speckles with the light speckles' properties: area and/or intensity.

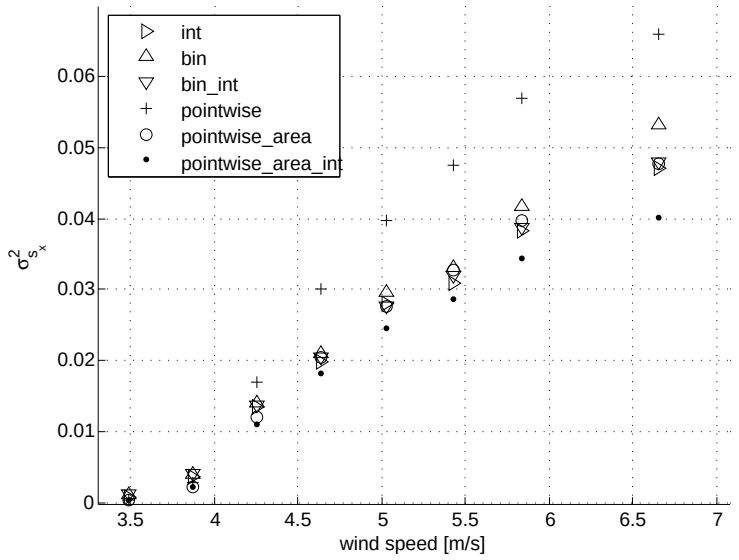


(a) Mean square slope data in x-direction (upwind) for different analysis methods

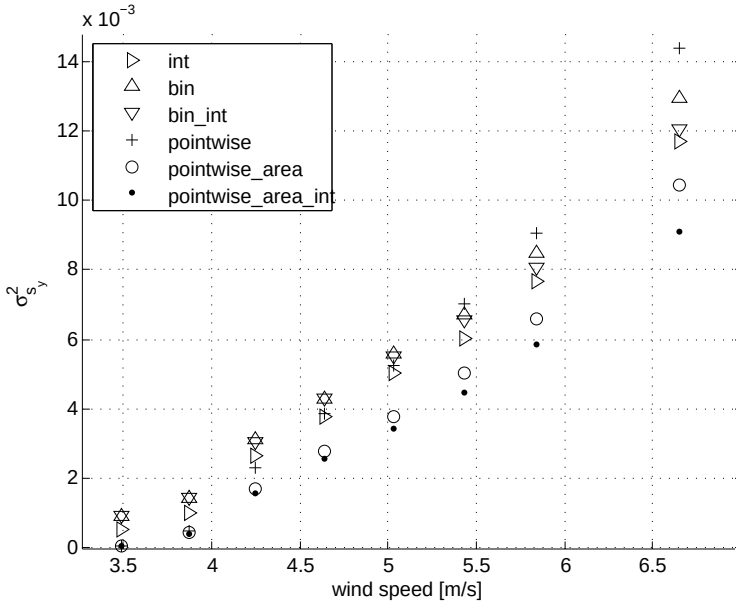


(b) Mean square slope data in y-direction (crosswind) for different analysis methods

Figure 6.4.: Comparison of mean square slope data from different image processing methods

Since area and intensity of the speckles decrease with higher slopes, the mean square slope is overestimated with the *pointwise* method, that ignores this effect.

3. If the slope data from the *pointwise* method is additionally weighted with the light speckle properties 'area' ($\circ$) and 'area'&'intensity' ($\cdot$), the mean square slope data decreases, as expected. Especially the weighting with only 'area' ($\circ$) is promising, as the data of this method is very close to the mean square slope data of the summation methods ($\triangleright$, $\triangle$, $\bigtriangledown$). For the case of wave fields with higher waves that necessitate a height correction, the 'area' weighted ($\circ$) method could be used.

4. For the summation method the difference between the *int* type ($\triangleright$) and the *bin* type ($\triangle$) method can be fully explained by the additional weighting with the speckle intensity for the *int* type, which is not included in the *bin* type method. Hence, the inclusion of the intensity weighting for the *bin* type method leads to the *bin_int* data ($\bigtriangledown$), which is in agreement with the *int* data ($\triangleright$).

5. Fig. 6.5 shows the anisotropy of the light speckle shape. For the *pointwise* methods ($+$, $\cdot$, $\circ$) that ignore the anisotropy of the light speckles, the ratio of mean square slopes in x- and y-direction $\sigma_{s_y}/\sigma_{s_x}$ is smaller than for the summation methods that respect the speckle shape. Hence, the mean speckle shape is stretched in y-direction (crosswind). This is in agreement with wave trains that propagate particularly in upwind direction.

6. For the following analysis the *int* type summation method is chosen ($\triangleright$). This method is weighted with the area and the intensity of the speckles. The intensity is a source of error on the one hand, because it is not constant for all slopes (see 5.2.1, Intensity correction). But on the other hand the inclusion of the intensity information respects the effect that the light speckles are blurred, so the intensity is a continuous quantity proportional to the frequency of occurrence of slope. A further advantage of this method is the fact that most of the former slope measurements also used the simple summation method to obtain the slope distribution without any manipulations on the single light speckle images. Therefore, the analysis methods are similar, so the results can be compared better to other measurements.

### Error of Mean Square Slope

The mean square slope value calculated from the slope distribution is a statistical quantity and has itself an statistical error. But the relative statistical error of the mean square slope value is in the order of magnitude of $\frac{1}{\sqrt{n}} = \frac{1}{100}$, with $n = 10000$. Hence,

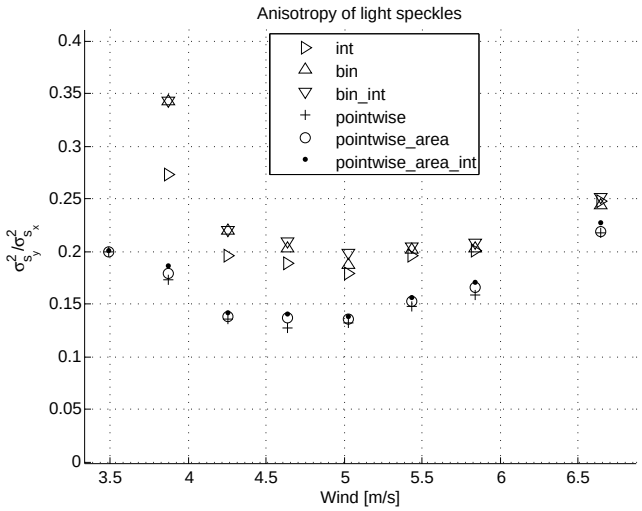


Figure 6.5.: Different ratios $\sigma_{s_y}/\sigma_{s_x}$ for the *pointwise* and the summation method indicate a anisotropic mean light speckle shape.

the main error of the mean square slope value is the systematic error caused by the analysis method. The values for the chosen *int* method ($\triangleright$) differ less than 10% from the methods that do not include intensity information ($\bigtriangledown$, $\circ$). So an error of 10% can be seen as the upper limit for the mean square slope values.

### 6.2.2. Mean Square Slope Dependence on Wind Velocity

The slope is measured at a fixed fetch of 2.38 m. The wind speed is varied from 0 to 6.7 m/s at 12 cm above the mean water level. This corresponds to a friction velocity range on the water side from 0 to 2 cm/s. 10000 RED light speckle images are used to obtain the slope probability density distribution.

#### Slope Probability Density Distributions

Fig. 6.6 shows the probability density distribution $p_s(s_x, s_y)$ for slope at four different wind speeds. The occurrence of higher wave slopes for higher wind speed leads to a wider distribution, i.e. to a higher mean square slope. The distributions are symmetric in crosswind direction for all wind speeds (Fig. 6.7). In upwind direction the distribution has a skewness to negative slopes that increases with the wind speed (Fig. B.2). For the highest wind speed of $u_{wind} = 6.7\,\mathrm{m/s}$ the maximum of the upwind slope distribution is at $s_x = -0.15$ (Fig. 6.7). This can be explained by non-linear wave-wave interactions such as small steep capillary waves on the face of small gravity waves (see Gram-Charlier

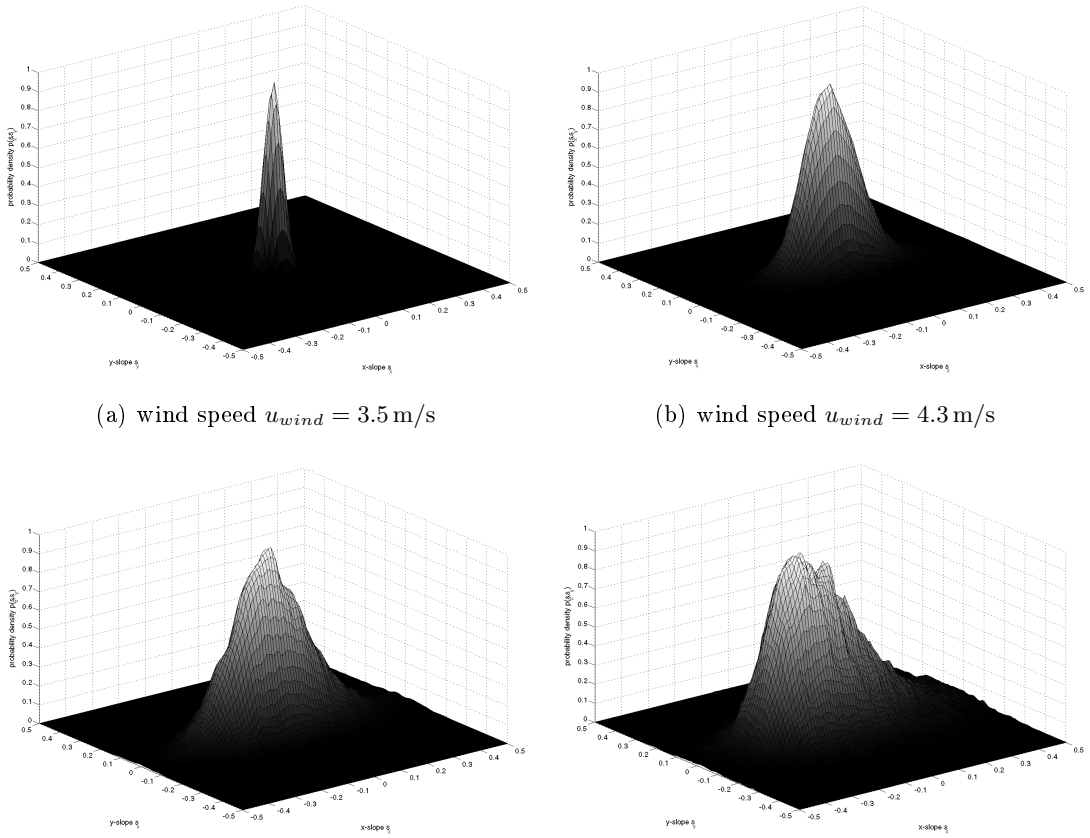

(a) wind speed $u_{wind} = 3.5\,\mathrm{m/s}$

(b) wind speed $u_{wind} = 4.3\,\mathrm{m/s}$

(c) wind speed $u_{wind} = 5.0\,\mathrm{m/s}$

(d) wind speed $u_{wind} = 6.7\,\mathrm{m/s}$

Figure 6.6.: 2-dim slope probability density distribution at four different wind speeds

distribution in 2.5 and Fig. 6.1).

Fig. 6.8 shows the total mean square slope values at different wind speeds for the measurement with the USSG and for a measurement by Lauer [28]. Lauer's measurements were done with a Reflective Slope Gauge (RSG) in the linear wind wave flume of the Scripps Institute of Oceanography, La Jolla. For the USSG measurement in the linear wind wave flume at the IUP, the water surface stays flat up to a limit wind speed of 3.5 m/s. Above that limit wind speed waves occur suddenly and the mean square slope increases strongly with increasing wind speed. For higher wind speeds the mean square slope values are similar for both measurements.

A special feature is the limit wind speed when steep waves first occur, i.e. the wind speed when the mean square slope increases abruptly. The wind speed was measured in different heights in both experiments, so the comparability is doubtable. Nevertheless, the limit wind speed seems to depend on the fetch in a way that for a longer fetch less wind is necessary to induce the first ripple waves. This can be expected since for a

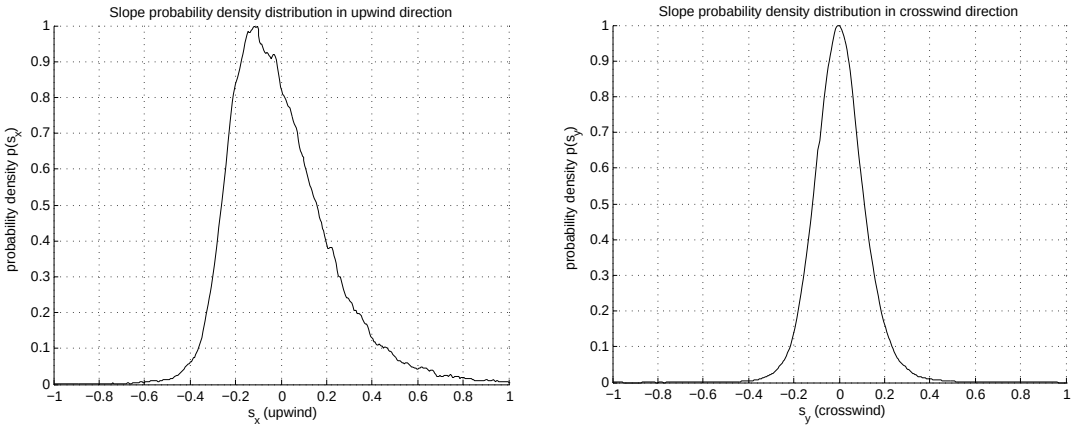


(a) Slope probability density distribution in upwind direction

(b) Slope probability density distribution in crosswind direction

Figure 6.7.: 1-dim directional slope distributions at $u_{wind} = 6.7\,\mathrm{m/s}$. The slope distribution in upwind direction (a) shows a skewness to negative slopes with a maximum at $s_{peak} = -0.15$

longer fetch the time for an energy transfer to the wave field is longer. In the Lauer [28] measurements, for the longest fetch of 11.20 m the first waves occur at a limit wind speed of about 2 m/s, for 4.90 m fetch at about 3 m/s (Fig. 6.8(b)) and for the USSG measurement for 2.38 m fetch at 3.5 m/s (Fig. 6.8(a)).

Fig. 6.9 shows the ratio of the mean square slope in upwind and crosswind direction $\sigma_{s_y}^2/\sigma_{s_x}^2$, which is a measure for the anisotropy of the wave field. The ratio is 1 for an isotropic wave field and 0 for maximal anisotropic waves, e.g. a plane wave that propagates in upwind direction. For a relatively flat water surface up to the limit wind speed of 3.5 m/s the slope distribution is dominated by the light source. It has the same isotropic shape as the circular light source, so the ratio is 1. Above the limit wind speed the ratio is 0.2 and increases only slightly with wind speed. It indicates a wave field that is highly directed in upwind direction. Compared to measurements by Lauer, the ratio is smaller and depends less on wind speed. This could be explained by the shorter fetch, since the slope component in crosswind direction develops from a wave-wave interaction, so a certain fetch is necessary that higher crosswind slopes occur. The data from Cox and Munk [9] from field measurements in Fig. 6.9(b) show much higher $\sigma_{s_y}^2/\sigma_{s_x}^2$ ratios that indicate higher crosswind slope components in the wave field on the free ocean. This can be explained by the very long fetch on the ocean. Another parameter that might lead to different crosswind slope components is the different variation of the wind direction on the ocean and in flumes.

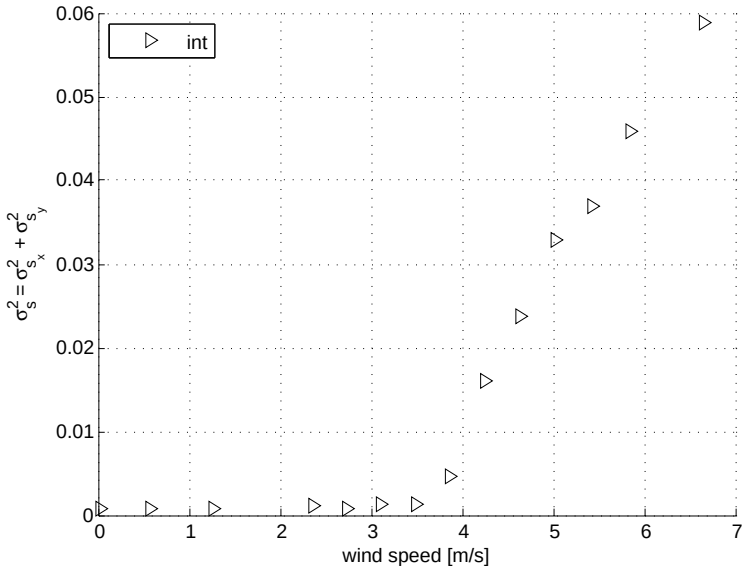


(a) Total mean square slope from the USSG. Fetch is 2.38 m

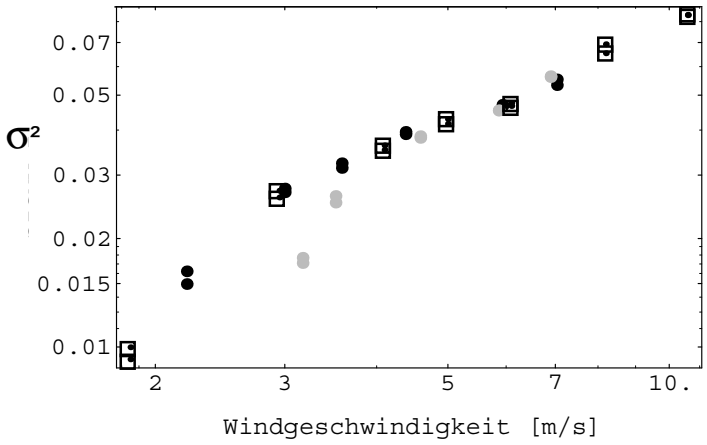


(b) Total mean square slope from Lauer. Fetch is 11.20 m (black dots and squares) and 4.90 m (gray dots)

Figure 6.8.: Comparison of mean square slope dependence on wind speed with measurements by Lauer [28] in the linear wind wave flume of the Scripps Institute of Oceanography

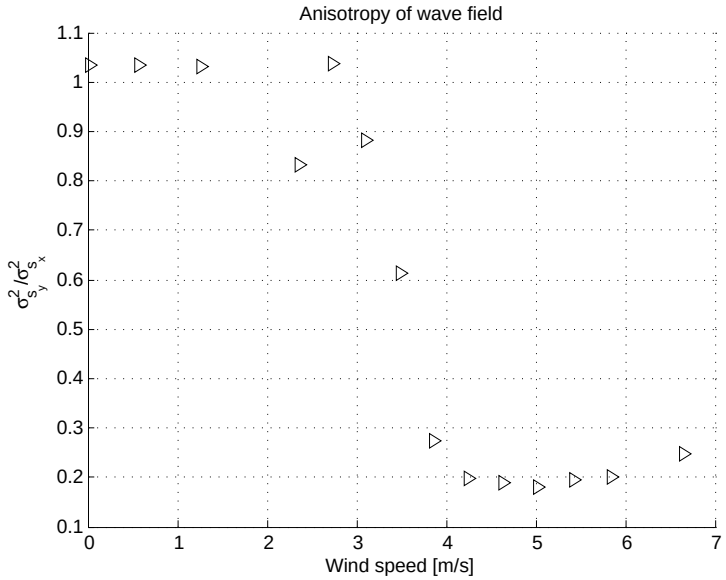


(a) $\sigma^2_{s_y}/\sigma^2_{s_x}$ from the USSG measurement

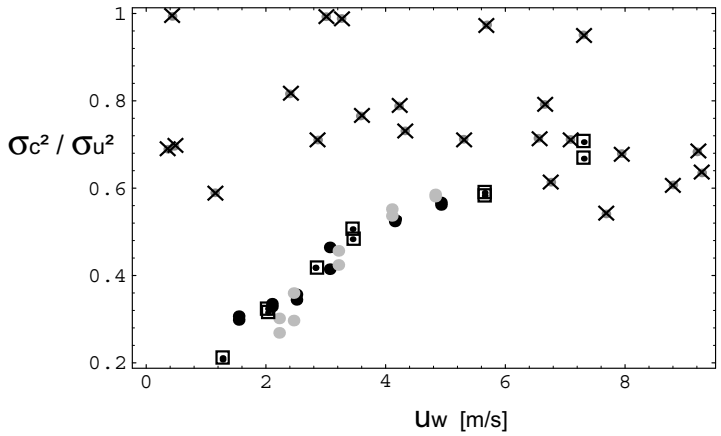


(b) Cox&Munk (×). RSG Lauer: fetch 11.20 m (black dots and squares) and fetch 4.90 m (gray dots)

Figure 6.9.: Comparison of the ratio $\sigma^2_{s_y}/\sigma^2_{s_x}$, which is a measure for the anisotropy of the wave field.

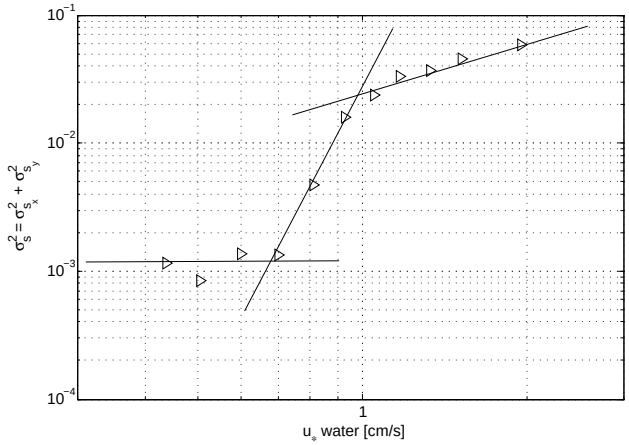


(a) Dependence of mean square slope $\sigma_s^2$ on friction velocity. The fetch is 2.38 m.

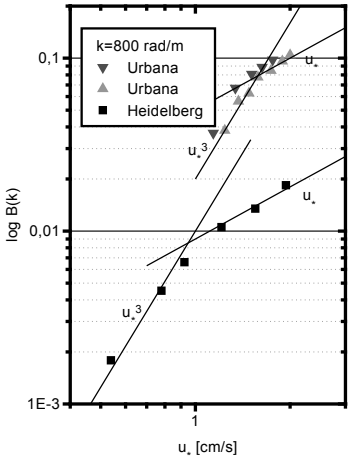


(b) Dependence of spectral density B($\mathbf{k}$) on friction velocity $u_*$ for small scale waves with $\lambda \approx 8\,\mathrm{mm}$ from Balschbach [1]

Figure 6.10.: Momentum flux into the wave field. Dependence of mean square slope $\sigma_s^2$ and spectral density $B(k = 800\,\mathrm{rad/m})$ on the friction velocity. For both a change of the relation at $u_* \approx 1\,\mathrm{cm/s}$ can be seen.

### 6.2.3. Mean Square Slope Dependence on Friction Velocity

The friction velocity $u_*$ is directly linked to the momentum flux into the water via $\tau = \rho\, u_*^2$. For the research on the evolution of the wave field it is a more significant quantity than the wind speed, since the wind speed depends on the height above the water surface. When momentum is transferred from the air flow to the water, waves occur and the wave field develops. This can be seen in the wave spectrum (cp. Fig. 2.3). The mean square slope is basically the integral over the energy spectrum (Eq. (2.43)). Hence, a higher momentum transfer is expected to result in an increase of the mean square slope of the wave field.

This is shown in Fig. 6.10(a). Three parts can be identified with different dependence on friction velocity. For low friction velocities almost no waves occur. At a friction velocity of about 0.7 cm/s corresponding to the limit wind speed found in Fig. 6.8 waves start to develop. Up to $u_* \approx 1\,\mathrm{cm/s}$ the mean square slope in the wave field increases strongly with increasing momentum transfer. Above 1 cm/s the relation changes and the mean square slope increases less. The change of the relation is also reported by Jähne [17, Fig. 4.11], and by Klinke [25, Fig. 8.10] and Balschbach [1, Fig. 5.12] for the spectral density $B(\mathbf{k})$ of small scale waves with $\lambda \approx 8\,\mathrm{mm}$. They find a relation proportional to

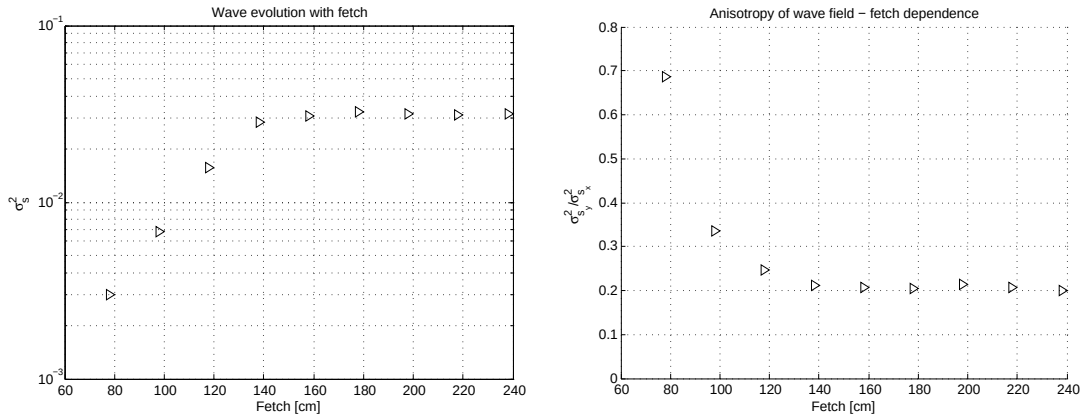


(a) (b)

Figure 6.11.: Fetch dependence of (a) the mean square slope $\sigma_s^2$ and (b) the directional slope ratio $\sigma_{s_y}^2/\sigma_{s_x}^2$. Both quantities remain constant for a fetch longer than 1.40 m.

$u_*^3$ for the strong increase and proportional to $u_*^1$ for the weak increase (Fig. 6.10(b)). This cannot be compared directly with the found relation for mean square slope, but the change in the relation is common for all measurements. Additionally, in the wave spectra of Klinke and Balschbach the change of the relation does only occur for the small wavelength of 8 mm. In the USSG measurements this change can be seen in the integral quantity mean square slope that includes all wavelengths. This is in agreement with the fact, that only small waves occur in the small linear wave flume.

### 6.2.4. Mean Square Slope Dependence on Fetch

For the variation of the fetch the cantilever with the USSG is moved to positions with a distance of 78 cm to 238 cm to the edge of the water basin where the wind first hits the water surface. The wind speed is set to a constant value of $u_{wind} = 5.0\,\mathrm{m/s}$. The water side friction velocity calculated from the air side friction velocity from Ueltzhöffer [45] is $u_{*\,w} = 1.17\,\mathrm{cm/s}$ for this wind speed. It is important to note that the wind speed was only measured at the end of the channel, i.e. at the longest fetch. Especially the friction velocity at shorter fetch can differ from these values as it depends on the roughness of the water surface.

Fig. 6.11(a) shows the development of the wave field with the fetch. The mean square slope increases up to a fetch of 1.40 m and is constant for longer fetch. The directional slope ratio is also constant for a fetch longer than 1.40 m (Fig. 6.11(b)). This is a clue that the wave field mainly consists of capillary waves that provide the main contribution

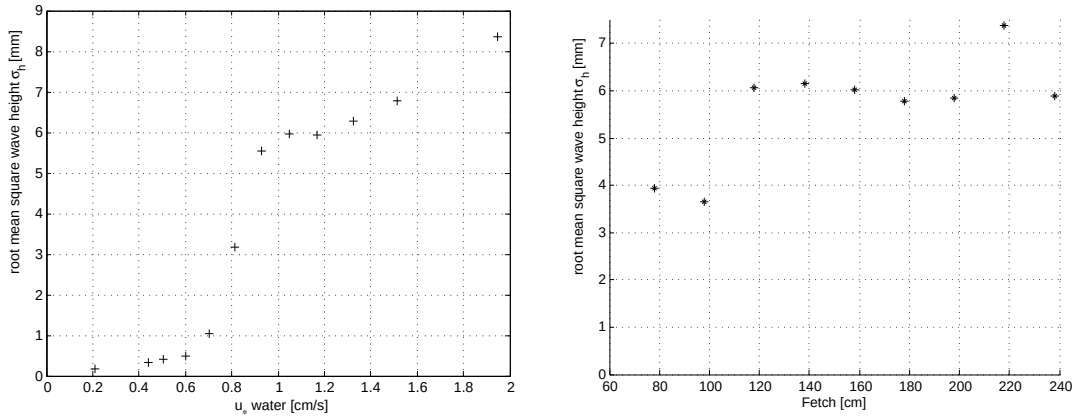


(a) (b)

Figure 6.12.: Root mean square wave height $\sigma_h$ as a function of (a) the friction velocity $u_*$ and (b) the fetch. The dependence of the rms wave height on the friction velocity and the fetch is similar to those of the mean square slope (cp. (a) with Fig. 6.10(a) and (b) with Fig. 6.11(a)).

to the surface slope and develop in the first 1.40 m of the fetch. After that distance energy might be transferred slowly to longer wave lengths, but the contribution of these to the slope remains small. This behavior is in agreement with the visual observation. An increasing roughness of the water surface within the first meter of fetch can be seen. Thereafter the appearance of the water surface remains constant.

Even for much longer fetches (4.90 m and 11.20 m) in the measurements by Lauer [28] no fetch dependence of the mean square slope (Fig. 6.8(b)) and the directional slope ratio (Fig. 6.9(b)) can be seen either.

## 6.3. Wave Height Distributions and Root Mean Square Wave Height

20000 light speckle images are taken for each wind speed to determine the water height, i.e. 10000 for each wavelength IR and RED. The root mean square wave height (rms wave height) is determined from a Gaussian probability density distribution of the measured water height (Fig. 5.9). For a rough water surface the additional effect of different light speckle size for IR and RED speckles leads to an artificial variation of the measured water height, which increases the rms wave height (see Sec. 4.2.4). Therefore, the rms wave height shown in Fig. 6.12 overestimates the real height values, i.e. the absolute values of the measured rms wave height are too high.

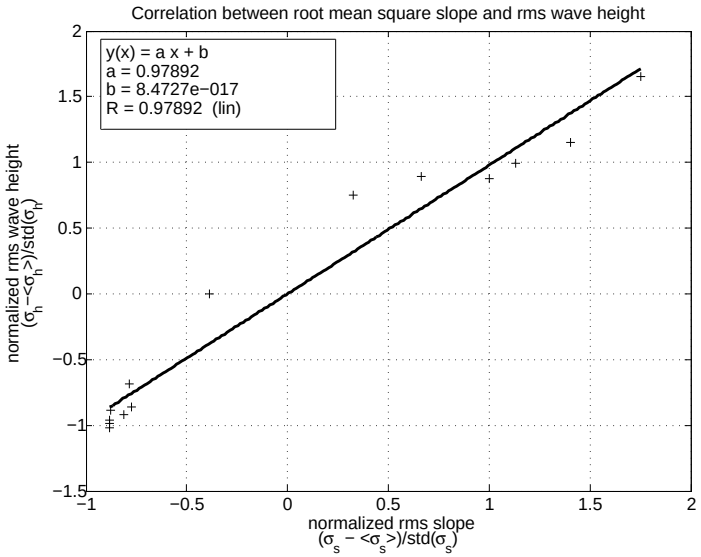


Figure 6.13.: Correlation between the normalized root mean square slope $\sigma_s$ and normalized rms wave height $\sigma_h$. In the measurement the friction velocity is varied and the fetch is constant at 2.38 m.

However, the dependence of the rms wave height on the friction velocity and on the fetch implies information about the wave field. Fig. 6.12(a) and Fig. 6.12(b) represent the same dependence of the rms wave height on friction velocity and fetch as already stated for the mean square slope in Fig. 6.10(a) and Fig. 6.11(a). Concerning the friction velocity, the rms wave height starts to increase abruptly at a friction velocity of $u_{*w} \approx 0.7\,\mathrm{cm/s}$ and changes to a weaker increase at $u_{*w} \approx 1\,\mathrm{cm/s}$. Concerning the fetch, the rms wave height is constant for a fetch longer than 1.20 m.

Fig. 6.13 shows the correlation between the root mean square slope and the rms wave height values which are taken simultaneously at a constant fetch of 2.38 m and a varied friction velocity (data in Fig. 6.10(a) and 6.11(a)). In order to obtain a geometrical parameter, the square root of the mean square slope is taken. Both quantities are nomalized. A positive correlation between the two parameters can be seen with a correlation coefficient of 0.98.

The correlation can partly be attributed to a bias of the height measurement that is due to lens effects, which occur in case of a rough water surface and which are therefore correlated with the mean square slope (see Sec. 4.2.4). However, for the longest fetch, the rms wave height of 6 mm is consistent with visual observations of the wave amplitudes. This suggests that - at least for higher values of the rms wave height - the height bias may only have a minor contribution. Therefore, it is expected that for the test conditions the rms wave height dependence on fetch and wind speed is indeed similar

to the mean square slope dependency.

It is important to note that the root mean square slope and the rms wave height of the wave field are only correlated for the special case of a very short fetch in the new linear wave flume. Here, small scale waves that just develop in the young wave field make the main contribution to both parameters. In general, for a longer fetch and an older wave field, the wave slope is dominated by small scale waves, whereas the wave height is dominated by large gravity waves.

# 7. Conclusion and Outlook

A new wave gauge for the measurement of slope and height statistics of water surface waves was built. It is ready to use for the characterization of the wave field in the new linear wind wave flume in the Institut für Umweltphysik (IUP), Heidelberg, in the context of gas transfer measurements, since the mean square wave slope is a key parameter for the gas exchange transfer velocity.

The wave gauge consists of a camera that looks perpendicular through the water surface into a dichromatic LED light source with two wavelengths 632 nm (RED) and 850 nm (IR). Only a light ray from the light source that is refracted at the water surface into the camera leads to a light speckle on the image. The refraction of the RED light at the water surface is used to measure the wave slope. The absorption of the IR (and RED) intensity is used to measure the water height, which is computed from the intensity ratio IR/RED. A set of 20000 images is taken to determine the probability density distributions of the wave slope and wave height at a single wave field condition.

In order to measure the absorption length from the IR/RED intensity ratio in the images two images must be taken of the same state of the fast moving water surface with different illumination from the light source. Therefore, the LED light source is pulsed and the camera is triggered to these pulses. A single pulse for one image is shorter than 60 $\mu$s. The IR LED pulse is set to the end of the first exposure time and the RED LED pulse is set to the beginning of the second exposure time, so that the temporal distance between the two pulses (RED and IR) is 80 $\mu$s. This short time which is limited by the used components turns out to be partly too long to image a stationary water surface, which leads to a bias of the height measurement.

The instrument was tested in the new linear wind wave flume in the IUP, Heidelberg. The flume has a mean water height of about 10 cm and the wind speed at 12 cm above the surface can be controlled from 0 to 6.7 m/s, which corresponds to a water side friction velocity up to 2 cm/s [45]. With a field of view of $71 \times 53\,\mathrm{mm}^2$ on the water surface the wave slope can be measured in the range of -1.5 to +1.5 in upwind direction and -1.0 to +1.0 in crosswind direction. In few cases single wave slopes outside the measurement range occurred, but the contribution of these to the slope probability distribution can be neglected.

A new analysis of different methods to determine the wave slope distribution from the series of light speckle images is made. It shows that a simple position detection of the light speckles is not sufficient, though the light speckle properties 'area' and 'intensity' have to be taken into account. The overall uncertainty of the total mean square slope values can be estimated to be less than 10 % from an intercomparison of the different analysis methods.

The height measurement is calibrated to an ultrasonic distance sensor and yields an error of less than 2 mm for a flat water surface. However, for a rough water surface, the measured water height is biased, so unrealistic height values appear. Lens effects due to the high curvature at the surface and fast changes of the wave slope can be an explanation for a different light speckle shape in corresponding IR and RED images and an additional variation of the light intensity in the images. This error cannot be corrected for, so the small wave amplitudes in the flume represent a relatively small signal compared to the noise due to the lens effects and fast slope changes. For a better understanding of the lens effects an exact ray tracing model at the water surface would be necessary. Changes of the slope between two images could be avoided with an even shorter time period between the two LED pulses. Limiting the fit range to realistic values, the root mean square wave height can still be estimated from the height probability distribution with a Gaussian fit.

A characterization of the wave field in the new linear wave flume is accomplished. Waves start to develop abruptly at a wind speed of 3.5 m/s or a water side friction velocity of 0.7 cm/s. A measurement at a wind speed of 5.0 m/s shows that the wave field develops within the first 1.40 m of the fetch and remains constant from there to the beach concerning the parameters mean square wave slope and rms wave height. At the maximum wind speed of $6.7 m/s$ and a fetch of 2.38 m the mean square slope is 0.059 and the rms wave height is 6 mm.

In addition to the usual use of the wave gauge at the linear wave flume, the wave gauge will be tested at the large circular flume, where the dominant wave height is higher by a factor of up to 100. Therefore the height measurement has a better signal to noise ratio and is expected to yield correct wave height values of the dominant gravity waves. The height values are needed in the large flume to correct the height dependent slope measurement. A correlation analysis of the height of the large scale waves and the slope can provide information about the long wave - short wave interaction.

A Reflective Slope Gauge (RSG) is planned to accompany heat transfer measurements in the field in 2009-2010. The detailed analysis of the single light speckle images shown in this study allows for a determination of the speckle properties. The findings can improve a quantitative evaluation of the RSG measurements.

# Bibliography


[1] G. Balschbach. *Untersuchungen statistischer und geometrischer Eigenschaften von Windwellen und ihrer Wechselwirkung.* PhD thesis, Universität Heidelberg, February 2000.

[2] S. Banerjee. *The Air-Water Interface: Turbulence and Scalar Exchange*, pages 87–101. Springer-Verlag, 2007.

[3] M. Bass. *Handbook of Optics, Volume 1, Fundamentals, Techniques, and Design.* McGraw Hill, New York, 1995.

[4] E. J. Bock and T. Hara. Optical measurements of capillary-gravity wave spectra using a scanning laser slope gauge. *Journal of Atmospheric and Oceanic Technology*, 12(2):395–403, April 1995.

[5] E. J. Bock, T. Hara, N. M. Frew, and W. R. McGillis. Relationship between air-sea gas transfer and short wind waves. *Journal of Geophysical Research-Oceans*, 104 (C11):25821–25831, 1999. J NOV 15.

[6] J.-I. Bouguet. Camera calibration toolbox for matlab. *on http://www.vision.caltech.edu/bouguetj/; 25.07.2008*, 2008.

[7] G. Caulliez, V. K. Makin, and V. N. Kudryavtsev. Drag on the water surface at very short fetches: observations and modelling. *Journal of Physical Oceanography*, preprint, 2008.

[8] C. Cox and W. Munk. Measurements of the roughness of the sea surface from photographs of the sun's glitter. *Journal of the Optical Society of America*, 44(11): 838–850, 1954.

[9] C. Cox and W. Munk. Statistics of the sea surface derived from sun glitter. *Journal of Marine Research*, 13(2):198–227, 1954.

[10] G. D. Crapper. Non-linear capillary waves generated by steep gravity waves. *Journal of Fluid Mechanics*, 40(I):149–159, 1970.

[11] S. R. Duke, L. M. Wolff, and T. J. Hanratty. Slopes of small-scale wind waves and their relation to mass transfer rates. *Experiments in Fluids*, 19:280–292, 1995.

[12] N. Ebuchi, H. Kawamura, and Y. Toba. Fine structure of laboratory wind-wave surfaces studied using a optical method. *Boundary-Layer Meteorology*, 39:133–151, 1987.

[13] N. M. Frew, E. J. Bock, and U. e. a. Schimpf. Air-sea gas transfer: Its dependence on wind stress, small-scale roughness, and surface films. *Journal of Geophysical Research*, 109(C8):C08S17, 2004.

[14] N. M. Frew, D. Glover, E. Bock, and S. McCue. A new approach to estimation of global air-sea gas transfer velocity fields using dual-frequency altimeter backscatter. *J. Geophys. Res.*, 112:C11003, 2007.

[15] D. Fuß. *Kombinierte Höhen- und Neigungsmessung von winderzeugten Wasserwellen am Heidelberger Aeolotron.* PhD thesis, University of Heidelberg, Heidelberg, Germany, 2004.

[16] G. M. Hale and M. R. Querry. Optical constants of water in the 200 nm to 200 $\mu$m wavelength region. *Appl.Opt.*, 12:555–563, 1973.

[17] B. Jähne. *Parametrisierung des Gasaustauschs mit Hilfe von Laborexperimenten.* Phd thesis, Universität Heidelberg, 1980.

[18] B. Jähne. *Digitale Bildverarbeitung.* Springer Verlag, fünfte edition, 2002.

[19] B. Jähne, J. Klinke, and S. Waas. Imaging of short ocean wind waves: a critical theoretical review. *J.Opt.Soc.Am.*, 11(8):2197–2209, 1994.

[20] B. Jähne, K. O. Münnich, R. Bösinger, A. Dutzi, W. Huber, and P. Libner. On the parameters influencing air–water gas exchange. *Journal of Geophysical Research*, 92(C2):1937–1949, February 1987.

[21] B. Jähne, K. O. Münnich, and U. Siegenthaler. Measurements of gas exchange and momentum transfer in a circular wind-water tunnel. *Tellus*, 31:321–329, 1979.

[22] B. Jähne and K. Riemer. Two-dimensional wave number spectra of small-scale water surface waves. *J.Geophys.Res.*, 95(C7):11531–11646, 1990.

[23] B. Jähne, M. Schmidt, and R. Rocholz. Combined optical slope/height measurements of short wind waves: principles and calibration. *Measurement Science & Technology*, 16(10):1937–1944, 2005.

[24] I. S. F. Jones and Y. Toba. *Wind Stress over the Ocean.* Cambridge University Press, Cambridge,UK, 2001.

[25] J. Klinke. *Optical Measurements of Small-Scale Wind Generated Water Surface Waves in the Laboratory and the Field.* PhD thesis, University of Heidelberg, Heideleberg, Germany, 1996.

[26] G. Komen, editor. *Dynamics and modelling of ocean waves.* Cambridge University Press, 1994.

[27] P. K. Kundu. *Fluid Mechanics.* Academic Press, San Diego, CA, 1990.

[28] H. Lauer. Messung der Neigungsverteilung von Wasseroberflaechenwellen mittels digitaler Bildverarbeitung. Master's thesis, Universität Heidelberg, 1994.

[29] H. Lauer. *Untersuchung der Neigungsstatistik von Wasseroberflächenwellen mittels eines schnellen, bildaufnehmenden Verfahrens.* Dissertation, Universität Heidelberg, 05 1998.

[30] P. S. Liss and L. Merlivat. Air-sea gas exchange rates: Introduction and synthesis. In P. Buat-Menard, editor, *The role of air-sea exchange in geochemical cycling*, pages 113–129. Reidel, Boston,MA, 1986.

[31] M. S. Longuet-Higgins. The statistical analysis of a random, moving surface. *Journal of Marine Research*, 249:321–387, February 1957. A. 966.

[32] K. V. N. Makin, V. K. Coupled sea surface-atmosphere model. part 1. wind over waves coupling. *Journal of Geophysical Research*, 104:7613–7623, 1999.

[33] W. R. McGillis, J. B. Edson, J. E. Hare, and C. W. Fairall. Direct covariance air-sea $CO_2$ fluxes. *Journal of Geophysical Research*, 106(C8):16729–16745, 2001.

[34] H. Mitsuyasu. A note on the momentum transfer from wind to waves. *Journal of Geophysical Research*, 90:3343–3346, 1985.

[35] P. D. Nightingale, P. S. Liss, and P. Schlosser. Measurements of air-sea gas transfer during an open ocean algal bloom. *Geophysical Research Letters*, 27:2117–2120, July 2000.

[36] O. M. Phillips. *The dynamics of the upper ocean.* Cambridge University Press, 1969.

[37] R. A. Pierson, W. J. (Jr) Stacy. The elevation, slope, and curvature spectra of a wind roughened sea surface, 1973.

[38] W. J. Plant. A new interpretation of sea-surface slope probability density functions. *Journal of Geophysical Research*, 108(C9):3295, 2003.

[39] R. Rocholz. Bildgebendes system zur simultanen neigungs- und höhenmessung an kleinskaligen wind-wasserwellen. Diploma thesis, University of Heidelberg, 2005.

[40] R. Rocholz. *Spatiotemporal Measurement of Short Wind-Driven Water Waves*. PhD thesis, University of Heidelberg, 2008. in preperation.

[41] W. Roedel. *Physik unserer Umwelt: die Atmosphäre*. Springer-Verlag, 3 edition, 2000.

[42] D. Segelstein. The complex refractive index of water. *M.S. Thesis, University of Missouri-Kansas City*, 1981.

[43] W. Tsai and L. Hung. *A Numerical Study on the Characteristic Flow Structures of a Micro-Breaking Wind Wave*. Springer-Verlag, 2007.

[44] W. Tsai and L. Hung. Three-dimensional modeling of small-scale processes in the upper boundary layer bounded by a dynamic ocean surface. *Journal of Geophysical Research*, 112:C02019, 2007.

[45] K. Ueltzhöffer. Windprofilmesungen am linearen Wind-Wellenkanal. Technical report, Institut für Umweltphysik, Heidelberg, 2008.

[46] S. Waas. Entwicklung eines Verfahrens zur Messung kombinierter Höhen- u. Neigungsverteilungen von Wasseroberflächenwellen mit Stereoaufnahmen. Master's thesis, University of Heidelberg, 1988.

[47] WAMDI. The wam model - a third generation ocean wave prediction model. *Journal of Physical Oceanography*, 18:1775–1810, 1988.

[48] R. Wanninkhof. Relationship between gas exchange and wind speed over the ocean. *Journal of Geophysical Research*, 97(C5):7373–7382, 1992.

[49] C. Zappa, M. L. Banner, H. Schultz, A. Corrada-Emanuel, L. B. Wolff, and J. Yalcin. Retrieval of short ocean wave slope using polarimetric imaging. *Meas. Sci. Technol.*, 19, 2008.

[50] X. Zhang. Capillary-gravity and capillary waves generated in a wind wave tank: Observations and theories. *Journal of Fluid Mechanics*, 189:51–82, 1995.

**Erklärung:**

Ich versichere, dass ich diese Arbeit selbständig verfasst und keine anderen als die angegebenen Quellen und Hilfsmittel benutzt habe.

Heidelberg, 03.09.2008

**Danksagung**

Besonders bedanken möchte ich mich bei Prof. Dr. Bernd Jähne, der diese Arbeit betreut und sie erst möglich gemacht hat. Ein großer Dank geht auch an Prof. Dr. Platt für die Übernahme der Zweitkorrektur.

Außerdem möchte ich noch meinen Dank aussprechen

Roland Rocholz, der mir seine Zeit geopfert hat für ausführliche Diskussionen und wertvolle Tipps,

der ganzen Arbeitsgruppe "Gasaustausch und Wellen" am Institut für Umweltphysik in Heidelberg für ihre tolle Unterstützung meiner Arbeit, der Beantwortung der vielen Fragen und die allzeit nette Stimmung im Windkanal Labor,

der Institutswerkstatt im IUP und Herrn Spiegel in der Diplomandenwerkstatt für die freundliche Beratung in technischen Fragen,

und nicht zuletzt meiner Freundin und meinen Eltern dafür, dass sie immer da sind.

# Appendices

# A. Calculations

## A.1. Water height amplitude from IR and RED speckle intensities

The slant absorption length $l$ in water is

$$l = -\frac{1}{(\alpha_{IR} - \alpha_{RED})} ln\left(\frac{I_{IR}}{I_{RED}}\right) + C \tag{A.1}$$

$$l = b + C \tag{A.2}$$

with measured IR intensity $I_{IR}$ and RED intensity $I_{RED}$ of the same speckle. $C$ is a constant length.

The correction from the slant absorption length $l$ to the vertical water height $\eta$ is

$$\eta = l \cos\theta_2 \tag{A.3}$$

with $\theta_2$ as defined in Fig. 3.1.

$l$ and $\cos\theta_2$ are not totally uncorrelated, but the error is small, $\frac{\langle l \cos\theta_2\rangle - \langle l\rangle\langle\cos\theta_2\rangle}{\langle\eta\rangle} = 0.1\%$, so

$$d_2 = \langle\eta\rangle = \langle l \cos\theta_2\rangle \approx \langle l\rangle\langle\cos\theta_2\rangle \tag{A.4}$$

$$\langle l\rangle \approx \frac{\langle\eta\rangle}{\langle\cos\theta_2\rangle} = \frac{d_2}{\langle\cos\theta_2\rangle} \tag{A.5}$$

with the mean water height $\langle\eta\rangle = d_2$.

Hence,

$$l - \langle l\rangle = b - \langle b\rangle + C - \langle C\rangle \tag{A.6}$$

$$l = b - \langle b\rangle + \langle l\rangle \tag{A.7}$$

$$l = b - \langle b\rangle + \frac{d_2}{\langle\cos\theta_2\rangle} \tag{A.8}$$

So with Eq. A.3 and Eq. A.8 the water surface amplitude $h$ becomes

$$h = \eta - \langle\eta\rangle \tag{A.9}$$

$$= l\cos\theta_2 - d_2 \tag{A.10}$$

$$= \left[b - \langle b\rangle + \frac{d_2}{\langle\cos\theta_2\rangle}\right]\cos\theta_2 - d_2 \tag{A.11}$$

# B. Measurement Data

## B.1. Light speckle area dependence on slope

The mean area of the light speckles decreases to higher slopes (Fig. B.1). This is probably due to a higher curvature of the water surface that occurs for small steep capillary waves.

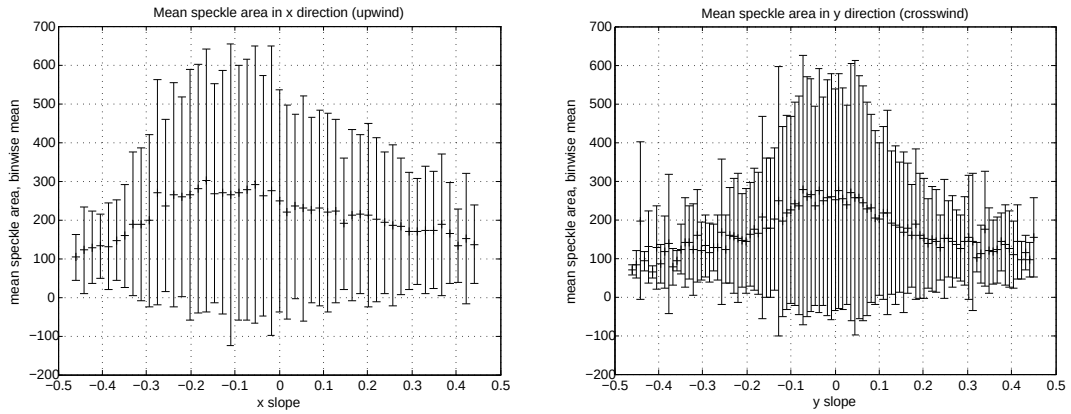


(a) (b)

Figure B.1.: The mean light speckle area decreases to higher slopes.

## B.2. Evolution of the Slope Distribution with Wind Speed

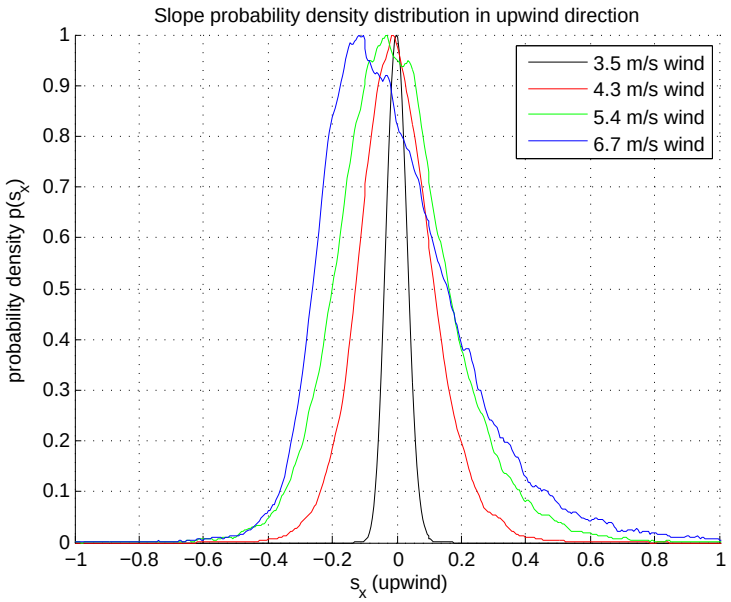


(a) Slope probability density distributions in upwind direction

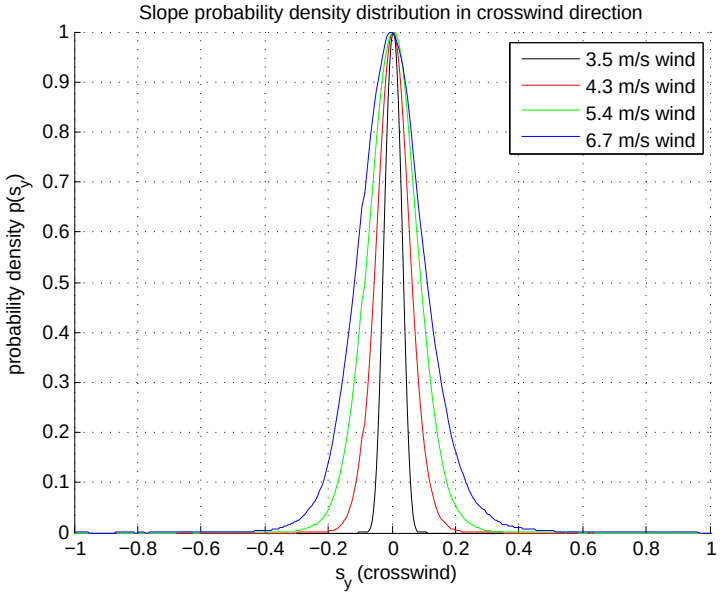


(b) Slope probability density distributions in crosswind direction

Figure B.2.: Evolution of 1-dim directional slope distributions with wind speed. The skewness of the upwind distribution increases with increasing wind speed (a), whereas the crosswind distribution remains symmetric (b).

## B.3. Verification of the Pinhole Camera Model

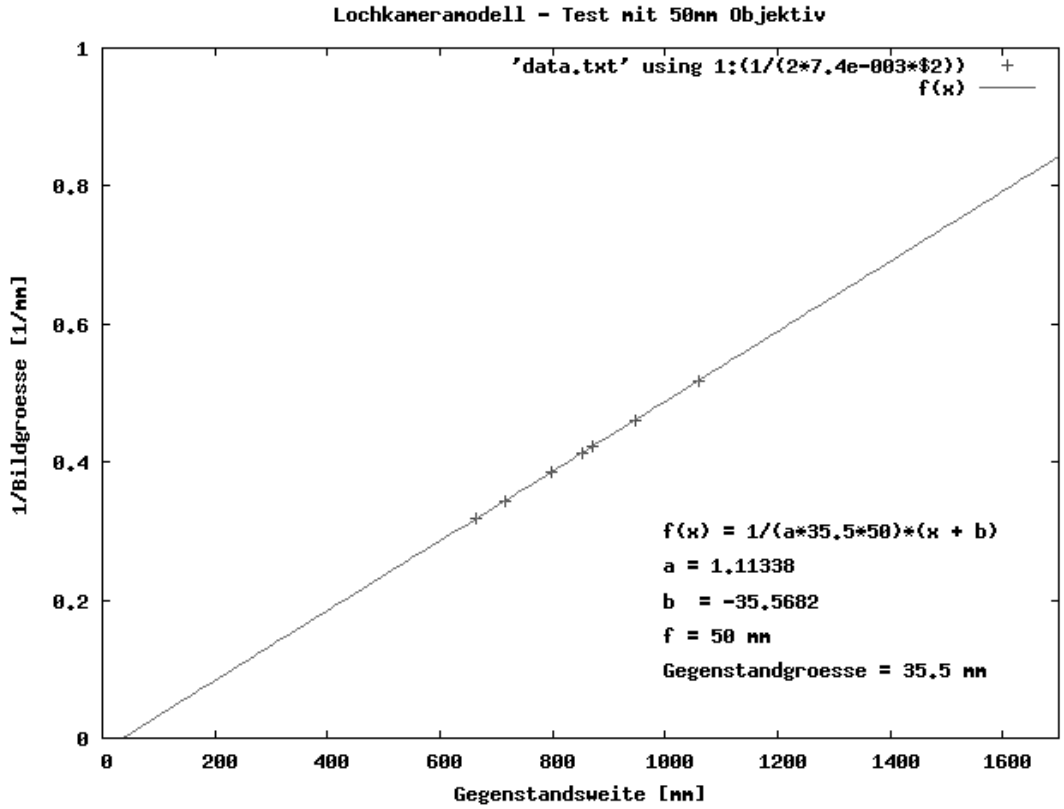


Figure B.3.: Inverse image size $\frac{1}{b}$ as a function of the distance object-pinhole $G$. The pinhole camera model applies. Verification of theorem of intersecting lines: $\frac{G}{g} = \frac{f}{b}$; with G: distance object-pinhole, g: object size, f: focal length, b: image size. The fit parameter $b = -35.5682\,\mathrm{mm}$ is the position of the fictive pinhole (the aperture) in the objective lens measured from the front edge.

## B.4. Mean Square Slope, Friction Velocity and Wind Data

The data columns in Fig. B.4 are:

1. $u_{wind}[m/s]$: wind speed measured with the Prandtl tube at 12 cm above the water surface and 2.70 m fetch
2. $u_{*\ a}[m/s]$: interpolated air side friction velocity from Ueltzhöffer [45] measured at a fetch of 2.70 m. The first two values could not be interpolated.
3. $u_{*\ w}[m/s]$: calculated water side friction velocity
4. $\langle s_x^2 \rangle$: mean square slope in x-direction (upwind)
5. $\langle s_y^2 \rangle$: mean square slope in y-direction (crosswind)
6. $\langle s^2 \rangle$: total mean square slope
7. $\langle s_y^2 \rangle \,/\, \langle s_x^2 \rangle$: directional mean square slope ratio

All slopes are measured at a fetch of 2.40 m. Errors are given in Chap. 6.

| u_wind[m/s] | u*air[m/s] | u*water[m/s] | sx^2 | sy^2 | s^2 | sx^2/sy^2 |
|---|---|---|---|---|---|---|
| 0.0300 | NaN | NaN | 0.0004 | 0.0004 | 0.0008 | 1.0351 |
| 0.5700 | NaN | NaN | 0.0004 | 0.0004 | 0.0008 | 1.0351 |
| 1.2600 | 0.0600 | 0.0021 | 0.0004 | 0.0004 | 0.0008 | 1.0323 |
| 2.3600 | 0.1261 | 0.0044 | 0.0006 | 0.0005 | 0.0012 | 0.8328 |
| 2.7300 | 0.1453 | 0.0050 | 0.0004 | 0.0004 | 0.0008 | 1.0366 |
| 3.1100 | 0.1726 | 0.0060 | 0.0007 | 0.0006 | 0.0014 | 0.8825 |
| 3.4900 | 0.2022 | 0.0070 | 0.0008 | 0.0005 | 0.0013 | 0.6135 |
| 3.8700 | 0.2345 | 0.0081 | 0.0037 | 0.0010 | 0.0047 | 0.2735 |
| 4.2500 | 0.2678 | 0.0093 | 0.0134 | 0.0026 | 0.0161 | 0.1967 |
| 4.6400 | 0.3019 | 0.0105 | 0.0199 | 0.0038 | 0.0237 | 0.1892 |
| 5.0300 | 0.3360 | 0.0117 | 0.0280 | 0.0050 | 0.0330 | 0.1791 |
| 5.4300 | 0.3818 | 0.0133 | 0.0309 | 0.0060 | 0.0369 | 0.1958 |
| 5.8400 | 0.4361 | 0.0151 | 0.0382 | 0.0077 | 0.0459 | 0.2010 |
| 6.6500 | 0.5614 | 0.0195 | 0.0471 | 0.0117 | 0.0588 | 0.2483 |

Figure B.4.: Measurement data from the wave gauge in the linear wind wave flume

Friction velocity from Ueltzhöffer [45]. The data columns in Fig. B.5 are:

1. $u_{wind}[m/s]$: wind speed measured with the Prandtl tube at 12 cm above the water surface and 2.70 m fetch
2. $u_{*\ a}[m/s]$: air side friction velocity from a logarithmic fit to the wind profiles
3. $\Delta u_{*\ a}[m/s]$: error of friction velocity from fit

| u_wind[m/s] | u*air[m/s] | u*air_err[m/s] |
|---|---|---|
| 0.58 | 0.06 | 0.02 |
| 1.31 | 0.06 | 0.01 |
| 2.05 | 0.11 | 0.01 |
| 2.82 | 0.15 | 0.01 |
| 3.59 | 0.21 | 0.01 |
| 4.39 | 0.28 | 0.02 |
| 5.19 | 0.35 | 0.02 |
| 6.02 | 0.46 | 0.01 |
| 6.89 | 0.60 | 0.02 |

Figure B.5.: Friction velocitiy from Ueltzhöffer [45]

# C. Images

## C.1. Images of the Wave Gauge Setup

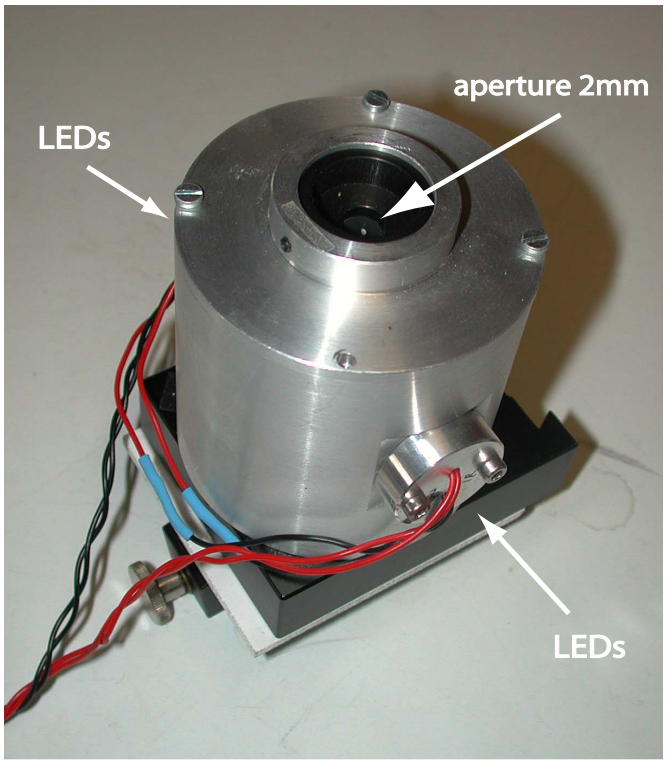


Figure C.1.: Ulbricht sphere encapsulated in an aluminium frame. The aperture is fixed with a grub screw and can easily be changed. The LEDs are series connected for each color, IR and RED.

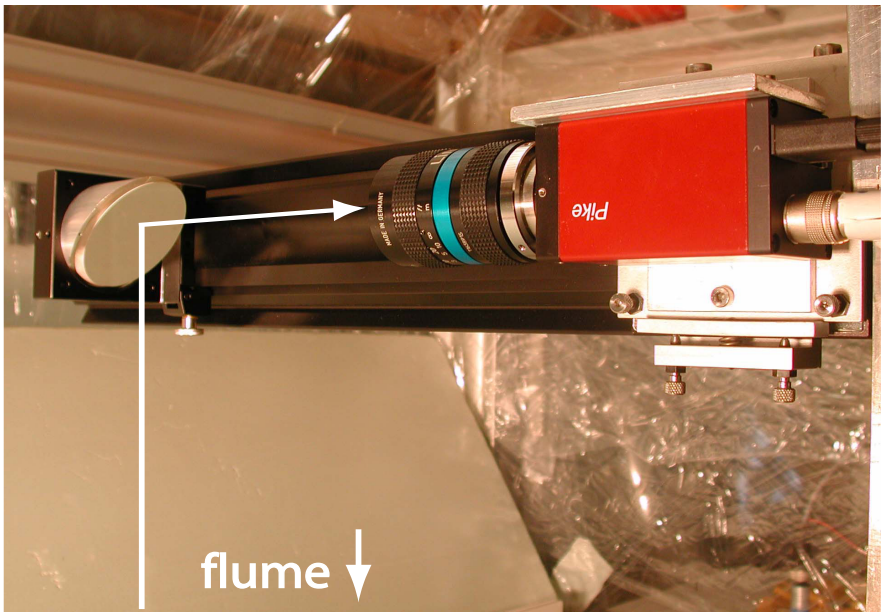


Figure C.2.: The camera is fixed on a mobile cantilever that can be moved along the flume. The direction of the camera is adjusted with fine thread screws. The mirror has an angle of 45°, so the camera looks perpendicular to the water surface

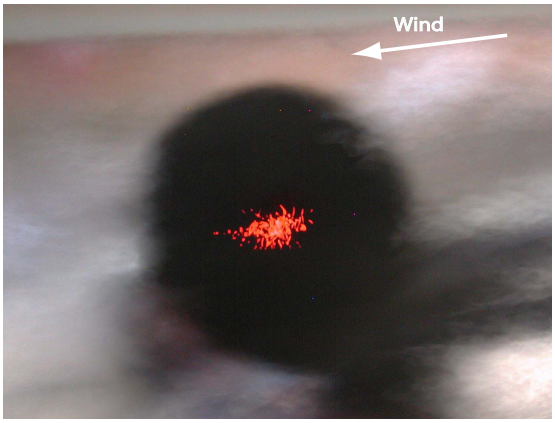


Figure C.3.: View on the light source through the water surface with a normal photo camera with exposure time 1 s. This time corresponds to 100 RED LED flashs. A cloud of red light speckles refracted at different slopes can be seen. The anisotropy of the slope distribution is already visible. The black disk is a plastic disk fixed on the light source to reduce background intensity.

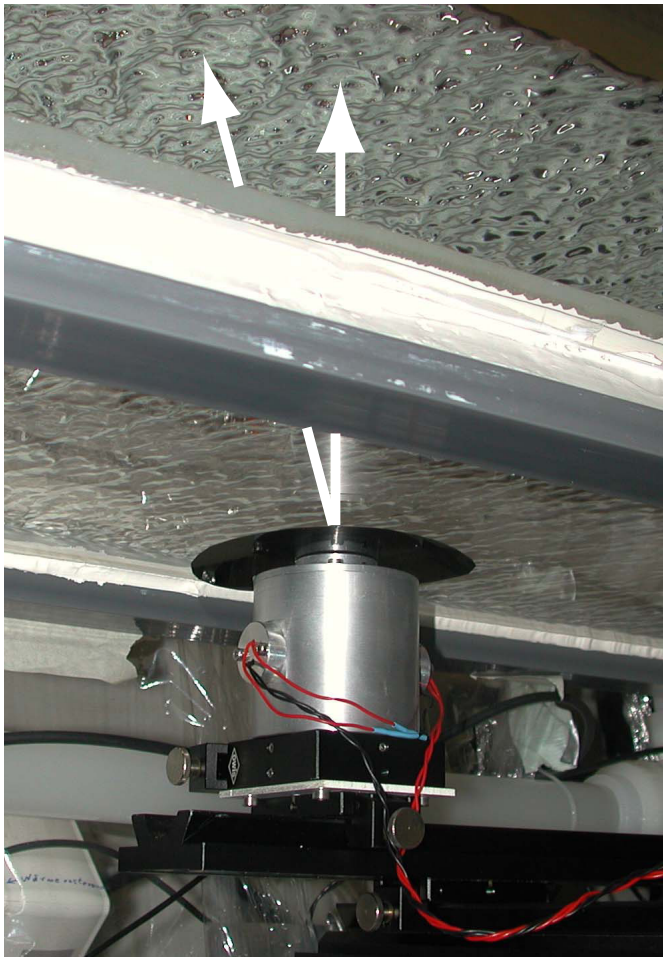

Figure C.4.: Ulbricht sphere under the wind wave flume. It is fixed on the same cantilever as the camera and can be moved along the flume without changing the position to the camera